Master's thesis

NTNU
Norwegian University of Science and Technology
Faculty of Natural Sciences
Department of Materials Science and Engineering

Ragnhild Austreid

Diffusion studies of Fe in amorphous quartz for the PV industry

Master's thesis in Chemical Engineering and Biotechnology
Supervisor: Marisa Di Sabatino Lundberg
Co-supervisor: Eivind Øvrelid
July 2020

NTNU
Norwegian University of
Science and Technology

Ragnhild Austreid

Diffusion studies of Fe in amorphous quartz for the PV industry

Master's thesis in Chemical Engineering and Biotechnology
Supervisor: Marisa Di Sabatino Lundberg
Co-supervisor: Eivind Øvrelid
July 2020

Norwegian University of Science and Technology
Faculty of Natural Sciences
Department of Materials Science and Engineering

NTNU
Norwegian University of
Science and Technology

Preface

This Master's thesis was carried out at the Norwegian University of Science and Technology (NTNU) at the Department of Materials Science and Engineering. The thesis was part of the course TMT4900 Materials Chemistry and Energy Technology and was done in collaboration with SINTEF's CruGenSi project. The work took place during spring 2020 and was completed at Gløshaugen Campus. An additional challenge this semester was the unforeseen outbreak of Covid-19. As a result, some experiments were not completed as planned due to restricted laboratory access.

I am very thankful for all of the knowledgeable people who have guided me throughout the master. I would like to show my sincere gratitude to my supervisor Prof. Marisa Di Sabatino Lundberg and my co-supervisor Senior Research Scientist Eivind Øvrelid (SINTEF) for the guidance and valuable advice throughout the year. I would also like to give a special thank you to PhD Candidate Jochen Busam and Prof. Marisa Di Sabatino Lundberg for the great help with performing the GD-MS analyses.

Finally, I would also like to thank my fellow students for all of the support, motivation and laughter throughout the study.

Ragnhild Austreid
Trondheim, July 2020

Abstract

Crucible materials have been identified as a dominant contamination source during the solidification process of multicrystalline silicon (mc-Si) ingots for solar cells. Too high concentrations of metallic impurities, such as iron, in the silicon are detrimental to the solar cell performance. However, there are few studies and publications on the diffusion mechanisms and behaviour of iron in quartz crucibles. To address this, this study aims to measure the diffusion coefficient of iron in amorphous quartz (SiO_2) crucibles to gain a better understanding of the iron in-diffusion and contamination in mc-Si. A quantitative analysis of iron diffusion in quartz crucibles is presented. Heat treatment of diffusion couples consisting of slip-cast crucible and steel, with synthetic quartz glass as a reference, is performed in a GSL-1500X-50RTP tube furnace. The diffusion coefficient of iron is measured in the temperature range 900-1300 °C, in a vacuum atmosphere. Concentration vs depth profiles are measured using glow discharge mass spectrometry (GD-MS). The results of the work can be used further as input parameters to predict by modelling the iron distribution in the mc-Si ingots. Further, this thesis also includes a literature review on diffusion studies in quartz. A general overview of the diffusion behaviour of different elements measured in quartz is summarised and compared.

Over the temperature range 900-1300 °C, the following Arrhenius relations were obtained for the diffusion of iron in a standard grade silica crucible and synthetic quartz glass, respectively,

$$D = 6.53 \cdot 10^{-8} exp\left(\frac{-1.154 \text{ eV}}{kT}\right) \text{ cm}^2\text{/s}$$

$$D = 1.05 \cdot 10^{-9} exp\left(\frac{-0.937 \text{ eV}}{kT}\right) \text{ cm}^2\text{/s}$$

The diffusion of iron in the slip-cast silica crucible was found to be one order of magnitude higher than in the synthetic quartz glass, with measured diffusion coefficients in the range of 10^{-13}-10^{-11} cm^2/s in the silica crucible compared to 10^{-14}-10^{-12} cm^2/s in the quartz glass. GD-MS proved to be a sufficient method for obtaining the concentration vs depth profiles with calculated sputtering rates of 0.57 nm/s and 0.30 nm/s for the silica crucible and quartz glass, respectively.

Sammendrag

Kvartsdiglene som brukes til å støpe multikrystallinsk silisium (mc-Si) til solcelleindustrien er en dominerende forurensningskilde i silisiumproduksjonen. For høye konsentrasjoner av metalliske urenheter, som jern, i silisium er svært ødeleggende for strømutbyttet til solcellen. Derimot er det få studier og publikasjoner som undersøker diffusjonsmekanismene til jern i diglene og hvordan jernet forurenser silisiumet. Formålet med denne oppgaven er derfor å måle diffusjonskoeffisienten til jern i amorfe kvartsdigler (SiO_2) for å bidra til forståelsen av hvordan jernet diffunderer inn og forurenser mc-Si ingoten. En kvantitativ analyse av jerndiffusjon i kvartsdigler er presentert. Varmebehandling av diffusjonspar bestående av en standard kvartsdigel og stål, med syntetisk kvartsglass som referanse, utføres i en GSL-1500X-50RTP rørovn. Diffusjonskoeffisienten måles i vakuum for temperaturområdet 900-1300 °C og konsentrasjonsprofilene av jern måles ved bruk av glødeavladnings massespektrometer (GD-MS). Resultatene fra arbeidet kan videre brukes til å modellere fordelingen av jern i silisiumingoten. I tillegg inkluderer denne avhandlingen en litteraturdel om diffusjonsstudier i kvarts. En generell oversikt over diffusiviteten til ulike elementer målt i kvarts er oppsummert og sammenlignet.

I temperaturområdet 900-1300 °C ble følgende Arrhenius forhold målt for diffusjonen av jern i henholdsvis kvartsdigelen og kvartsglasset,

$$D = 6.53 \cdot 10^{-8} exp\left(\frac{-1.154\,\text{eV}}{kT}\right)\ \text{cm}^2/\text{s}$$
$$D = 1.05 \cdot 10^{-9} exp\left(\frac{-0.937\,\text{eV}}{kT}\right)\ \text{cm}^2/\text{s}$$

Diffusiviteten av jern i kvartsdigelen ble funnet til å være en størrelsesorden høyere enn diffusiviteten av jern i syntetisk kvartsglass, med målte diffusjonskoeffisienter i området 10^{-13}-10^{-11} cm^2/s i kvartsdigelen sammenlignet med 10^{-14}-10^{-12} cm^2/s i kvartsglasset. GD-MS viste seg å være en god metode for å oppnå konsentrasjonsprofilene av jern i de to kvartsmaterialene med beregnede sputteringshastigheter på henholdsvis 0.57 nm/s og 0.30 nm/s for digelen og kvartsglasset.

Table of Contents

List of Tables

List of Figures

Abbreviations

GD-MS	=	glow discharge mass spectrometry
mc-Si	=	multicrystalline silicon
PV	=	photovoltaic
RSF	=	relative sensitivity factor
SEM	=	scanning electron microscopy
VGF	=	vertical gradient freeze
XRD	=	x-ray diffraction

Chapter 1

Introduction

Mono- and multicrystalline silicon are by far the most common semiconductor materials, dominating the photovoltaic market with 95 %.[1] Compared to monocrystalline silicon, multicrystalline silicon (mc-Si) contains a higher amount of defects and impurities that are introduced during the directional solidification process. Contamination from the silicon feedstock, furnace atmosphere, crucible and coating is incorporated into the silicon ingot.[2] As a result, the solar cell efficiency using monocrystalline silicon is higher than for mc-Si with current lab record efficiencies of 26.7 % and 22.3 %, respectively.[3] The crystallisation process and feedstock quality of mc-Si have been improved in recent years, but the electrical material quality is still limited by crystal defects and metal impurities.[4] Maintaining the high purity of the raw silicon material is one of the main challenges and is essential to obtain a high-quality silicon material and wafer yield.[5] Too high concentrations of metallic impurities in the silicon are detrimental to the solar cell performance. Consequently, it is vital to prevent the contamination incorporated during the directional solidification process.[6][7]

The amorphous quartz (SiO_2) crucible and silicon nitride (Si_3N_4) coating used in the production of mc-Si ingots have been identified as dominant contamination sources. Further, iron is considered one of the most harmful and common metal impurities in mc-Si. It is introduced from the silicon feedstock and the crucible and coating materials during the solidification process. Deeper level impurities, such as iron, are very detrimental as they introduce trapping sites in the silicon bandgap, promoting the recombination of charge carriers. This trapping effect creates recombination centres which reduce the minority carrier lifetime, further resulting in a reduced solar cell efficiency.[8][9][10] The electrical performance of p-type silicon solar cells can be severely degraded by iron contamination. Concentrations of greater than 10^9 cm^{-3} will cause a significant reduction in the bulk lifetime.[11]

1.1 Objectives

In the past years, it has become increasingly important to understand the mechanisms of iron contamination and its harmful effects in silicon devices, due to the high expenses of the purifying technology.[8] The industrial solar cell concepts are developing to higher efficiency potentials which increases the demand for high-quality mc-Si. The metal contamination is still a crucial factor, limiting the carrier lifetime and degrading the electrical performance.[12] This substantiates the importance of investigating the origins and transport mechanisms of the metal impurities. Although the impurity modelling of iron in solid silicon has been studied, less research has been done on the mechanisms of iron diffusion in the crucible and coating materials, even though they are identified as dominant contamination sources.[10][13][14] Furthermore, there are no confirmed data in the literature on the diffusion coefficient for iron in the silica crucibles used for directional solidification of mc-Si. To address this, this thesis aims to measure the diffusion coefficient of iron in amorphous quartz (SiO_2) crucibles to gain a better understanding of the iron in-diffusion and contamination in silicon. A method for performing heat treatments of diffusion couples consisting of slip-cast crucible and steel, with quartz glass as a reference, has been developed. The diffusion coefficient of iron is measured in the temperature range 900-1300 °C, in a vacuum atmosphere. Glow discharge mass spectrometry (GD-MS) is used to obtain the concentration vs depth profiles. The results of the work can be further used as input parameters to predict by modelling the iron distribution in the mc-Si ingots.

Chapter 2

Theory

The following section presents the essential theory and background for this thesis that is necessary for the interpretation of the results.

2.1 Crystalline silicon solar cells

The photovoltaic (PV) market is dominated by silicon solar cells. Mono- and multicrystalline silicon are by far the most common semiconductor materials and in 2018 they accounted for about 95 % of the market.[1] There are several techniques for producing silicon wafers for the PV industry. The most common methods are the directional solidification of multicrystalline silicon and the growth of monocrystalline silicon through the Czochralski process. Currently, industrial silicon ingots are produced larger than 700 kg. The ingots are sliced into wafers of typically 15x15 cm^2 before they are used in the fabrication of solar cells.[15]

2.1.1 Directional solidification

Multicrystalline silicon (mc-Si) is produced from directional solidification. The process involves controlled cooling of molten silicon in a crucible. The silicon solidifies, commencing from the bottom of the crucible and going up. Upon the solidification, random nucleation starts in many places simultaneously, leading to larger crystals growing in a columnar way with arbitrary shapes and crystallographic orientations. The grain sizes vary from microns to several centimetres.[12] There are various methods of the directional solidification process; vertical gradient freeze (VGF), Bridgman and Stockbarger methods. The different principles are based on the controlled shifting of the temperature profile relative to the crucible. There are three ways of doing this; 1) the VGF method involves shifting the temperature by changing the furnace power, no mechanical movement of the crucible is involved 2) the Bridgman and Stockbarger methods are achieved by either me-

chanical movement of the crucible relative to the fixed furnace or 3) by shifting the temperature profile by moving the furnace relative to the fixed crucible.[16][17] The Bridgman technique is illustrated in Figure 2.1. The crucible is pulled down, out of the furnace, commencing the cooling and nucleation from the bottom.[18]

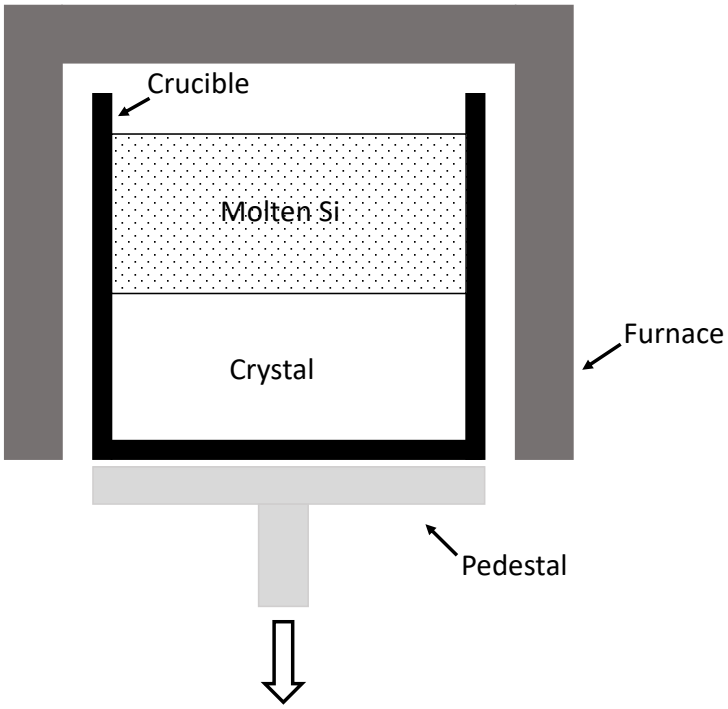

Figure 2.1: An illustration of the directional solidification method using the Bridgman technique. The crucible is pulled down, out of the furnace, commencing the cooling from the bottom.[18]

Table 2.1: Typical impurity levels in mc-Si given in ppma.[18][15]

Element	**Typical value [ppma]**
Fe	< 0.1
Al	0.5-2
Cu, Mn, Cr, Mg, Sr	< 0.1

Monocrystalline silicon is produced from the Czochralski method. A crystal seed is introduced to the molten silicon and slowly pulled out in a rotating motion to grow the single-crystal in a

cylindrical shape. Compared to the directional solidification method, the crystal growing is not in direct contact with the crucible and coating, reducing the amount of contamination in the silicon ingot. The quality of mc-Si is, therefore, lower due to defects and more impurities introduced from the feedstock, crucible and coating.[2] Typical impurity levels in mc-Si are given in Table 2.1.[18] During the growth of mc-Si ingots, defects such as dislocations, randomly oriented grain boundaries, oxides and inclusions can be generated. Therefore, mc-Si is an inhomogeneous material with dislocations densities ranging from 10^2 cm^{-2} to 10^7 cm^{-2} in dislocation clusters. These defects will trap mobile impurities through segregation due to higher solubility in the strain field, or through precipitation of supersaturated impurities.[12] Schön et al. found iron concentrations of three orders of magnitude higher in the vicinity of defects compared to in undisturbed areas.[12] Defects will usually work as recombination centres and are harmful to the performance of the solar cell.[5] As a result, the solar cell efficiency using monocrystalline silicon is higher than for mc-Si, with current lab record efficiencies of 26.7 % and 22.3 %, respectively.[3]

2.2 Directional solidification crucible

The silica (SiO_2) crucible, also known as quartz or amorphous silica, is the most common crucible material used for solar cell manufacturing. For mc-Si, the silica crucible is synthesised through slip-casting. The slip-casting process is illustrated in Figure 2.2. Natural quartz sand is melted to form silica glass. The silica particles are ground to form a powder before it is mixed with water and binder to make a silica slurry. The slurry is then poured into a plaster mould for the slip-casting process. The process involves absorbance of moisture from the slurry followed by annealing of the green body at high temperatures. The resulting silica crucible contains sintered quartz glass particles and is made to withstand the high temperatures from the liquid silicon (1414 °C [2]) to avoid failures and cracks in the silicon during the solidification process.[18][19]

As mentioned previously, mc-Si solidifies in contact with the crucible. As a result, the wetting from the molten silicon leads to sticking. This creates a strong adherence in which the crucible must be broken to release the finished ingot. Also, the thermal expansion coefficient of silica is lower than for silicon. This means that during cooling, the silicon material will experience a stronger shrinkage compared to the crucible. This contraction, combined with the wetting of the molten silicon, will induce stress and cracks.[20][19][21] A non-wetting behaviour for spontaneous detachment, as well as a negligible reactivity with the silicon ingot to avoid pollution, are the two main requirements for the crucible materials.[22] In absence of a satisfactory crucible material, the silica crucibles are coated with a layer of silicon nitride (Si_3N_4). The coating prevents the liquid silicon from sticking to the crucible walls and reduces possible cracking of the ingot due to stresses occurring during

the solidification.[18] It works as a releasing agent between the crucible and silicon ingot and also inhibits the diffusion of oxygen and other impurities into the melt from the crucible.[6]

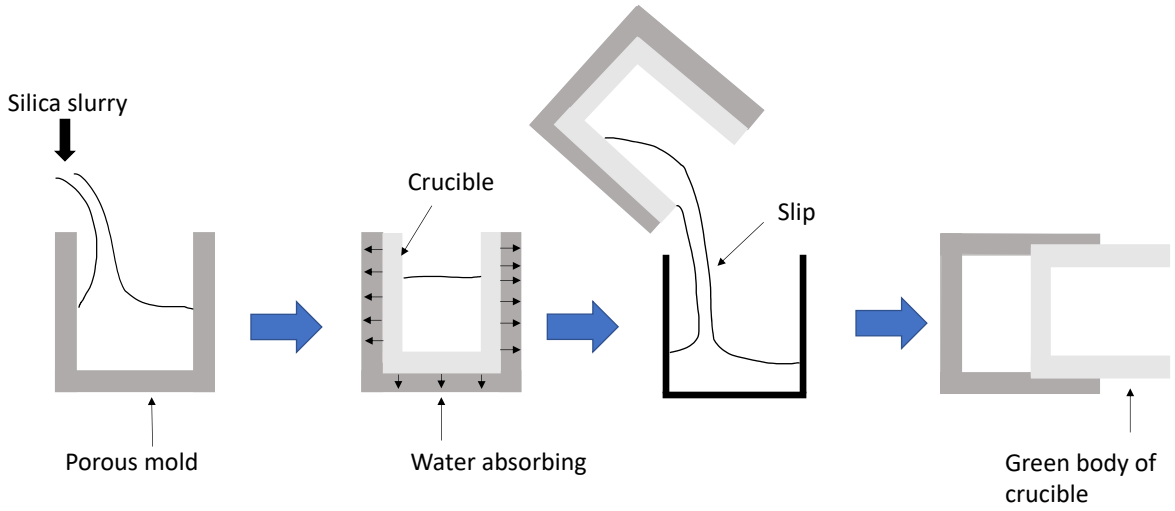

Figure 2.2: Schematic illustration of the slip-casting process of the silica crucible. The silica slurry is poured into a porous mould. The mould will extract the liquid and the crucible will compact along the mould walls. The finished green body is annealed at high temperatures.[23]

2.2.1 Silica

The structure of amorphous SiO_2 consists of SiO_4-tetrahedra where Si is surrounded by four oxygen atoms in a tetrahedrally coordinated system, see Figure 2.3a. The SiO_4-tetrahedra form a disordered three-dimensional network through bridging oxygen atoms, sharing the oxygen ions at the corners, shown in Figure 2.3b.[24][25] In contrast, crystalline silica has a three-dimensional network of SiO_4-tetrahedra coordinated in a repetitive and ordered system. An overview of observed silica phase transitions from the literature are given in Figure 2.4 and the unary phase diagram of silica is given in Figure 2.5. Amorphous silica is produced from the rapid cooling of liquid silica. Quenching prevents the silica from crystallising and results in a glassy and amorphous structure. The phase transformations of the silica crucible during directional solidification of mc-Si is one of the major causes of crucible failure. Research has shown that upon melting of the silicon when the crucible is exposed to temperatures above 1470 °C (depending on the pressure), part of the silica will transform from the glassy α-quartz phase directly into β-cristobalite with a cubic crystal structure, as can be seen in Figure 2.4. This aids the integrity of the crucible as the melting point of β-cristobalite (1710 °C) is below the peak temperature registered in the furnace used for the silicon ingot. However during cooling, post-solidification, the silica transitions from cubic β-cristobalite

to α-cristobalite with a tetragonal structure. This results in a volume decrease of 6.2 vol% leading to cracking and breakage of the crucible. This phase transformation can occur below 300 °C.[26]

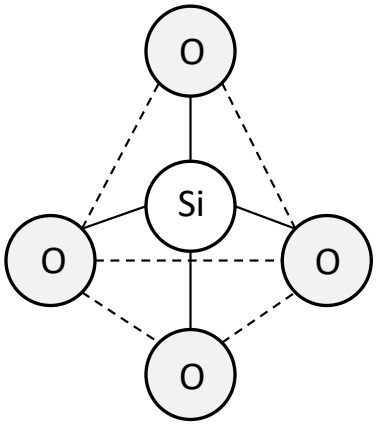

(a) The chemical structure of SiO_4. Si is surrounded by four oxygen atoms in a tetrahedrally coordinated system.[24][25]

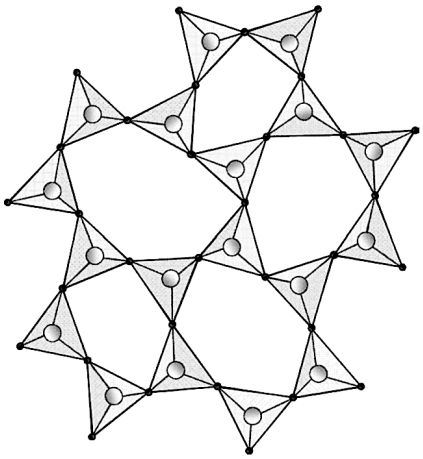

(b) The disordered arrangement of SiO_4-tetrahedra in amorphous silica.[26]

Figure 2.3: The chemical structure of silica.

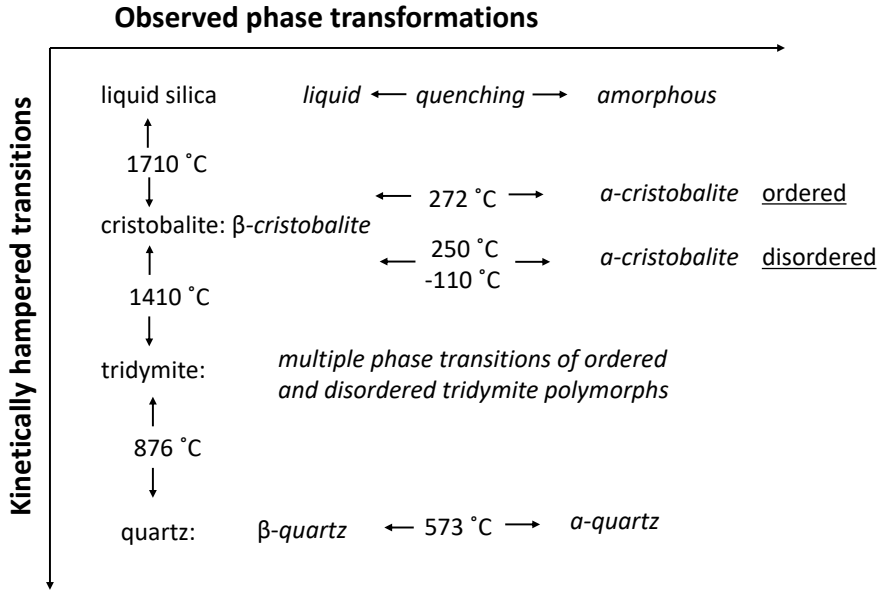

Figure 2.4: Observed phase transitions of SiO_2.[26]

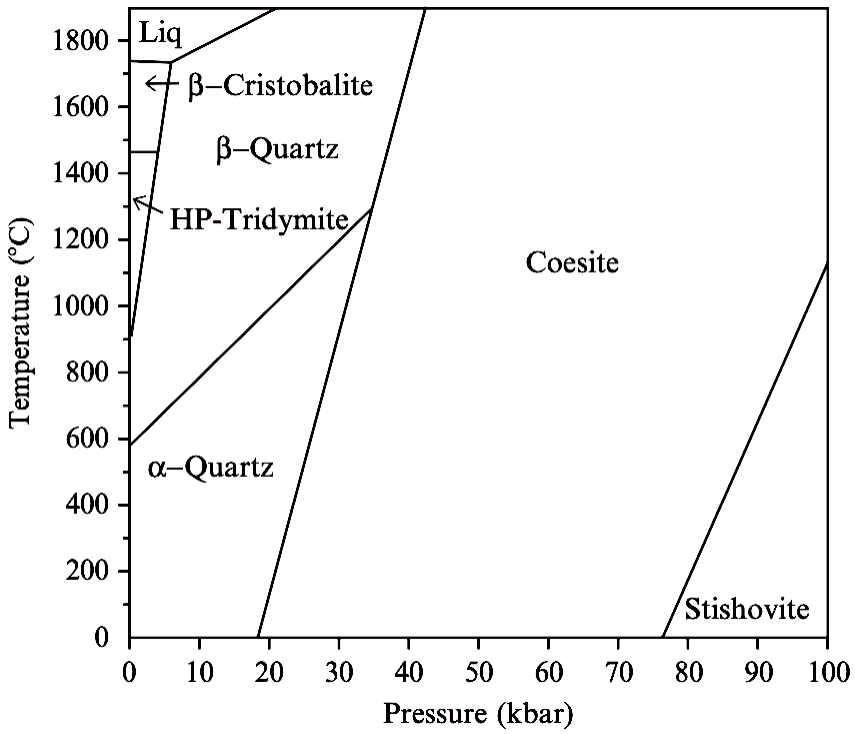

Figure 2.5: The unary phase diagram of the SiO_2 system.[27]

2.3 Effect of impurities

Impurities in semiconductors can be categorised as either dopants or contaminants. Impurities added intentionally to modulate the resistivity of the material are called dopants, while contaminants are incorporated during various process steps and can be detrimental to the material properties. The prevalent impurities are oxygen, nitrogen and carbon, in addition to metallic impurities. The presence of impurities will introduce new energy levels in the silicon energy bandgap. Depending on the location of these levels, the impurity can either increase the mobile charge density (energy levels close to the conduction or valence band) or introduce trap sites (deeper energy levels).[28] Impurities causing deeper states, also called trap levels, are very detrimental as they increase the probability of recombination due to these trapping sites. The trapping effect creates recombination centres, promoting the recombination of charge carriers, which reduces the minority carrier lifetime. Furthermore, this leads to a lower solar cell efficiency.[9][8] The minority carrier lifetime, τ [s], is defined as the average time a minority carrier is mobile before it recombines. It is given by the equation,

$$\tau_n = \frac{\Delta n}{U} \tag{2.1}$$

$$\tau_p = \frac{\Delta p}{U} \tag{2.2}$$

for electrons and holes, respectively, where Δn [cm^{-3}] and Δp [cm^{-3}] is the excess electron and hole density and U [cm^{-3}s^{-1}] is the net recombination rate.[28]

During the growth of mc-Si ingots, the contamination sources are mainly the feedstock, the furnace environment and the surfaces in direct contact with the silicon melt and solid (crucible walls).[9] The silicon oxide crucible and the silicon nitride coating have both been identified as dominant sources of impurities. However, the amount of impurities that end up in the mc-Si ingot from these sources is unknown. The impurity levels measured in a standard grade silica crucible from Vesuvius is given in Table 2.2.

Table 2.2: Impurities measured in a standard grade silica crucible from Vesuvius.[29][30]

Element	**Concentration [ppm wt]**
Mg	10
Al	950
Ti	60
Mn	2
Fe	120 (Kvande et al. 2009), 45.2 and 59.9 (Skarstad 2016)
Ni	1

Stokkan et al. reviewed reported contamination levels in the crucible and coating used for solidification of mc-Si. The results are summarised in Table 2.3. The impurity concentrations found in the silica crucible, coating and mc-Si ingot is given. The chemical state of these impurities and their interaction with grain boundaries and dislocations determine their impact on the solar cell properties.[31] Impurities can diffuse into the silicon melt as well as being incorporated into the crystal lattice during the crystallisation, giving an impurity concentration that increases towards the top of the ingot. Also, the impurities enter the ingot through solid-state diffusion from the crucible and coating into the solidified parts of the ingot. This leads to an edge region with a high impurity concentration and low bulk carrier lifetimes.[4]

Table 2.3: Impurity concentrations reported in the crucible, coating and mc-Si.[31]

Element	Crucible SiO_2 [ppm wt]	Coating Si_3N_4 [ppm wt]	Ingot [ppb wt]
Al	500	10	19
Cr	5	2	0.4
Cu	0.2	1	1
Fe	20	10	5
Ni	0.3	1	1
Ti	100	0.1	1
Zn	3	1.5	0.5
Mo	0.1	0.1	1
Co	0.05	30	0.05
Ca	50	5	-
Na	50	5	10
K	50	5	10

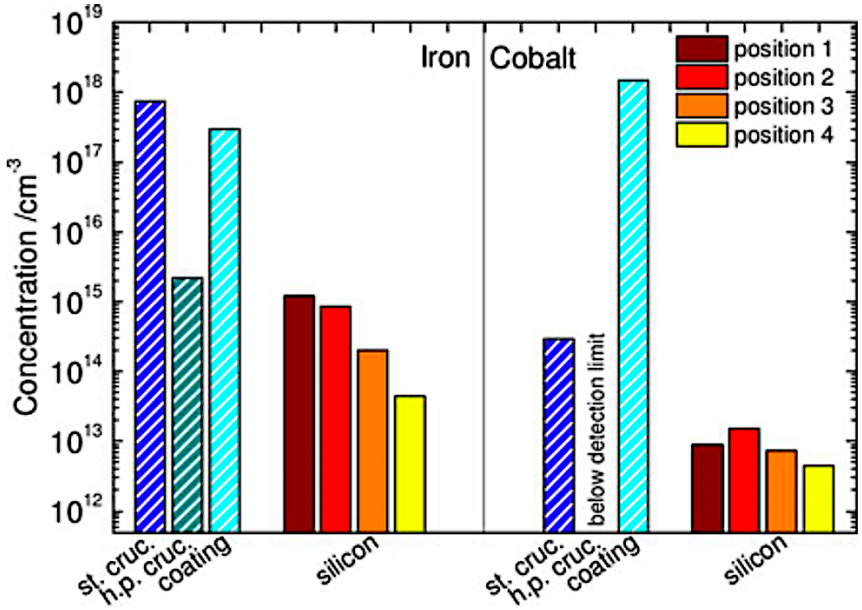

Figure 2.6: The iron and cobalt concentration measured in a standard crucible, high purity crucible and crucible coating powder, and the concentrations measured for different positions starting from the edge going horizontally towards the inner part of the silicon crystal.[10]

Improving the impurity of the crucible and coating is one approach to obtain mc-Si with a better electrical material quality as most of the impurities stem from these. Cleaner crucible materials have shown to improve the solar cell efficiency by increasing the carrier lifetime due to less contamination.[10][4][32] Schubert et al. measured the impurity concentrations of iron and cobalt in a standard crucible, a high purity crucible and the crucible coating, as well as in the silicon ingot. Their work, presented in Figure 2.6, clearly show a reduced iron and cobalt concentration in the high purity crucible. Standard crucibles can be considered as an infinite iron source, while high purity crucibles do not contribute much to the iron in-diffusion. The coating on the other hand, for high purity crucibles, will behave as a finite iron source. Cobalt is a typical impurity in the coating and works as a finite contamination source independent of the crucible.[10]

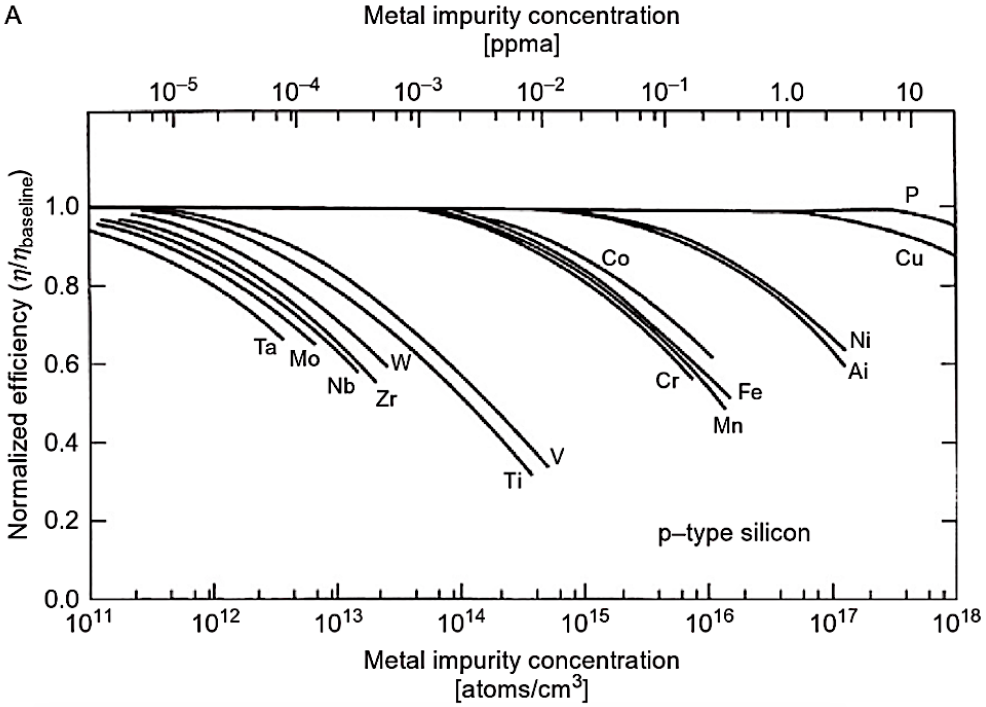

Figure 2.7: The efficiency loss due to metal contamination in p-type silicon.[33]

2.3.1 Impact of Fe contamination

Iron is considered one of the most detrimental impurities in silicon used in solar cells.[34] It is a deep level impurity with a large capture cross-section of electrons. Transition metals like iron are very harmful to the crystalline solar cells and will reduce the conversion efficiency, whether present as precipitates or isolated point-like impurities, due to the increased carrier recombination.[35] The efficiency loss due to metal contamination in p-type silicon is presented in Figure 2.7. Concentra-

tions of iron greater than 10^9 cm^{-3} will cause a significant reduction in the bulk lifetime.[11] Iron can easily be introduced into silicon crystals due to its high solubility and fast diffusion in silicon at high temperatures. It also has a low distribution coefficient.[9][8] The diffusivity, solubility and, as a result, the electrical activity and precipitation conditions of iron determines the behaviour and reactions of iron in silicon.[36] The iron is introduced from the feedstock and furnace environment as well as the crucible walls and silicon nitride lining that are in direct contact with the melt and solid silicon. Iron is also introduced during emitter diffusion and the firing of contacts at high temperatures.[9]

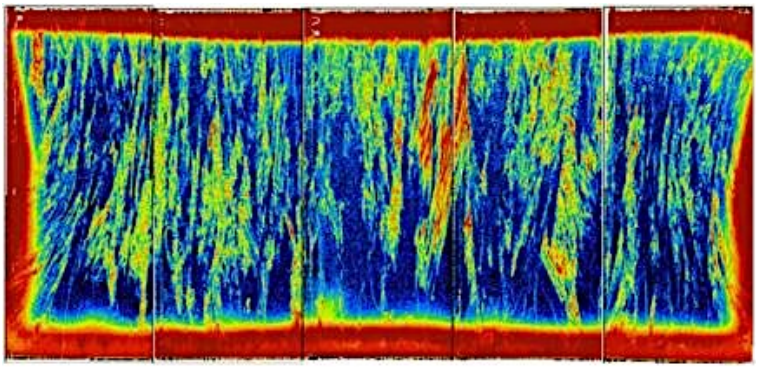

Figure 2.8: Typical minority carrier lifetime map of mc-Si. Areas with less contamination are blue and correspond to longer minority carrier lifetimes. The red area represents a lower lifetime and a higher contamination concentration.[37]

Generally, transition metals have lower distribution coefficients and can be removed more easily using directional solidification, gettering or heat treatment. Iron is an easy element to getter during diffusion of the phosphorus emitter since it is a fast diffuser.[9] In addition, most of the iron will exist in the silicon melt due to the low distribution coefficient and will, as a result, accumulate in the liquid phase at the top during solidification. However, since interstitial iron is a fast diffuser in solid silicon it will diffuse back into the bulk during cooling. In addition to this, the bottom and side parts of the ingot are still at high temperatures and fast diffusers like iron will diffuse from the crucible and into the solid silicon.[38][34] These edge zones where the contamination is high is referred to as red zones, see Figure 2.8. The bottom red zone is often broader because this is where the solidification commences and therefore the impurities will have a longer time to diffuse into the solid in this part.[5] Nærland et al. found strongly reduced minority carrier lifetimes in the vicinity of the edge (< 1 µs) of a p-doped silicon ingot. Their research also showed an increased iron concentration towards the edge, and occasionally high concentrations in the bulk.[39] Moreover, compared to interstitial iron, it is more challenging to remove iron precipitated at defects, dislocations and grain boundaries due to higher binding energies.[9] The chemical state of the iron

impurity is therefore of high importance when considering the impact of the solar cell properties. Previous studies have shown that in silicon, iron is present as interstitial iron or as metal silicide nano precipitates, mainly as $FeSi_2$.[40][41]

Iron impurities are very mobile in silicon solar cell wafers. The temperature-dependent diffusivity of iron in silicon wafers can be fit by the linear relationship given in Equation (2.3).[11][8]

$$D = (1.0^{+0.8}_{-0.4}) \cdot 10^{-3} exp\left(\frac{-0.67\ \text{eV}}{kT}\right)\ \text{cm}^2/\text{s} \tag{2.3}$$

2.4 Impurity transport mechanisms

Diffusion is the process of atoms moving from one lattice site to another. In solids, the atoms are constantly moving and changing positions. Two conditions are required for such movement of atoms; the atom must have enough energy to break the bonds to its neighbouring atoms to cause lattice distortion during the displacement, and there must be an empty adjacent site for the atom to move to. The diffusive motion increases for higher temperatures due to an increasing movement of the atoms.[42]

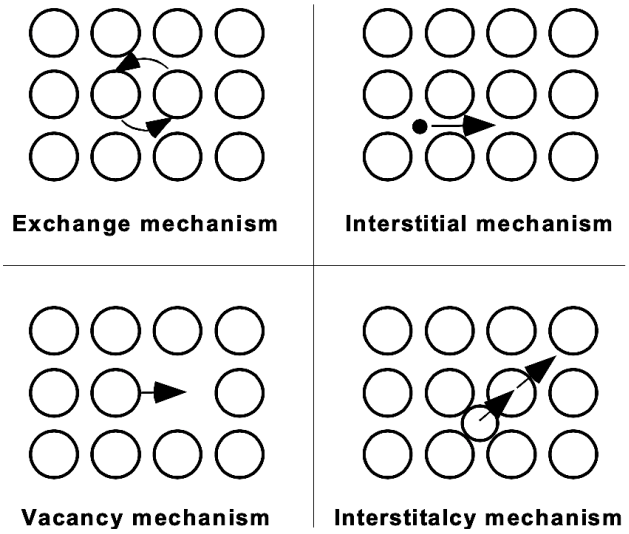

Figure 2.9: Transfer mechanisms for atomic diffusion; exchange, interstitial, vacancy and interstitalcy mechanism.[43]

The two dominating diffusion mechanisms in solids are vacancy and interstitial diffusion. Vacancy diffusion involves the movement of an atom to an adjacent vacant lattice site or vacancy, while in-

terstitial diffusion involves the migration of atoms from interstitial positions to empty neighbouring interstitial sites. Interstitial diffusion occurs for atoms that are small enough to fit into the interstitial positions and for metals the interstitial diffusion occurs more rapidly than vacancy diffusion.[42] Exchange and interstitalcy transfer mechanisms are also possible for atomic diffusion. The exchange mechanism is an exchange of adjacent atoms, while the interstitalcy mechanism involves an interstitial atom pushing a normal sited atom and displacing it into another interstitial site.[43] The four transfer mechanisms are illustrated in Figure 2.9. Iron is known to diffuse interstitially in silicon.[36][9][10]

2.4.1 Fick's 1st Law - steady-state diffusion

The mathematical theory of diffusion, given by Fick's first law, is based on that the transfer rate of the diffusing substance, through a unit area of a section, is proportional to the concentration gradient normal to the section. It is a diffusion model that describes the collective motion, flow of particles, from higher to lower concentrations. Fick's first law assumes steady-state conditions and is only valid for an isotropic medium, where chemical and physical properties are equal in all directions. When the diffusion flux, J, does not change with time the system is defined to have steady-state conditions. [44][42]

$$J = -D\frac{dC}{dx} \tag{2.4}$$

J [units/m^{2}s] is the diffusion flux, or the rate of mass transfer, in the x dimension. This represents the number of particles diffusing through the unit area per unit time. $\frac{dC}{dx}$ [units/m^4] is the concentration gradient and D [m^2/s] is the diffusion constant, the constant of proportionality. The concentration gradient can also be considered a driving force for the diffusive motion. The diffusion occurs in the opposite direction to that of increasing concentration, hereby the negative sign.[44] After a given time, the diffusion will reach a state of equilibrium and the concentration will be equal throughout the medium.

2.4.2 Fick's 2nd Law - non-steady-state diffusion

In a non-steady-state system, the diffusion flux and concentration gradient will vary with time. Fick's second law is derived for non-steady-state conditions and is a more realistic approach. This gives the diffusion equation,

$$\frac{\partial C}{\partial t} = \frac{\partial}{x}\left(D\frac{\partial C}{\partial x}\right) \tag{2.5}$$

where C [mol/m^3] is the concentration, D [m^2/s] is the diffusion coefficient, x [m] is the position and t [s] is the diffusion time. If the diffusion coefficient, D, is independent of concentration and constant in all directions, the equation simplifies to

$$\frac{\partial C}{\partial t} = \left(D \frac{\partial^2 C}{\partial x^2} \right) \tag{2.6}$$

The solution of Equation (2.6) can be obtained from Laplace transformations and specifying the following boundary and initial conditions:

(i) For t $>$ 0, C = C$_0$ at x = 0

(ii) For t = 0, C = 0 at x $>$ 0

The derivation of the solution can be found in "The Mathematics of Diffusion" by J. Crank.[44] The solution follows the error function, erf, and is given by

$$C = C_0(1 - erf\left(\frac{x}{2\sqrt{Dt}}\right)) \tag{2.7}$$

where C [mol/m^3] is the concentration at distance x [m] and time t [s], C_0 [mol/m^3] is the boundary concentration and D [m^2/s] is the diffusion coefficient. The diffusion coefficient is dependent on the temperature, but not the concentration and time. The error function is defined as

$$erf(z) = \frac{2}{\sqrt{\pi}} \int_0^z e^{-\eta^2} d\eta \tag{2.8}$$

where η is equal to

$$\eta = \frac{z}{\sqrt{2}\sigma} \tag{2.9}$$

where σ represents the standard deviation.

Figure 2.10 shows the relationship between the concentration profile and diffusion time. The diffusion coefficient follows the Arrhenius relation, see Equation (2.10), where D_0 [m^2/s] is a temperature-dependent preexponential, E_a [eV] is the activation energy for diffusion, k [eV/K] is the Boltzmann constant and T [K] is the absolute temperature.[42] The Arrhenius equation can also be expressed in terms of E_a [J/mol] and the gas constant, R [J/molK]. Rewriting the Arrhenius relation using the natural logarithm gives Equation (2.11) where ln(D) can be plotted against the inverse of temperature, 1/T, to find the slope, corresponding to -$\frac{E_a}{kT}$, and the y-intercept value, corresponding to ln(D_0).

$$D = D_0 exp\left(-\frac{E_a}{kT}\right) \tag{2.10}$$

$$ln(D) = ln(D_0) - \frac{E_a}{kT} \tag{2.11}$$

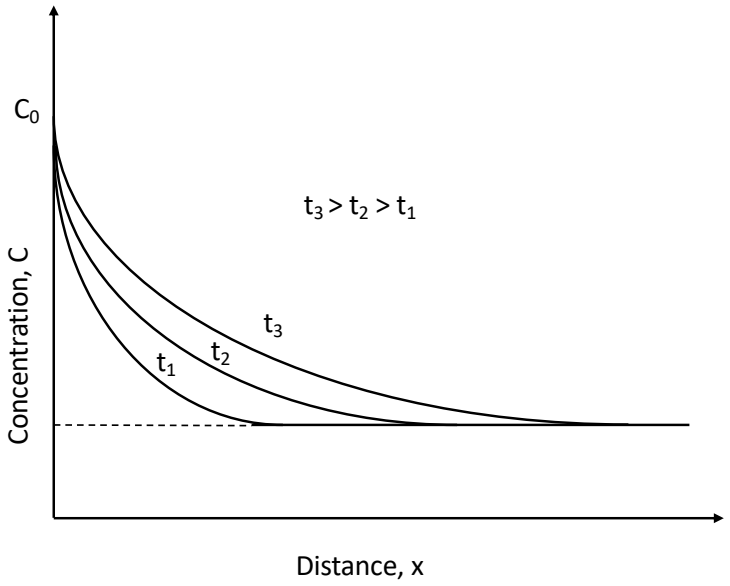

Figure 2.10: The relationship between the concentration profile and diffusion time, t, at a constant temperature. C_0 is the boundary concentration and x is the distance.[44]

2.4.3 Solubility

The solubility is the maximum concentration of an impurity that can be dissolved at a given temperature and is found from the equation

$$S = S_0 exp\left(\frac{-H_s}{kT}\right) \text{ for } T < T_{eut} \tag{2.12}$$

where S_0 [cm^{-3}] is a temperature-independent preexponential factor, H_s [J] is the solution enthalpy, k [J/K] is the Boltzmann constant and T [K] is the temperature.[38] This is only valid for temperatures below the eutectic temperature which is the lowest melting point of a mixture of com-

ponents. The solubility is very relevant when evaluating the solid diffusion of an atom specie since it gives the maximum concentration that can be dissolved in the host material at given conditions. Any concentration above this will give precipitations forming other solid phases or compounds of different composition.[38] In the temperature range 800-1200 °C, the solubility of iron in intrinsic silicon can be fit by the linear relationship given in Equation (2.13).[8]

$$S = (8.4^{+5.4}_{-3.4}) \cdot 10^{25} exp\left(\frac{-2.86 \pm 0.05 \text{ eV}}{kT}\right) \text{ cm}^{-3} \tag{2.13}$$

2.4.4 Segregation

At an interface between two media with different impurity concentrations, the impurity will segregate and move across the interface due to different solubilities in the two media. The segregation will continue until the concentrations at the interface equal the partition or segregation ratio, see Equation 2.14. Most of the impurities in silicon tend to segregate into the liquid phase during the solidification process due to higher solubility in liquid silicon rather than in solid silicon. The solubility is dependent on the size of the impurity atom and the solubility in silicon decreases with increasing atomic size. The equilibrium segregation coefficient is defined as

$$k_{eq} = \frac{C_S}{C_L} \tag{2.14}$$

where C_S [mol/m^3] and C_L [mol/m^3] are the impurity concentrations in the crystal silicon and molten silicon, respectively. The equilibrium segregation coefficient assumes complete mixing in the liquid and no diffusion in the solid.[38] Incomplete mixing is a more realistic assumption. The effective segregation coefficient takes this into account and is defined as

$$k_{eff} = \frac{1}{k_{eq} + (1 - k_{eq}) exp(\frac{-v\delta}{D})} \tag{2.15}$$

where v [m/s] is the growth velocity, D [m^2/s] is the diffusion coefficient of the impurity in the melt and δ [m] is the boundary layer. Coletti measured the effective segregation coefficient, k_{eff}, of Fe in mc-Si to be 1.5x10^{-5}.[38][45]

Chapter 3

Literature Review

The following chapter is a literature review on diffusion studies in quartz. A general overview of the diffusion behaviour of different elements measured in quartz is summarised and compared to create a reference database to the experimental work of this thesis.

3.1 Introduction

Quartz is a very abundant mineral on Earth that can contain small amounts of transition metals, aluminium and alkalis.[46][47] As a result, quartz crucibles used in the production of mc-Si (for solar cells) contain impurities that can diffuse into and contaminate the silicon. These impurities are detrimental to the silicon quality and solar cell efficiency. Diffusion studies in quartz are therefore of high importance in order to gain a better understanding of how to reduce the contamination from the crucible and coating to the solid silicon.

This chapter reviews a collection of diffusion studies of different elements in quartz. A summary of diffusion data in quartz materials is given in Table 3.2. As this literature data is found from experiments conducted with different quartz materials of different morphology and thickness, it is unclear as to what extent the different data are useful for the description of the porous crucibles. However, diffusion data for both crystalline and amorphous quartz is given for comparison.

3.2 Diffusion in quartz

Amorphous materials are described to be in a thermodynamical state of non-equilibrium, while crystalline materials are in a state of equilibrium. The silica matrix is further described in Chapter 2.2. Due to the non-equilibrium state, the diffusion mechanisms of amorphous materials can not be

expected to be the same as the ones established for crystalline materials. Furthermore, the diffusion mechanisms in amorphous materials are not as well understood as the mechanisms in crystalline materials and there are few data available.[48] It is hard to envision point defects and on-site hopping of single atoms in the disordered structure of amorphous materials. However, the diffusion data reported in this chapter shows that Fick's law of diffusion applies to some amorphous materials.

In crystalline quartz, diffusion can occur either through volume diffusion through the lattice, along grain boundaries or through surface diffusion. Surface diffusion and grain boundary diffusion are related to surface and line defects. For polycrystalline materials, grain boundary diffusion is the dominant diffusion mechanism at low temperatures. Volume diffusion is related to the existence of lattice defects (vacancies and interstitial ions) and is the dominant diffusion mechanism at higher temperatures.[49] These diffusion mechanisms are further described in Chapter 2.4. Vacancy diffusion is more common for metals and alloys, whereas interstitial diffusion is more dominating in nonmetallic solids, like silica.[50]

Impurities in quartz can be carried in three different forms; fluid inclusions, minerals inclusions and as structural impurities. Liquid inclusions are common for hydrothermal quartz while mineral inclusions are more commonly found along the grain boundaries. Trace elements confined to the lattice structure, substitutional or interstitial, are called structural impurities. These impurities are especially difficult to remove so the quartz quality highly depends on the amount of these.[49]

Figure 3.1 illustrates the most common defect types in crystalline quartz. The most important point defect is the substitution of Si^{4+} by trivalent cations like Al^{3+}, Fe^{3+}, B^{3+}, As^{3+} and Ga^{3+}. The lower charge of the trivalent cations creates a charge deficit which is balanced by incorporating a monovalent cation in interstitial positions or by substituting another Si^{4+} with a pentavalent cation. The interstitial cations are favourably small such as H^{+}, Li^{+}, Na^{+}, Cu^{+} and Ag^{+}.[51][49] The substitutional and interstitial impurities accommodate the lattice and compensate electrically to reach charge neutrality. The incorporation of structural trace elements can, therefore, be divided into three modes; compensated substitution, single substitution and double substitution. These are illustrated in Figure 3.2.[49][52]

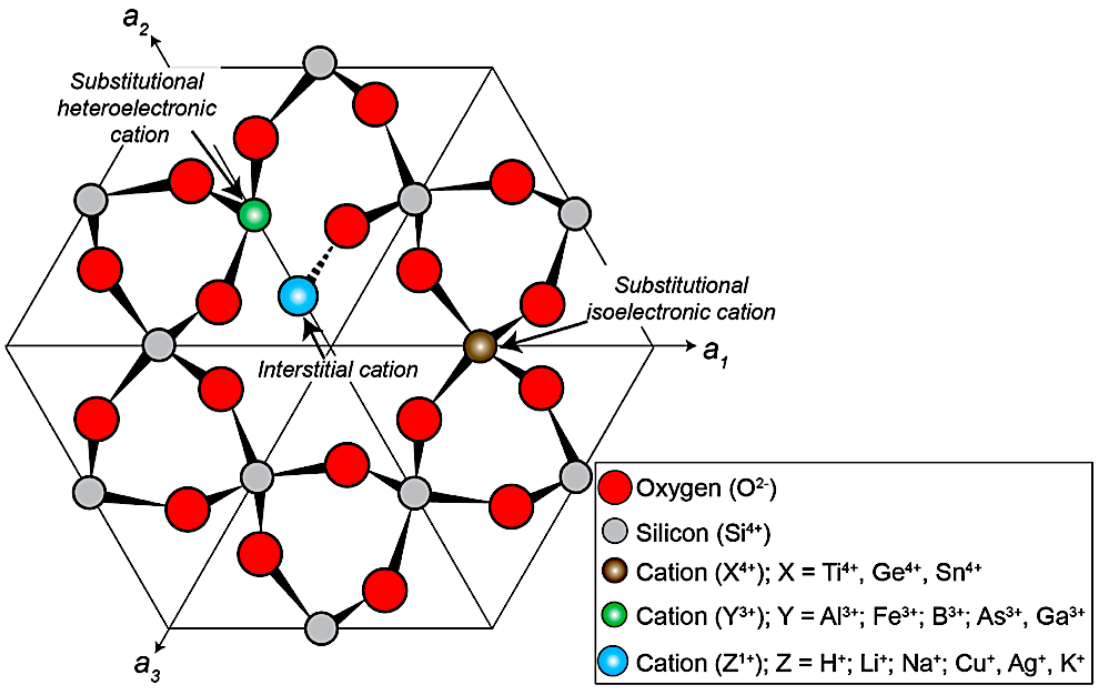

Figure 3.1: The most common defect types in crystalline quartz.[51]

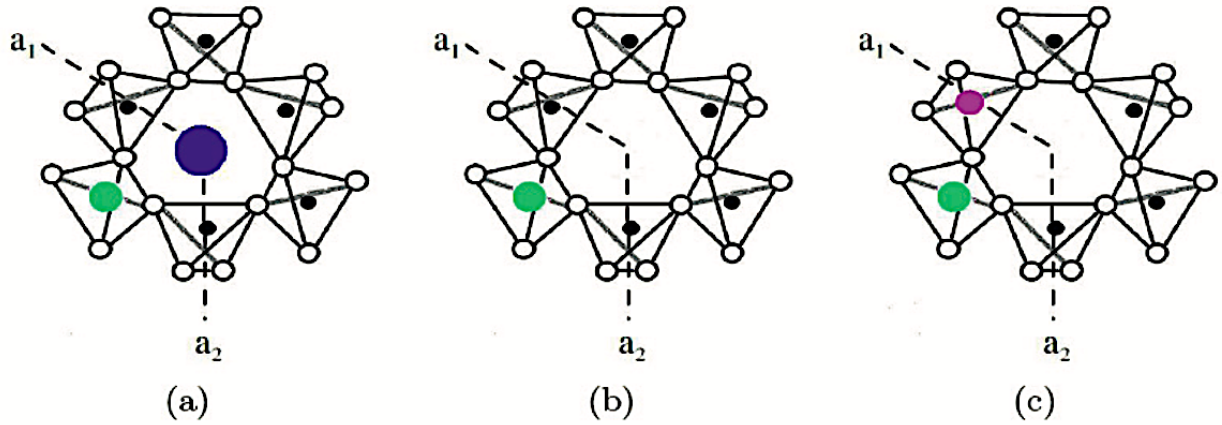

Figure 3.2: The three modes of incorporating structural trace elements: a) compensated substitution: a trivalent cation replaces Si^{4+} and is balanced by the incorporation of a monovalent cation into an interstitial position (blue) b) single substitution: Si^{4+} is substituted by another tetravalent cation c) double substitution: two Si^{4+} ions are replaced by one trivalent cation and one pentavalent cation.[49][52]

Diffusion of cations in quartz is dependent on the silica polymorph and the typology of the impurity. Foreign ions will accommodate easier in more open structures, voids and cracks. Cristobalite and

tridymite are more open types of silica phase structures compared to quartz. Their densities are both lower than the density of quartz, see Table 3.1.[53] The estimated void space per unit cell for β-cristobalite is 48.4 % and 51.7 % for β-tridymite, while amorphous silica has an estimated 57 % void space per unit cell volume.[26] The voids in cristobalite and tridymite can accommodate ions such as Na^+, Ca^{2+} and K^+. As a result of the more open structure, the solubility is also higher in these silica phases compared to quartz.[49] The structure of amorphous silica is also more open and has a similar density to both cristobalite and tridymite. Therefore it is reasonable to assume that amorphous silica also has a higher solubility and that diffusion will occur more easily compared to the diffusion in quartz. However, the disordered structure will lead to inhomogeneous distributions, locally decreased/increased densities and consequently altered physical properties.[26]

Table 3.1: The densities, ρ [g/cm^3], of different silica structures.[54][27][30]*This work

Silica phase	**Density, ρ [g/cm^3]**
Cristobalite	2.33
Tridymite	2.28
Quartz glass	2.20
Quartz	2.66
Quartz crucible (Skarstad)	1.90
Quartz glass (Skarstad)	2.23
Quartz crucible*	1.95
Quartz glass*	2.20

According to literature, experimental observations usually find lower activation energies for diffusion in silica compared to other solids. This can be accounted for by the open structure of the silica matrix.[50] The activation energy given in the diffusion equation can be interpreted as the potential barrier that is required for diffusion to occur, i.e. movement of an atom from one interstitial site to another.[50] The potential energy can be described by the equation,

$$E_a = 8\pi G_{r_D}(r - r_D)^2 \tag{3.1}$$

where G [Pa] is the elastic shear modulus, r_D [m] is the radius of the interstitial cavity and r [m] is the radius of the diffusing atom. Equation (3.1) indicates that the activation energy is lower for diffusing atoms with a smaller radius. This means that smaller ions will diffuse more easily due to smaller potential energy barriers.[50] Moreover, in addition to the cation radius, the diffusion in

quartz also depends on the lattice position and the charge. As mentioned, alkaline ions like Li^{+} and Na^{+} will diffuse into interstitial positions. Such interstitial elements will accommodate the vacancies created by lattice defects where there may be a balance charge anomaly in the structure. They have higher diffusivities and are easily mobilised in the structure, compared to other substitutional elements such as Al^{3+} and Ti^{4+}. This is due to the relative weakness of purer ionic bonds compared to ionic-covalent bonds to the substituted elements.[52] Elements such as Al^{3+} will substitute for Si^{4+} which requires a necessary charge compensation. These elements are therefore dependent on the alkali compensator ion. Larger alkali ions will have a weaker attraction to the surrounding oxygen atoms, resulting in more lattice distortion. This will aid the mobilisation of Al and increase its diffusivity.[49] Na compensated Al diffusion appear to have lower activation energies compared to Li compensated Al diffusion. Na is a larger alkali ion and will give more lattice distortion resulting in easier migration of Al. In contrast, Li is smaller and has a stronger attraction to the surrounding oxygen atoms reducing the mobility of Al.[55]

Table 3.2: Summary of diffusion data in quartz. The temperature-dependent preexponential, D_0 [cm^2/s], and the activation energy, E_a [eV], is given for different elements measured in quartz.

Element	**Research**	D_0 **[cm^2/s]**	E_a **[eV]**	**SiO$_2$ structure**
Al	Cherniak et al.[56]	2.48x10^{-7}	2.07	Crystalline
Ca	Frischat[47]	1x10^{5}	2.95	Crystalline
Co	Schubert et al.[10]	1x10^{3}	3.05	Amorphous (crucible)
Fe	Atkinson et al.[24]	6x10^{-3}	3.00	Amorphous
Fe	Istratov et al.[14]	2.2x10^{-2}	3.05	Amorphous
Fe	Kononchuk et al.[57]	1x10^{-3}	2.8	Amorphous
Fe	Ramappa et al.[13]	4x10^{-8}	1.51	Amorphous
Fe	Schubert et al.[10]	50	3.05	Amorphous (crucible)
Fe	Skarstad[30]	2.6x10^{-9}	0.47	Amorphous
Fe	Skarstad[30]	1.2x10^{-4}	1.53	Amorphous (crucible)
H_2	Lee et al.[58]	5.7x10^{-4}	0.45	Amorphous
K	Verhoogen[59]	18x10^{-2}	0.33	Crystalline
Li	Verhoogen[59]	6.9x10^{-3}	0.21	Crystalline
Na	Verhoogen[59]	3.6x10^{-3}	0.25	Crystalline
Ne	Cherniak et al.[60]	1.6x10^{-10}	1.19	Crystalline
Ne	Begeal et al.[61]	5.1x10^{-5}	0.41	Amorphous
Ni	Ghoshtagore[48]	7.2x10^{-10}	1.61	Amorphous
O_2	Norton[62]	2.9x10^{-4}	1.17	Amorphous
Ti	Cherniak et al.[46]	7x10^{-4}	2.84	Crystalline
Ti	Bromiley et al.[46]	2x10^{-3}	2.03	Crystalline

3.2.1 Metals

Iron

The diffusion behaviour of iron in silicon dioxide materials has been studied by Atkinson et al.[24], Kononchuk et al.[57], Ramappa et al.[13] and Schubert et al.[10] among others. It was observed that the diffusion of iron in SiO_2 followed the Arrhenius relationship. Their results are presented in Table 3.2. Apart from Schubert et al., who modelled the diffusion coefficient in slip-cast silica crucibles, their studies were based on quantitative analysis looking at diffusion of iron in amorphous silica glass. It can be seen from Figure 3.3 that their data agree between 1000-1200 °C within two orders of magnitude.[14] Istratov et al. performed a least-square fit analysis of these literature data to achieve the following diffusion equation for iron in silicon dioxide,

$$D = 2.2 \cdot 10^{-2} exp\left(\frac{-3.05 \text{ eV}}{kT}\right) \text{ cm}^2/\text{s} \tag{3.2}$$

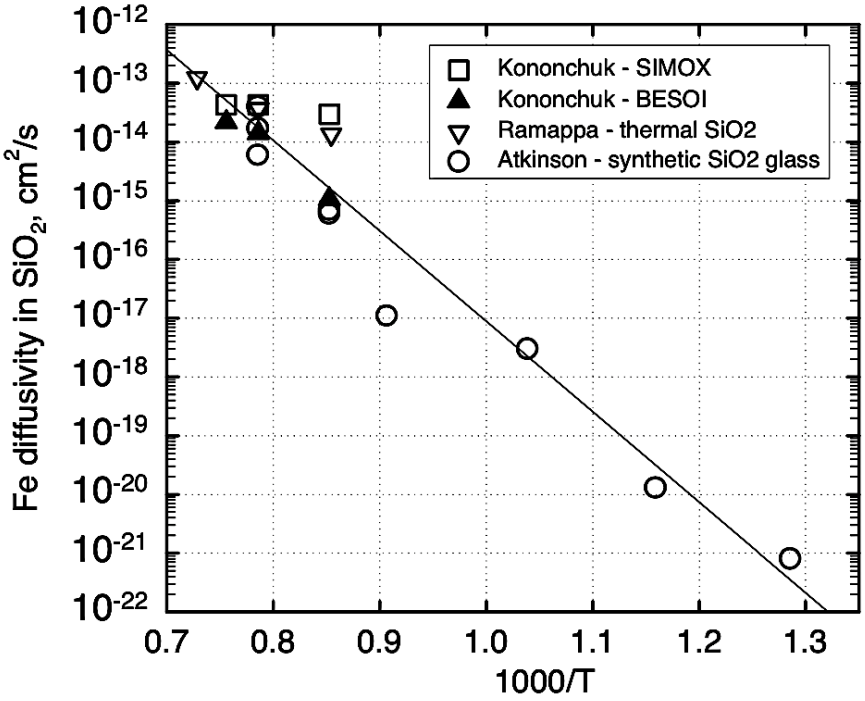

Figure 3.3: Literature data on iron diffusion in silicon dioxide.[14]

Schubert et al. measured a significantly higher diffusion coefficient for iron in the amorphous slip-cast SiO_2 crucible compared to the iron diffusion measured in quartz glass. This was explained from

the material properties of the crucible, it is highly porous and has a lower density than quartz glass. Figure 3.4 shows a secondary electron micrograph, from the master thesis by Skarstad, of a crucible sample revealing the pores and grains in the microstructure.[30] Skarstad studied the diffusion of iron in both quartz crucibles and quartz glass. The density of quartz glass was measured to be 2.23 g/cm^3 and 1.9 g/cm^3 for the slip-cast crucible. The results from Skarstad's diffusion studies support Schubert's research with a higher reported diffusivity in the crucible compared to in the quartz glass. Skarstad measured a difference of one order of magnitude between the diffusion profiles of the slip-cast crucible and quartz glass, see Table 3.2.[30]

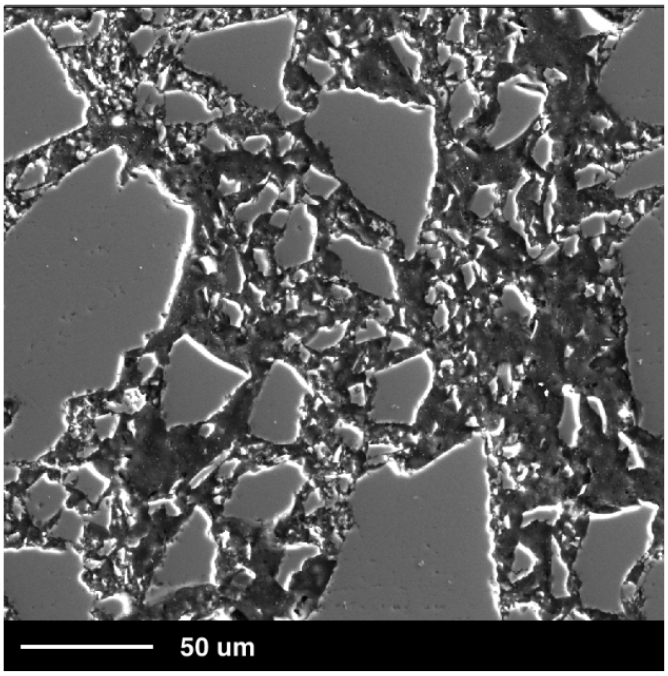

Figure 3.4: Secondary electron micrograph of the cross-section of a polished slip-cast crucible sample from the master thesis by Skarstad.[30]

The thermodynamically non-equilibrium state of amorphous materials means that the diffusion mechanisms can not be expected to be the same as those established for ordered crystalline materials. According to Atkinson et al.[24], iron is assumed to only behave as point defects in silica and the diffusion of iron will then, therefore, depend on the density of these point defects and their thermal diffusivity. One such interaction is the substitution of Si^{4+} by Fe^{3+} in the tetrahedrally coordinated positions. The negatively charged defects are compensated by other defects with a positive charge, such as oxygen vacancies. Introducing iron to SiO_2 will then result in the production of oxygen vacancies and the diffusion coefficient of iron would be determined by the diffusion of these defects.[13][24] Due to this, the presence of water will increase the diffusion of iron by

affecting the rate of the diffusion of oxygen vacancies.[49]

As mentioned, the activation energy given in the diffusion equation is related to the potential barrier for diffusion to occur. The activation energy can be interpreted as the energy required for an atom to jump from one interstitial site to another.[50] Ramappa et al. observed that for diffusion in SiO_2, the activation energy decreased with decreasing atomic sizes of the diffusing species which corresponds well with this theory.[13] Due to this observation, Ramappa suggests that the mechanisms of iron diffusion in SiO_2 is a combination of both interstitial and vacancy diffusion.

Cobalt

In addition to iron, Schubert et al. also modelled the diffusivity of cobalt in the slip-cast crucible used in the production of mc-Si. Similarly to iron, the measured diffusivity of cobalt was also significantly higher compared to diffusion data in other quartz materials. This again was explained by the porous structure of the amorphous quartz crucible material. Cobalt is not a common element in the silica crucible, but it is commonly found in the silicon nitride coating.[10]

Aluminium

Cherniak et al. studied the diffusion of aluminium in natural and synthetic crystalline quartz. Diffusion profiles were measured using nuclear reaction analysis. The results showed a sufficiently slow diffusivity of Al through the quartz lattice with a D_0 of 2.48x10^{-7} cm^2/s and an E_a of 2.07 eV.[56] Similarly to Fe^{3+} ions, Al^{3+} is also expected to substitute Si^{4+} in the tetrahedrally coordinated positions, followed by a charge compensation.[24]

Titanium

The diffusion of titanium in natural and synthetic crystalline quartz was studied by Cherniak et al. using a TiO_2 powder source. The diffusion profiles were obtained using Rutherford backscattering spectrometry. Similar diffusion properties were found for both synthetic and natural quartz. The result showed a somewhat slower diffusion compared to aluminium. According to Figure 3.1, Ti ions most likely will substitute for Si in the lattice, similar to Al and Fe. However, Ti^{4+} has the same charge as Si^{4+} giving an isoelectronic substitution, also called single substitution, compared to Fe^{3+} and Al^{3+} where the effective negative charge must be compensated by other defects. The higher charge of Ti^{4+} compared to Al^{3+} might contribute to the slower diffusivity.[46][24][13]

Figure 3.5 is a summary, by Cherniak et al., of diffusion data in crystalline quartz.[46][55] It shows that the diffusion of Ti is significantly slower than for the diffusion of the alkalis (Na, Li, K studied

by Verhoogen[59]), but faster than oxygen diffusion in quartz under dry conditions and the self-diffusion of Si.[46] Figure 3.6 is another summary by Cherniak et al. that includes Arrhenius lines for diffusion in quartz under nominally dry conditions. It was found that generally, the diffusion coefficients of higher charged cations are lower than for lower charged cations (at the same temperature). Similarly, higher charged cations also have higher activation energies for diffusion.[63]

Bromiley et al. studied the grain boundary diffusion of titanium in polycrystalline quartz. A slow lattice diffusion and fast grain boundary diffusion was revealed from the resulting diffusion profiles. Over the temperature range 1000-1400 °C, the grain boundary diffusion of Ti was found to be 3-4 orders of magnitude faster than the lattice diffusion of Ti.[64] This corresponds well with the diffusion theory discussed earlier which stated that grain boundary diffusion is the dominating mechanism for polycrystalline materials.

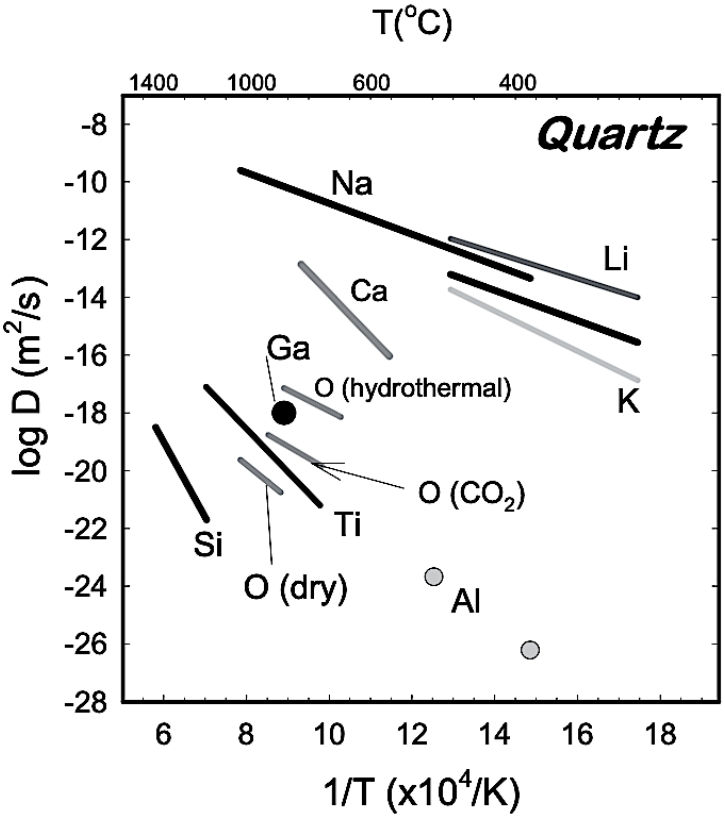

Figure 3.5: Summary of diffusion data in crystalline quartz by Cherniak et al.[55][46]

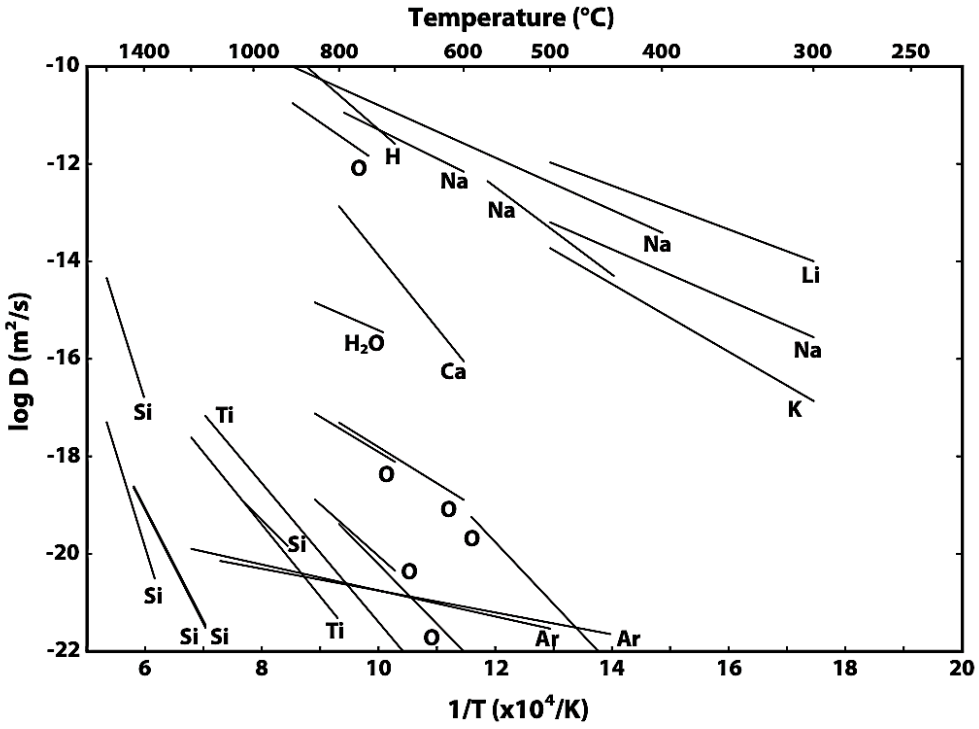

Figure 3.6: Summary of diffusion data in quartz under nominally dry conditions by Cherniak et al.[63] The diffusion coefficients are generally lower and the activation energies higher for higher charged cations.

Nickel

Nickel diffusion in amorphous SiO_2 films was studied by Ghoshtagore in the temperature range 1100-1490 °C. According to Ghoshtagore, the activation energy of nickel diffusion is the same for all types of SiO_2 studied which means that it is the same point defect in every material that is responsible for the diffusion. In other words, it seems like nickel migrates by the same point defect in all types of amorphous SiO_2 studied. However, no specific diffusion mechanism for nickel was discussed.[48]

3.2.2 Alkali and alkaline earth metals

Li, Na and K

The diffusion coefficients of the alkalis elements Li^+, Na^+ and K^+ were measured in natural quartz crystals in the temperature range 300-500 °C by Verhoogen. It was found that the diffusion most likely occurred through the crystal lattice and not through mechanical defects (grain boundaries and cracks).[59] The alkali metals Li, K and Na have the same charge, but different atomic sizes. The influence of the atomic size can be seen in Figure 3.5 where K is the largest atom and has the lowest

diffusion coefficient, while Li is the smallest atom and has the highest diffusion coefficient.[63]

Diffusion of larger ions cannot happen without distortion of the lattice to make room for the ion or to occupy preexisting holes. The energy requirements and the diffusion rates would be very sensitive to the ionic sizes if the diffusing ion is distorting the lattice. This was also shown in Equation (3.1) and discussed by Ramappa earlier, where it was observed that decreased atomic sizes gave decreased activation energies of diffusion.[13] Verhoogen discussed how this is true to some extent, however not for the larger univalent ions, like K^+, which diffuse more rapidly than smaller bivalent or trivalent ions. This can indicate that it is more common for foreign ions to diffuse through preexisting holes, such as vacant oxygen lattice sites. The oxygen vacant sites are formed by removing an oxygen ion to an interstitial position. The effective positive charge created will repel any invading positive ion. This explains why bivalent ions, even of smaller sizes (e.g. Mg^{2+}), will diffuse more slowly than larger univalent ions like Na^+ and K^+, due to their higher positive charge.[59]

Calcium

Calcium diffusion in natural quartz crystals was measured by Frischat. It was found that the Ca diffusion was slower than the Na diffusion in quartz due to a much higher activation energy (2.95 eV for Ca compared to 0.25 eV for Na (Verhoogen)), in common with Fe, Al, and Ti. Frischat found that the diffusion of Ca is about 3 orders of magnitude slower than Na (Verhoogen) at 600 °C.[47] From Figure 3.5 and 3.6 it can be seen that the diffusion of Ca is significantly slower than the diffusion of all of the measured alkalis. This is consistent with the trend, discussed above, applied for divalent and univalent cation diffusion. The divalent Ca^{2+} diffusion is expected to diffuse slower than the univalent alkalis due to a stronger repelling force through the lattice.[55]

3.2.3 Gases

Neon

Begeal et al. studied the diffusion of neon in amorphous SiO_2 substrates in the temperature range 25-500 °C, while Cherniak et al. studied the diffusion of neon in single quartz crystals in the temperature range 400-1050 °C.[61][60] The activation energy for neon diffusion in amorphous quartz was measured to be 0.41 eV, while in crystalline quartz it was measured to be 1.19 eV. Comparing the activation energies of the two studies, it is clear that for amorphous quartz it is much lower. This corresponds to the theory discussed in the sections above, i.e. diffusion in more open structures occur more easily and has lower potential energy barriers.

Oxygen

The data for oxygen in Table 3.2 are resulted from measuring the diffusion of molecular oxygen, O_2, in silica over the temperature range 950-1080 °C.[62] Through several experiments, the activation energy for O_2 diffusion has been estimated to values ranging from 1.17-1.35 eV. The research has shown that molecular oxygen diffuses in silica without any appreciable interactions with the matrix and that oxygen diffuses as a molecule through the interstitial diffusion mechanism.[50]

Chapter 4

Experimental

This chapter gives an overview of the methods that were used to obtain the results from the experiments. The setup and instruments used in the different measurements are described as well as the approach.

4.1 The diffusion couple technique

The diffusion couple technique is an experimental approach to study a multicomponent system. A solid-state diffusion couple involves joining two (or more) materials together, obtaining intimate contact between the two faces of the materials.[42] To achieve such intimate contact that diffusion will occur, the couple components are commonly ground and polished flat before they are joined together. The couple is then heat treated and annealed at a temperature for an extended time period (below the melting temperature) before they are cooled to room temperature. Quenching can be desirable to freeze the equilibrium state obtained at a high temperature. Various atmospheres can be used depending on the materials, e.g. vacuum or inert gas.[65]

To measure the diffusion coefficient of iron in amorphous SiO_2 heat treatments of diffusion couples consisting of slip-cast crucible, steel, and quartz glass were performed in a vacuum atmosphere using temperatures ranging from 900-1300 °C. Based on results from similar studies, the samples were not quenched, but air cooled to avoid the quartz glass from breaking.[30]

4.1.1 Sample preparation

Samples of a coated standard grade slip-cast SiO_2 crucible (provided by Vesuvius) were cut using a core drilling machine (by Strands) with a 25 mm bore, see Figure 4.1. The thickness of the samples was approximately 12 mm, with some variations. The samples were washed with soap and water,

followed by ethanol, before they were dried. The silicon nitride coating was removed by scraping it off using a clean plastic bit. This was to solely observe the diffusion of iron in the amorphous silica material and not in the silicon nitride coating. The samples were not polished to avoid any metal contamination.

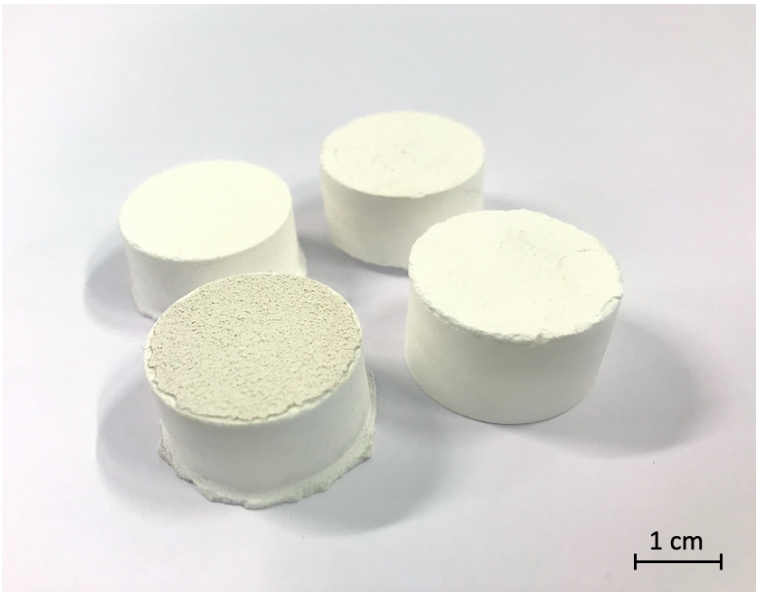

Figure 4.1: Samples of the Vesuvius slip-cast crucible. The sample in the front left is coated.

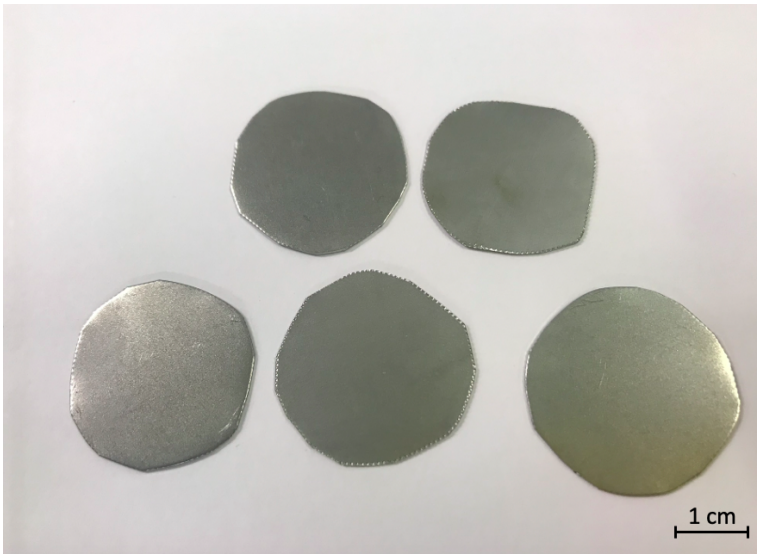

Figure 4.2: The steel samples used as the iron source in the diffusion experiments.

Low-carbon steel (NS-EN 10130) was used as the iron contamination source. The steel samples

were cut from a Smith Steel cold-rolled plate DC01 (0.5 mm x 1000 mm x 2000 mm), using a plier, into circles with a large enough diameter to cover the entire surface area of the silica samples (approximately 25-30 mm), see Figure 4.2.

Pure synthetic quartz glass samples (from Heraeus) with a 25 mm diameter and 5 mm thickness were prepared by the glassblower workshop at NTNU, see Figure 4.3. The quartz glass was used as a reference to the slip-cast crucible to compare the diffusion of iron in both silica materials. The typical concentrations of trace impurities in synthetic Heraeus quartz glass is given in Table 4.1. Quartz glass is a material with a very low thermal expansion coefficient and can withstand rapid thermal changes. At 0-900 °C, the mean thermal expansion coefficient is only 4.8x10^{-7} K^{-1}.[66] The softening temperature of quartz glass is 1730 °C and the maximum working temperatures are 1150 °C (continuous) and 1300 °C (short-term). According to the producer, the quartz glass has hardness values of 5.5-6.5 on the Mohs scale.[66]

Table 4.1: Typical concentrations of trace impurities in Heraeus quartz glass (HOQ) [ppm wt].[66]

Element	Al	Ca	Cr	Cu	Fe	K	Li	Mg	Na	Ti
Concentration [ppm wt]	20	1	0.1	0.1	0.8	0.8	1	0.1	1	1

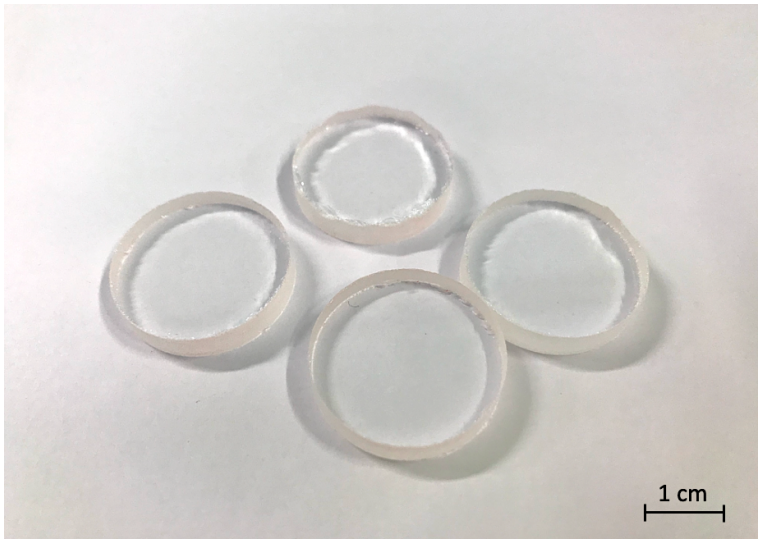

Figure 4.3: Quartz glass samples prepared by the glassblower workshop at NTNU.

Based on results from similar studies, the expected diffusion length of iron in amorphous quartz is in micrometres.[30] Compared to the much thicker samples, this means that the diffusion would

only occur in a small part of the sample. The variation in thickness between the different samples were, therefore, not a complication as it would not affect the iron concentration depths obtained from the diffusion experiments.

4.1.2 Heat treatment

Heat treatments were performed in a tube furnace (GSL-1500X-50RTP) with a vacuum atmosphere. The samples were placed together in a sandwich structure with the steel plate in between the slip-cast quartz crucible and the quartz glass, see Figure 4.4. This allowed two diffusion profiles to be measured simultaneously, one in the slip-cast crucible and one in the quartz glass. Due to furnace specifications, a processing tube of quartz was used for the lower temperature heat treatments (900-1100 °C), while a mullite tube was used for the heat treatments above 1100 °C. An alsint pipe (11 mm diameter) was placed inside the processing tube to keep the samples in place at the end of the tube and to protect the thermocouple, see Figure 4.5a and 4.5b.

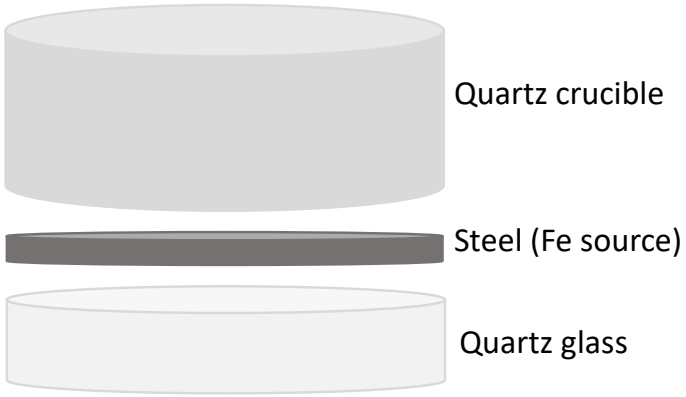

Figure 4.4: The samples were coupled in a sandwich structure with the steel layer in between the quartz crucible and the quartz glass to obtain the two diffusion profiles simultaneously.

Prior to the heat treatment, a vacuum atmosphere was created inside the sample tube using a vacuum pump. Following this, the sample tube was filled with argon before the atmosphere was pumped down to a vacuum again. This was to ensure a clean atmosphere that would not contaminate or react with the samples during the diffusion experiments. Pressures of 10^{-2}-10^{-3} mbar were maintained during the heat treatments using a vacuum pump. The temperature inside the sample tube was measured using a thermocouple (type C with a Mo layer) connected to a datalogger (Datataker DT80). After completing the heat treatment, the samples were pulled out of the oven and air cooled inside the sample tube. The experimental setup is illustrated in Figure 4.6.

(a) Slip-cast crucible, steel and quartz glass samples placed in the quartz tube on top of the alsint pipe. An extra piece of the alsint pipe was added to the top of the diffusion couples to ensure intimate contact between the faces of the samples.

(b) The samples inside the quartz processing tube.

Figure 4.5: The setup of the quartz sample tube used in the furnace.

The heat treatments were performed at different temperatures ranging from 900-1300 °C. The diffusion holding times were also varied for each temperature. The tube furnace was preheated and the samples were inserted when the desired heat treatment temperature was reached. Based on similar diffusion studies, longer holding times were chosen for the lower temperatures and shorter holding times were chosen for the higher temperatures.[30] According to the theory, the diffusion coefficient is dependent on the temperature but not the diffusion time. However, the different holding times were chosen to ensure a high enough iron concentration for the quantitative analysis and to obtain a concentration profile with a slope that is necessary to calculate the diffusion properties. An overview of the heat treatments performed is presented in Table 4.2. Each experiment was repeated twice for each temperature. The samples are named with the heat treatment temperature, duration of heat treatment and chronological sample number (e.g. 900.24.1). The notation C and Q are used to distinguish between the crucible and quartz glass samples, respectively.

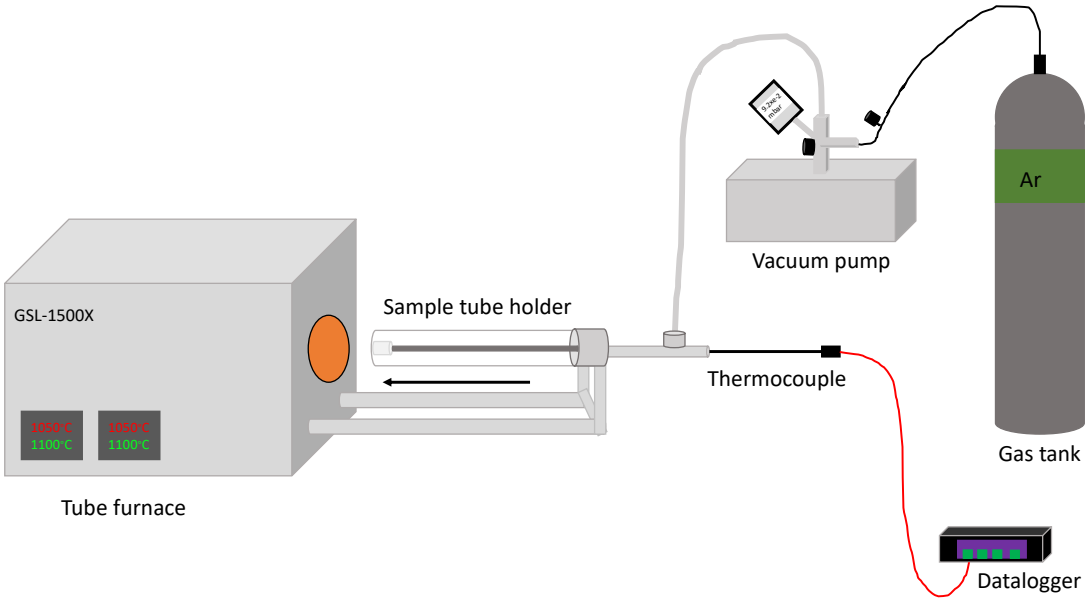

Figure 4.6: The experimental setup used in the diffusion experiments. The tube furnace (GSL-1500X-50RTP) with a sample tube holder was connected to a vacuum pump and an argon gas tank. A thermocouple connected to a datalogger (Datataker DT80) was placed inside the processing tube.

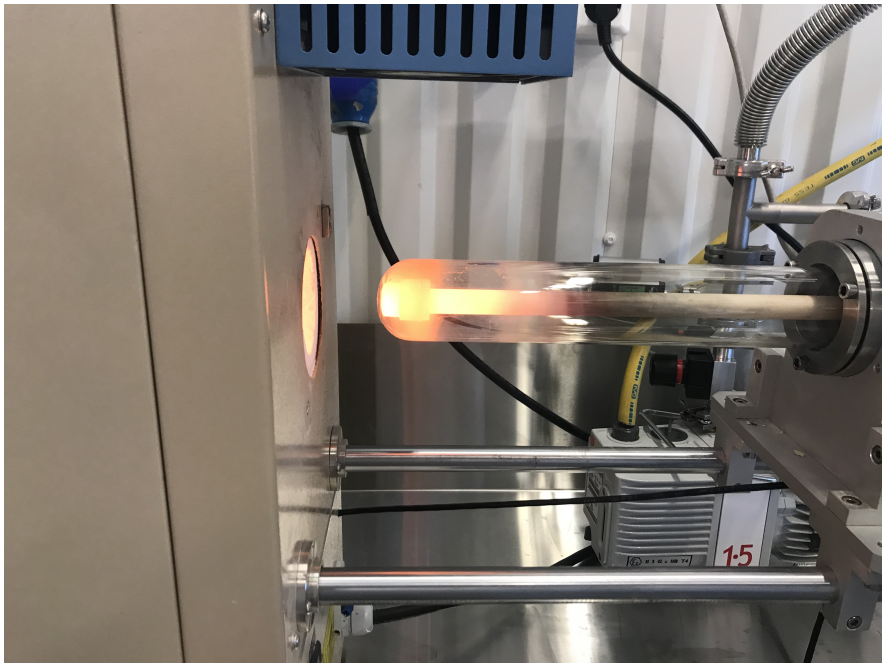

Figure 4.7: Finished heat treated samples removed from the furnace to air cool.

Table 4.2: Overview of the heat treatments performed. Temperatures, T [°C], holding times, t [hr], and sample names are given for each material. The samples are named with the heat treatment temperature, duration of heat treatment and chronological sample number. The notation C and Q are used to distinguish between the crucible and quartz glass samples, respectively.

Material	Temperature, T [°C]	Holding time, t [hr]	Sample name
Crucible	900	24	C.900.24.1
	900	24	C.900.24.2
	1000	24	C.1000.24.1
	1000	24	C.1000.24.2
	1100	26	C.1100.26.1
	1100	24	C.1100.24.2
	1200	7	C.1200.7.1
	1200	7	C.1200.7.2
	1300	3	C.1300.3.1
	1300	3	C.1300.3.2
Quartz glass	900	24	Q.900.24.1
	900	24	Q.900.24.2
	1000	24	Q.1000.24.1
	1000	24	Q.1000.24.2
	1100	26	Q.1100.26.1
	1100	24	Q.1100.24.2
	1200	7	Q.1200.7.1
	1200	7	Q.1200.7.2
	1300	3	Q.1300.3.1
	1300	3	Q.1300.3.2

4.2 GD-MS

Glow discharge mass spectrometry (GD-MS) was used to measure the iron concentration vs depth profiles present in the heat treated samples. Blank samples, that were not heat treated, of the silica crucible and quartz glass were also analysed to measure the initial iron concentrations in the two materials. An Astrum GD-MS by Nu Instruments was used, shown in Figure 4.8. The system was cryo-cooled with liquid nitrogen.

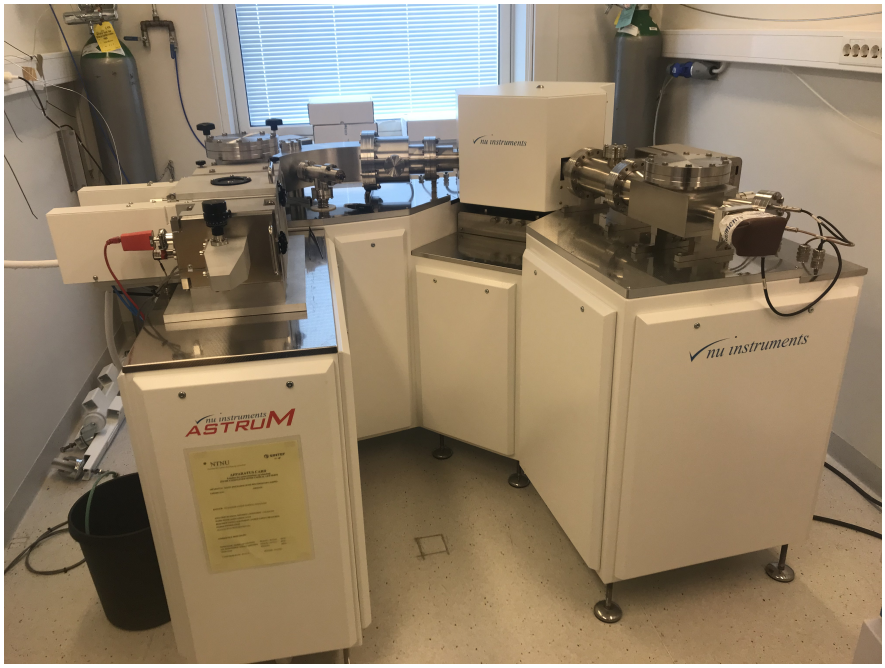

Figure 4.8: The Astrum GD-MS by Nu Instruments used to analyse the iron distribution in the heat treated samples.

GD-MS is a relatively fast and efficient analytical method for detecting impurities present in conducting and semiconducting samples in the low ppb range (1 ppba or lower). The GD-MS consists of the following main components: sample holder, plasma chamber, ion optic assembly, resolution slit, magnet, electro-static analyser and a detector.[67] The general process is illustrated in Figure 4.9. The plasma gas is typically argon. The sample is placed in the sample holder and functions as the cathode. Argon ions (Ar^+), formed in a low-pressure plasma, are accelerated towards the cathode and the sample material is sputtered.[68] This results in an emission of sputtered atoms (Sa) from the sample surface. These atoms are then accelerated in the discharge electric field where they are ionised by colliding with the argon atoms in the plasma. Several ionisation mechanisms occur, as illustrated in Figure 4.9. The ionised particles are then detected from mass spectrometry and separated according to their mass-to-charge ratio. The excited atoms are detected using atom-emission spectrometry from their light emission.[67][68][69]

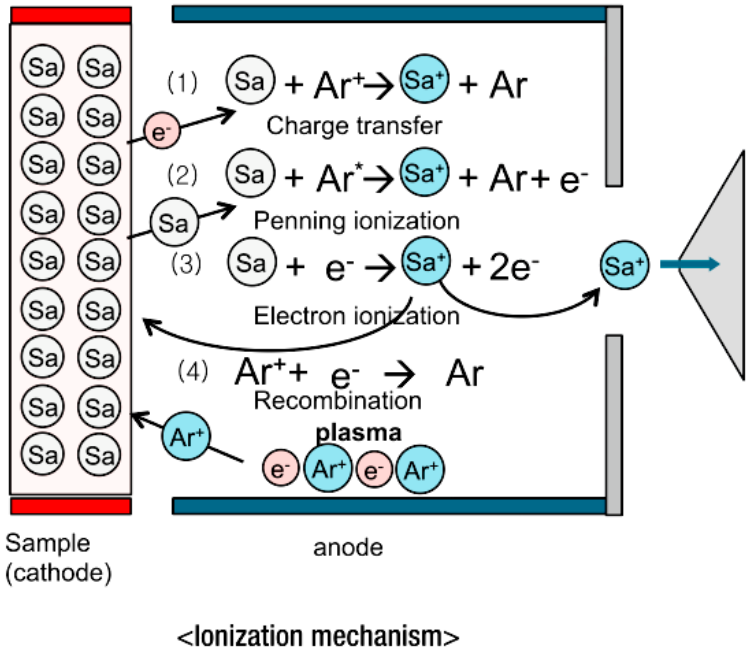

Figure 4.9: Schematic overview of the glow discharge process. The plasma chamber is in the middle with the sample to the left. The ionisation processes occurring in the chamber are shown in (1)-(4).[70]

4.2.1 Sample preparation

After completing the heat treatments the samples were polished manually with 2400 fixed abrasive. The highly contaminated surface was removed to achieve a more efficient GD-MS analysis. If the surface contamination was not removed, the GD-MS analysis would be very time consuming and the measured iron levels would be extremely high for a long time. To produce a discharge the GD-MS analysis requires a conducting sample. Since quartz is a non-conducting material, the samples were pressed into a high purity conductor. 7N purity indium pellets were pressed flat to make masks that were attached to the surfaces of the samples, see Figures 4.10, 4.11a and 4.11b. Since indium is a conductive material it will support the sputtering process so the sample can be ionised for analysis. Three small areas were cut out of the indium plate where the sample could be analysed. Before the GD-MS analysis, each indium mask was carefully etched and cleaned with nitric acid (65 % HNO_3), followed by water and ethanol, to remove any contamination and maintain its high purity.

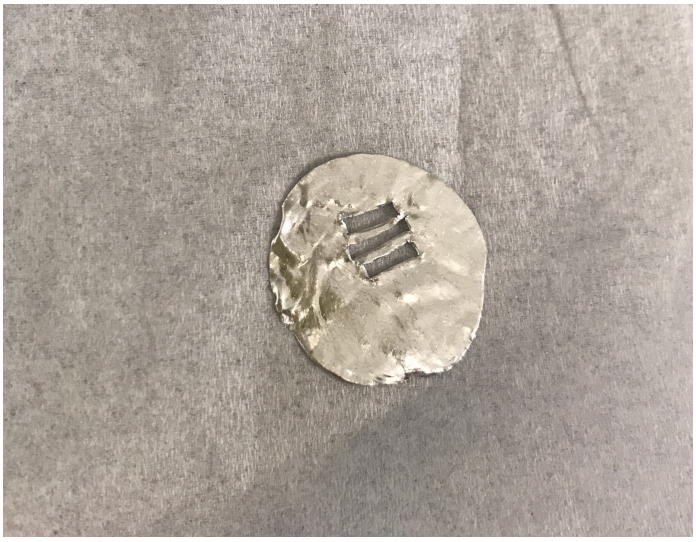

Figure 4.10: The 7N purity indium mask prepared for GD-MS analysis. Small areas are cut out so the sample can be sputtered.

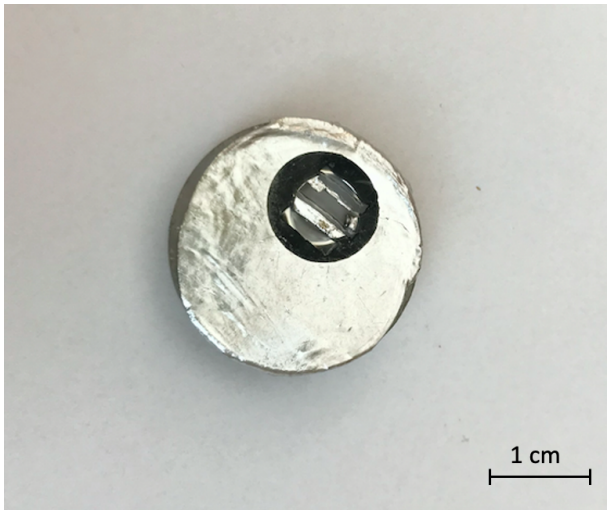

(a) A quartz glass sample with the indium mask after the GD-MS analysis.

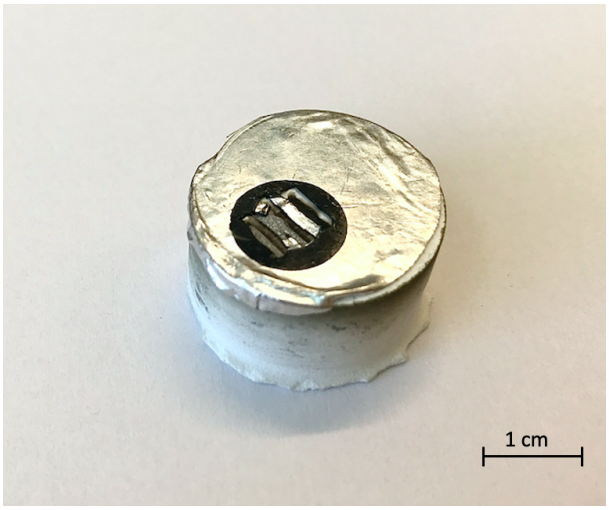

(b) A quartz crucible sample with the indium mask after the GD-MS analysis.

Figure 4.11: A 7N purity indium mask was applied to the crucible and quartz glass samples to support the sputtering process during GD-MS. The open areas on the mask are where the sample was sputtered and analysed.

Due to time limitations, concentration vs depth profiles were only obtained for eight samples. An overview of the specific samples that were analysed with GD-MS is given in Table 4.3.

Table 4.3: An overview of the samples that were analysed with GD-MS.

Material	Sample name
Silica crucible	C.900.24.2
	C.1100.26.1
	C.1200.7.1
	C.1300.3.1
Quartz glass	Q.900.24.1
	Q.1000.24.2
	Q.1200.7.1
	Q.1300.3.1

4.2.2 Quantification

The ion beam signal of the matrix, I_M, is assumed to be large relative to the individual trace elements, I_X, and is a good approximation of the total current signal (i.e. can assume a matrix concentration, K_M, of 100 %).[67] This assumption applies for trace element analysis of high-purity materials. The ion beam ratio of the element and matrix is used to quantify the elements. The concentration of an element X, K_X, is found from

$$K_X = \left(\frac{I_X}{I_M}\right) K_M \tag{4.1}$$

where I_X and I_M are the ion beam signals of the element and matrix, respectively, and K_M is the concentration of the matrix element.[71] If multiple isotopes of the matrix and the detected elements are considered, their isotope abundances should be taken into account. The concentration of an element X is then given by

$$K_X = \left(\frac{I_X}{I_M}\right) K_M \left(\frac{A_M}{A_X}\right) \tag{4.2}$$

where A_X and A_M are the isotope abundances of the element and matrix, respectively.[67] For quantitative results, relative sensitivity factors (RSF) are determined to account for the variations in the analytical sensitivity occurring between the different elements. The correct concentration of

element X, C_X, is then expressed as

$$C_X = K_X RSF_X \tag{4.3}$$

where K_X is the uncorrected element concentration (from Equation (4.2)) and RSF_X is the relative sensitivity factor of element X in the matrix.[67][71]

The elements Si, Fe and In were chosen for the analysis and Si was used as the matrix element. Since the real matrix element in the samples was SiO_2, the stoichiometric factor (0.47) was added to the results to correct for the matrix element being Si. A high signal to noise ratio is prerequisite for detecting low concentrations.[67] To achieve a low detection limit, the instrument conditions were optimised before the analysis to give a high sensitivity for the Si matrix signal. The discharge voltage (DV), discharge gas (DG) and discharge current (DV) were adjusted to maximise the intensity for the Si matrix. The GD-MS discharge parameters used for the analysis of the two silica materials are given in Table 4.4.

Table 4.4: The GD-MS discharge parameters used for the analysis of the silica samples.

Discharge current	0.3 mA
Discharge voltage	1400 V
Discharge gas	110 ml/min
RSF (Fe)	1

The results retrieved from the GD-MS analyses were adjusted in the Nu Astrum software. GD-MS spectra (intensity vs mass) from each measurement were obtained with concentration peaks for every chosen element (Si, Fe and In), shown in Figures 4.12, 4.13 and 4.14. Each peak was manually adjusted to ensure that the correct concentration was quantified. The peak for ^{56}Fe, indicated by the blue area in Figure 4.12, is very close to the peak for ^{28}Si^{28}Si (two isotope atoms of silicon). This is the peak on the right-hand side of Fe shown in Figure 4.12. ^{28}Si is the most abundant isotope of silicon and is present in both of the silica materials analysed. This results in an interference with the Fe concentration, and therefore, the correct peak has to be chosen for each measurement to avoid any mistakes in the quantification.[67]

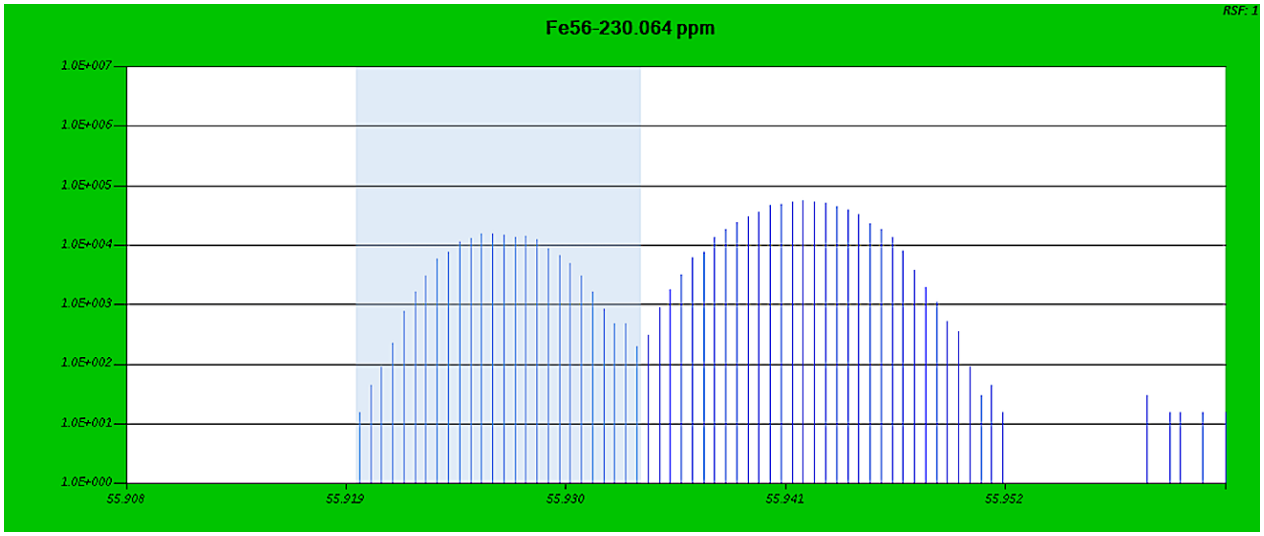

Figure 4.12: The GD-MS spectrum (intensity vs mass) for Fe. The signal peak for ^{56}Fe, indicated by the blue area, must be adjusted to the left position due to interference from ^{28}Si^{28}Si in the peak to the right.

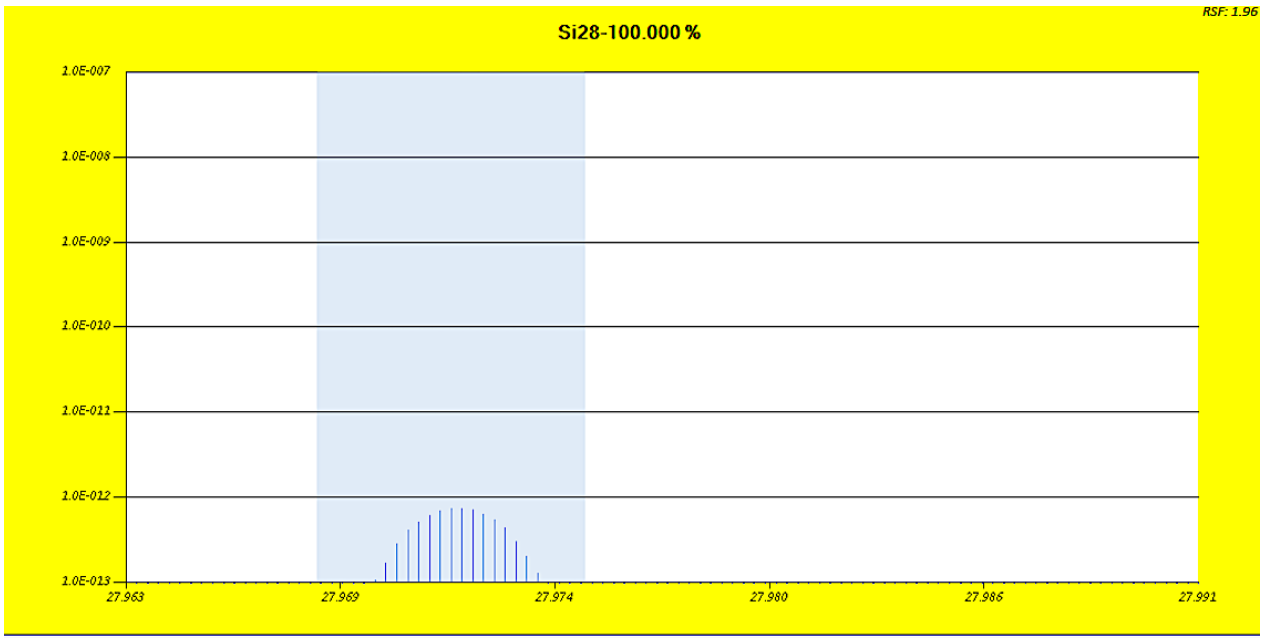

Figure 4.13: The GD-MS spectrum (intensity vs mass) for Si.

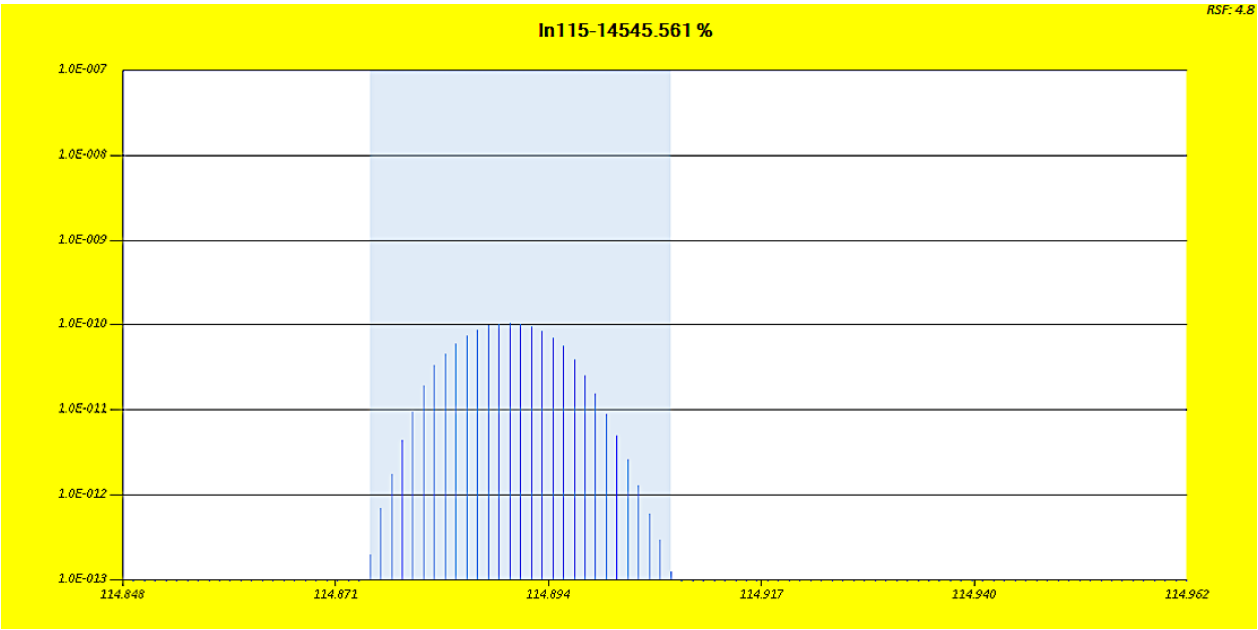

Figure 4.14: The GD-MS spectrum (intensity vs mass) for In.

4.2.3 Depth analysis

During the GD-MS analysis, the ionised Ar sputtering create craters in the sample. Layers by layers are removed from the sample surface in the sputtering process. Figure 4.15 illustrates a typical sputter crater created from a GD-MS analysis.[72]

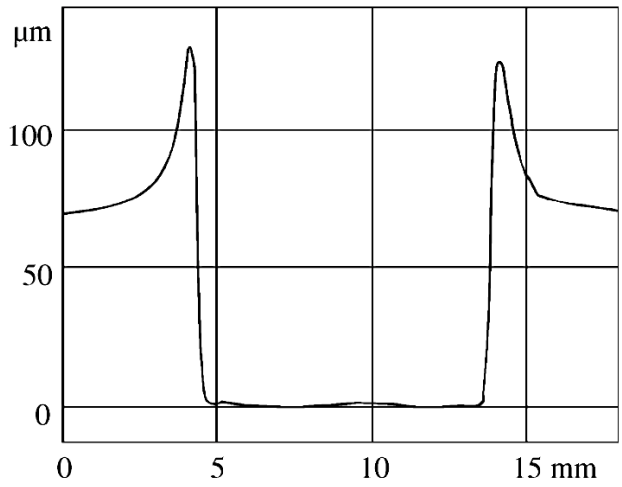

Figure 4.15: A typical sputter crater from GD-MS.[72]

The higher edges on each side of the crater in Figure 4.15 is a result of the sputtering process.

During the analysis, the sputtered material will start to deposit on the sidewalls of the crater increasing the height above the sample surface. The longer the duration of the GD-MS analysis, the deeper the crater will be. A profilometer (by Mahr) was used to measure the depth of the craters where the samples had been analysed. Profilometry is a microscopic technique used to image the surface texture of a material. A probe is passed across the crater and records each point on the surface creating a 1D or 2D map.[73] The depth profiles of samples C.1200.7.1 and Q.1300.3.1 were measured. These samples were chosen because they had longer GD-MS analysis times and would accordingly have deeper sputtering craters. The profiles were measured in the middle of the crater along its entire length. By using the measured depth and time of analysis, the sputtering rate was calculated for the two quartz materials. The sputtering rate was used to calculate the depths of the craters in all of the analysed samples which further was used to find the distances of iron diffusion in the two quartz materials.

4.3 Light microscopy

Light microscopy was used to investigate the sample surfaces before and after polishing. An inverted Axio Vert.A1 microscope from Zeiss was used, shown in Figure 4.16. No sample preparation was required. The samples were examined with light microscopy to make sure that the highly contaminated surface was removed, as well as microcracks present in the surface. The samples were polished to avoid extremely high iron levels in the GD-MS analysis. The quartz glass sample Q.1200.7.1 and crucible sample C.1200.7.1 were also cut in half to study the cross-sections of the samples after heat treatment with light microscopy.

Figure 4.16: The inverted Axio Vert.A1 microscope used to study the samples.

Chapter 5

Results

This following chapter presents the results obtained from the experiments. The approach for calculating the iron diffusion profiles is given in Appendix A.

5.1 Diffusion experiments

The densities of the slip-cast crucible and quartz glass samples were found to be 1.95 g/cm^3 and 2.2 g/cm^3, respectively, given in Table 5.1. The calculation is given in Appendix A.

Table 5.1: The calculated densities, ρ [g/cm^3], of the slip-cast silica crucible and quartz glass samples.

Material	**Density, ρ [g/cm^3]**
Silica crucible	1.95
Quartz glass	2.20

After the heat treatment, the white surface of the slip-cast crucible was grey as a result of being in contact with the steel plate. It was clear that the samples were highly contaminated. Further, there were no visible changes to the quartz glass samples apart from some shattered and cracked areas on the contact surface. Some of the shattered quartz glass was also stuck onto the steel surface. Figure 5.1 shows the crucible, quartz glass and steel samples post heat treatment at 900 °C. Images of all of the heat treated samples can be found in Appendix B. Figure 5.2 presents the temperature profile measured inside the sample tube during the heat treatment at 900 °C. The temperature was even and stayed constant for the whole duration of the experiment. After diffusion at 900 °C it took approximately one hour before the samples cooled down to room temperature.

Figure 5.1: Samples C.900.24.1, Q.900.24.1 and the steel plate after heat treatment.

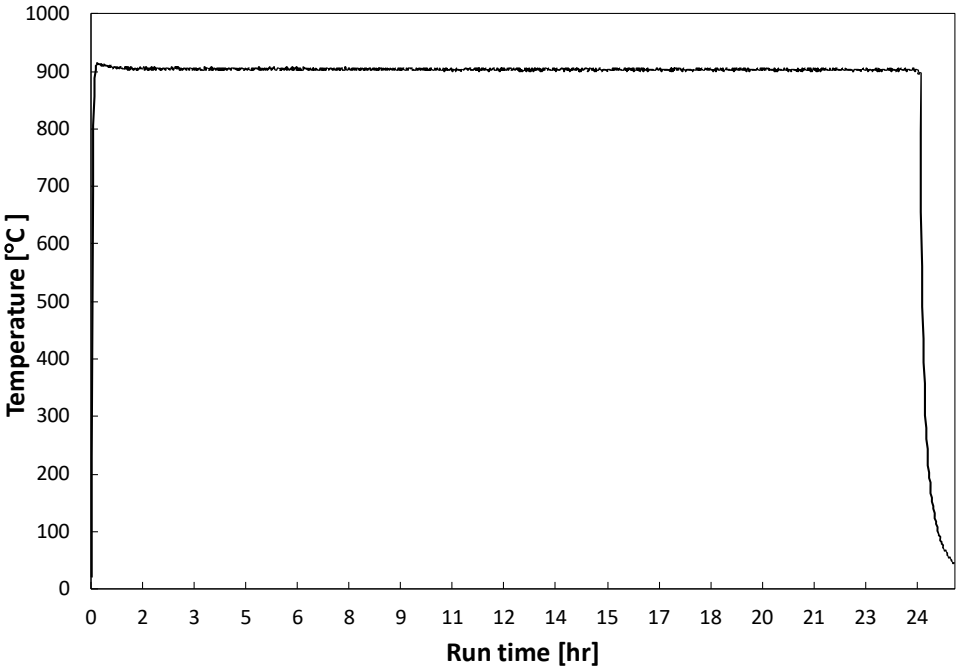

Figure 5.2: The temperature profile measured inside the sample tube during heat treatment at 900 °C for 24 hours.

Only one diffusion experiment at 1300 °C was performed successfully. The mullite tube cracked shortly after entering the furnace during the second attempt. However, this was not realised until after the heat treatment was completed. An increase in pressure to 2 mbar was observed as the

sample tube was placed inside the furnace. This increase in pressure was subsequently identified as the mullite tube cracking. However, due to the vacuum pump, the tube kept together during the experiment, but the finished heat treated samples where ruined. The steel plate in between the quartz crucible and quartz glass seemed to have melted and was stuck onto both sample surfaces, see Figure 5.3. The quartz glass sample was brown, as well as the top part of the crucible sample.

Figure 5.3: The samples after the second attempt at heat treating at 1300 °C for 3 hours. The slip-cast silica crucible is to the left and the quartz glass is to the right. The steel plate is melted and stuck onto both sample surfaces.

5.2 GD-MS

The diffusion profiles of iron in the silica crucible and quartz glass were calculated using the concentration vs depth profiles obtained at different temperatures ranging from 900-1300 °C. A summary of the Arrhenius diffusion relations calculated for the two quartz materials is given in Table 5.5. The results are compared to the literature in Figure 5.29. The approach for calculating the iron diffusion profile is described in Appendix A. It should be noted that since the samples were polished prior to the GD-MS analysis, the given depths in the concentration vs depth profiles do not correspond to the exact positions in the sample, but illustrates the distances of the iron diffusion.

5.2.1 Analysis of blank samples

The iron distributions measured in the blank samples of the silica crucible and quartz glass are given in Figures 5.4a and 5.4b.

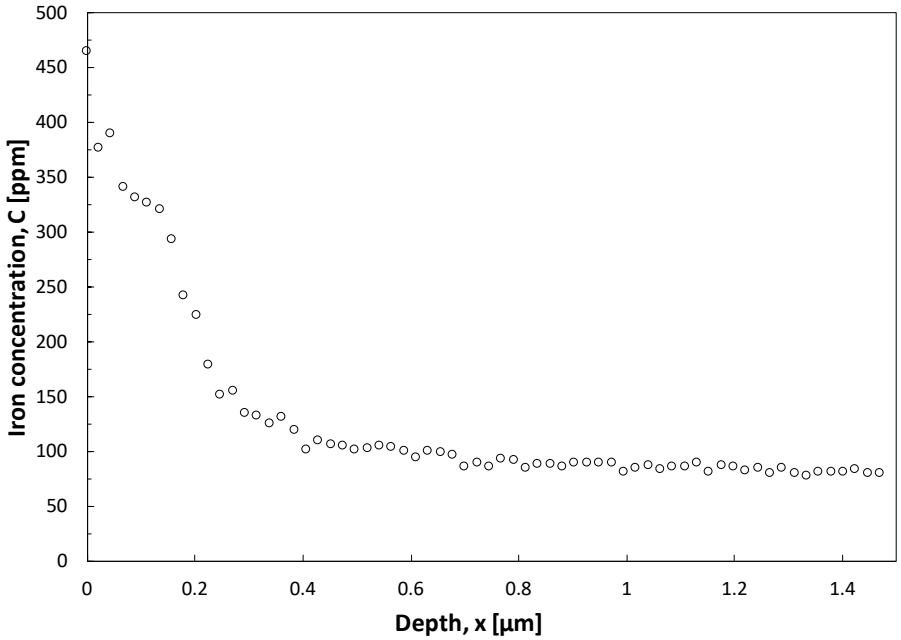

(a) The iron distribution in a blank Vesuvius standard grade silica crucible.

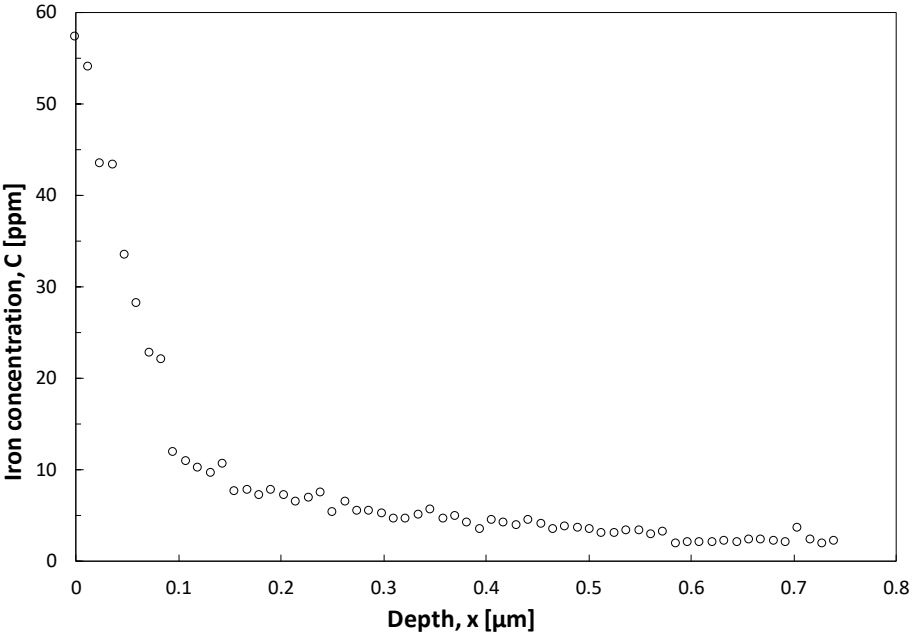

(b) The iron distribution in a blank synthetic quartz glass sample.

Figure 5.4: The iron distributions measured in blank samples of the silica crucible and quartz glass.

The initial iron concentrations were found to be 82.8 ppm in the silica crucible and 2.2 ppm in the quartz glass, see Table 5.2. Both GD-MS analyses started at high iron levels in the sample surface before decreasing rapidly and stabilising deeper into the sample. When the iron concentration was

no longer decreasing it was assumed that the initial iron concentration in the bulk material was reached.

Table 5.2: The initial iron concentrations measured in the silica crucible and quartz glass samples.

Material	Fe concentration [ppm]
Silica crucible	82.8
Quartz glass	2.2

5.2.2 Slip-cast crucible

Concentration vs depth profiles for 900, 1100, 1200 and 1300 °C obtained from the GD-MS analyses are given in Figures 5.5, 5.8, 5.10 and 5.12. The concentration profiles are fitted to the one-dimensional solution to Fick's law of diffusion, Equation (2.7), in Figures 5.7, 5.9, 5.11 and 5.13. The outliers in the plots were neglected in the calculations. The calculated diffusion coefficients for the different temperatures are given in Table 5.3 and Figure 5.14. The Arrhenius diffusion relation, Equation (2.10), is calculated in Figure 5.15 through linear regression. See Appendix A for calculations.

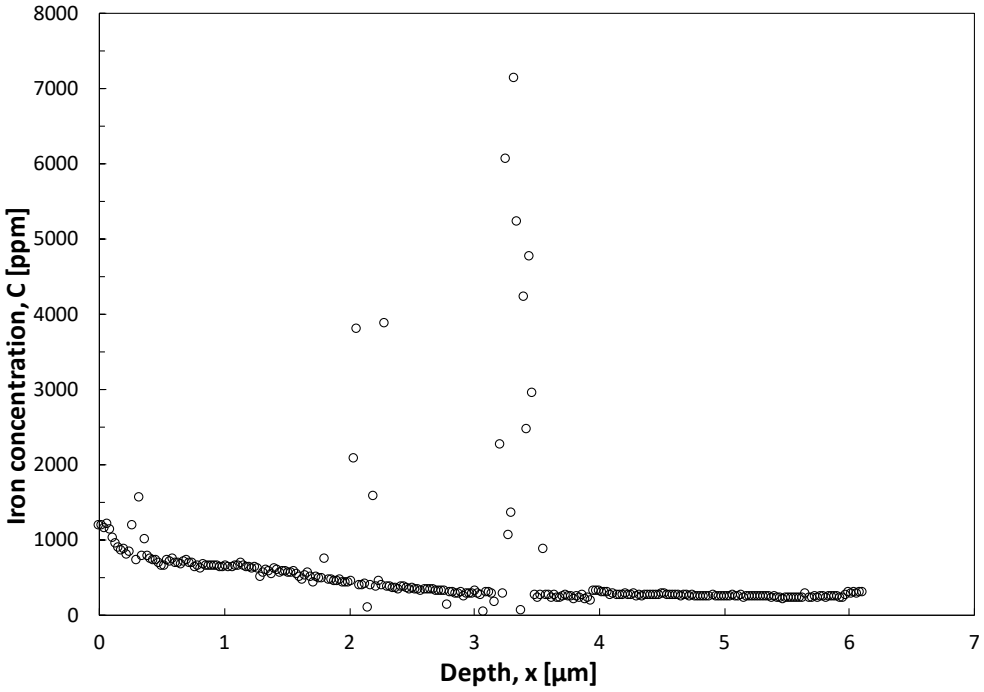

Figure 5.5: The iron distribution in sample C.900.24.2 measured from the GD-MS analysis.

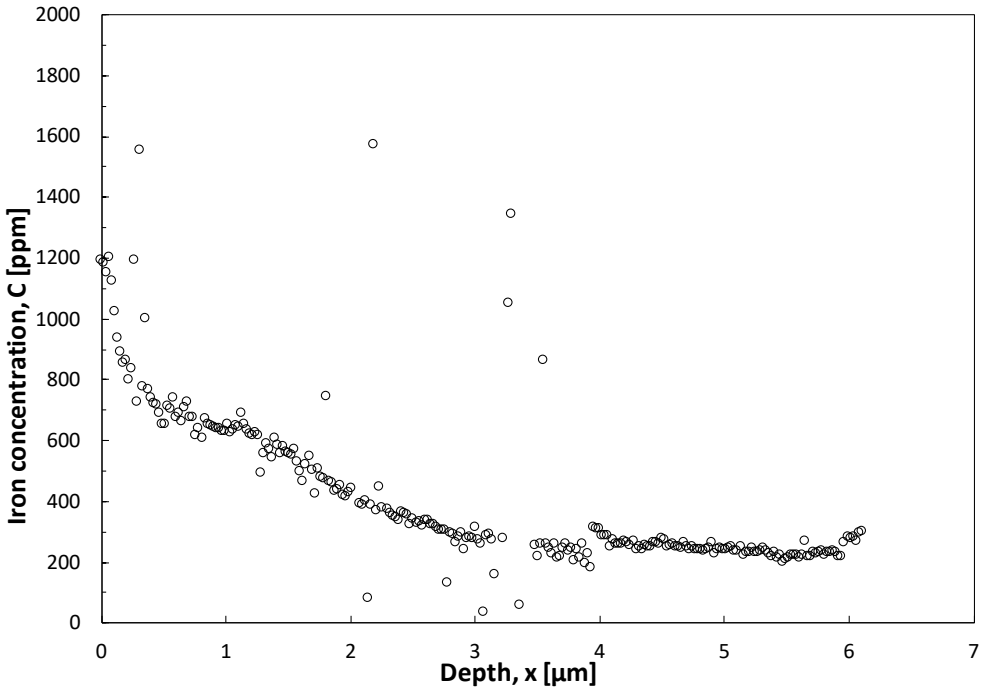

Figure 5.6: The iron distribution in sample C.900.24.2 measured from the GD-MS analysis, excluding the outliers in Figure 5.5.

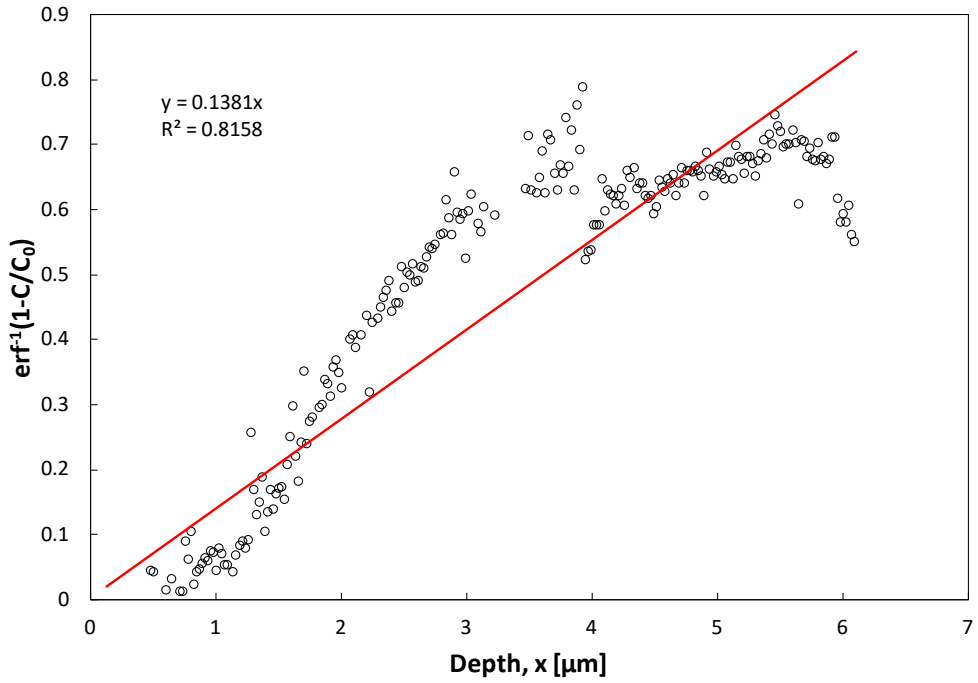

Figure 5.7: The concentration profile of C.900.24.2 fitted to the solution of Fick's law, Equation (2.7).

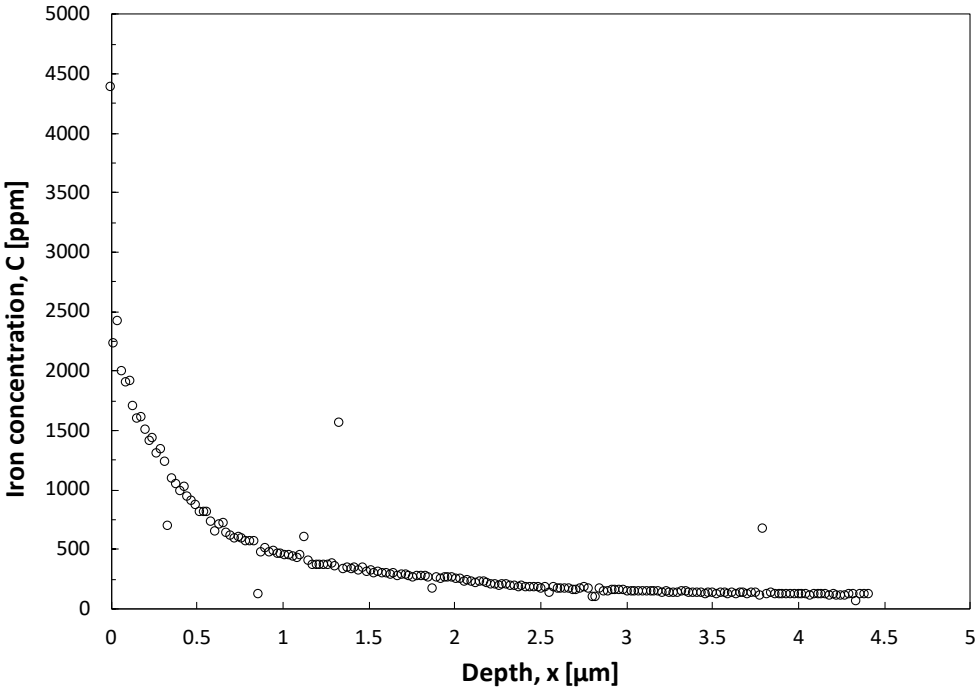

Figure 5.8: The iron distribution in sample C.1100.26.1 measured from the GD-MS analysis.

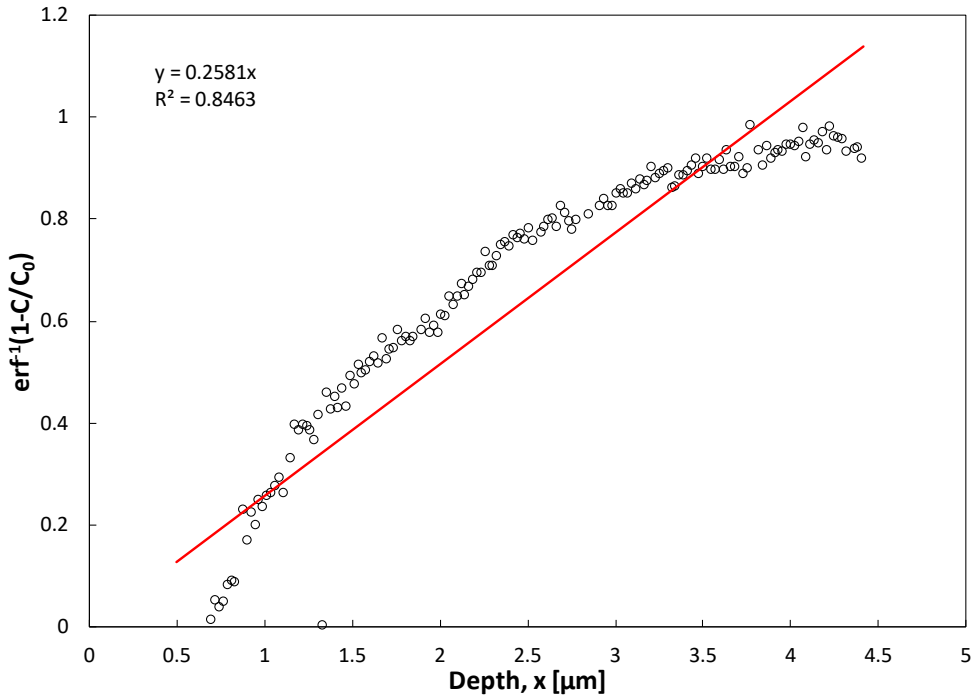

Figure 5.9: The concentration profile of C.1100.26.1 fitted to the solution of Fick's law, Equation (2.7).

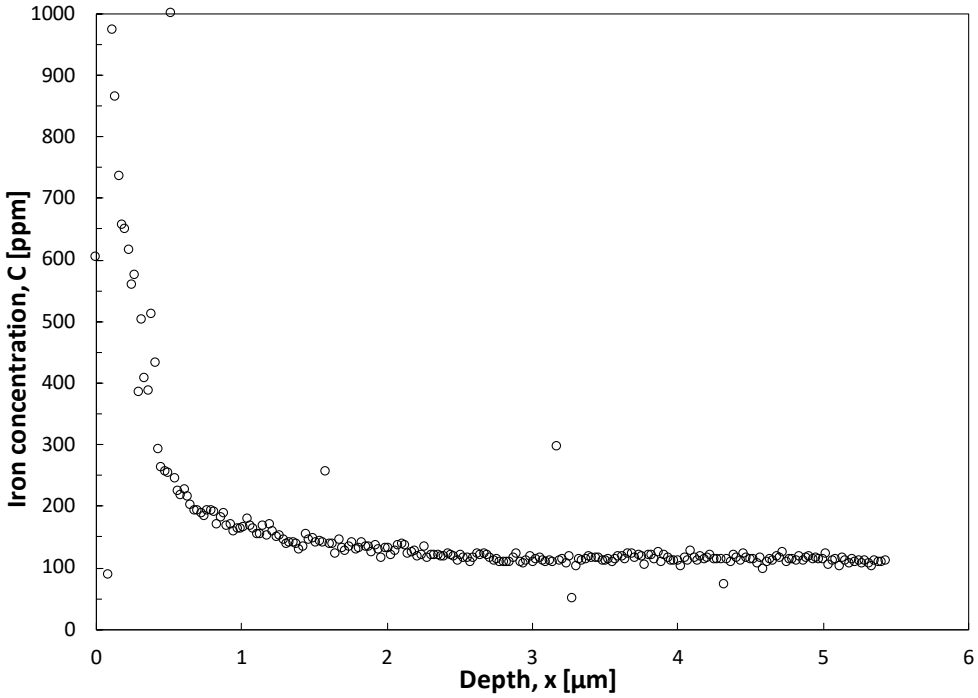

Figure 5.10: The iron distribution in sample C.1200.7.1 measured from the GD-MS analysis.

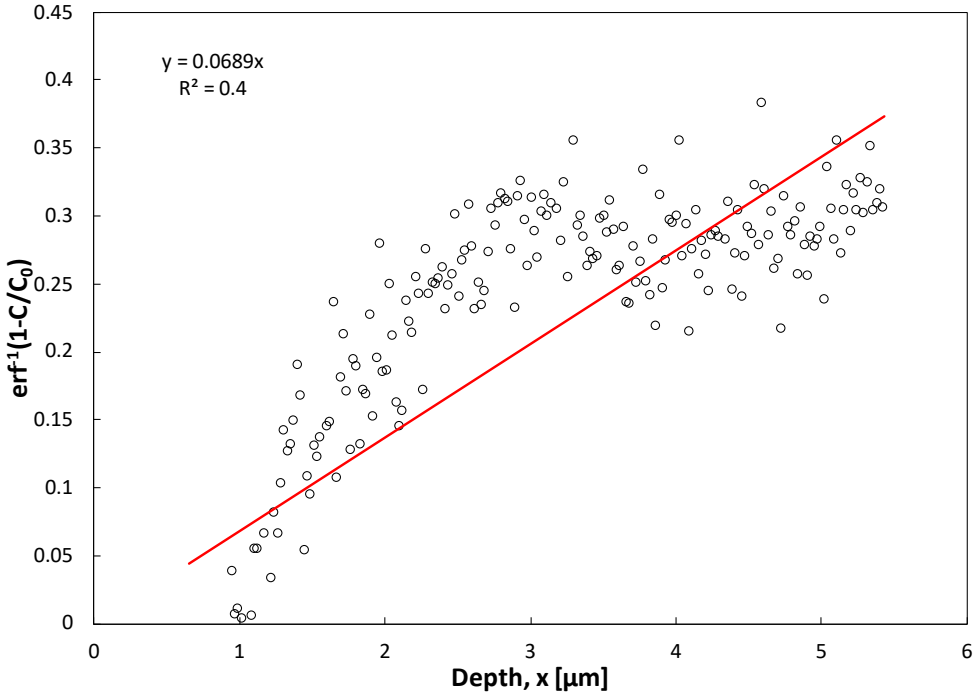

Figure 5.11: The concentration profile of C.1200.7.1 fitted to the solution of Fick's law, Equation (2.7).

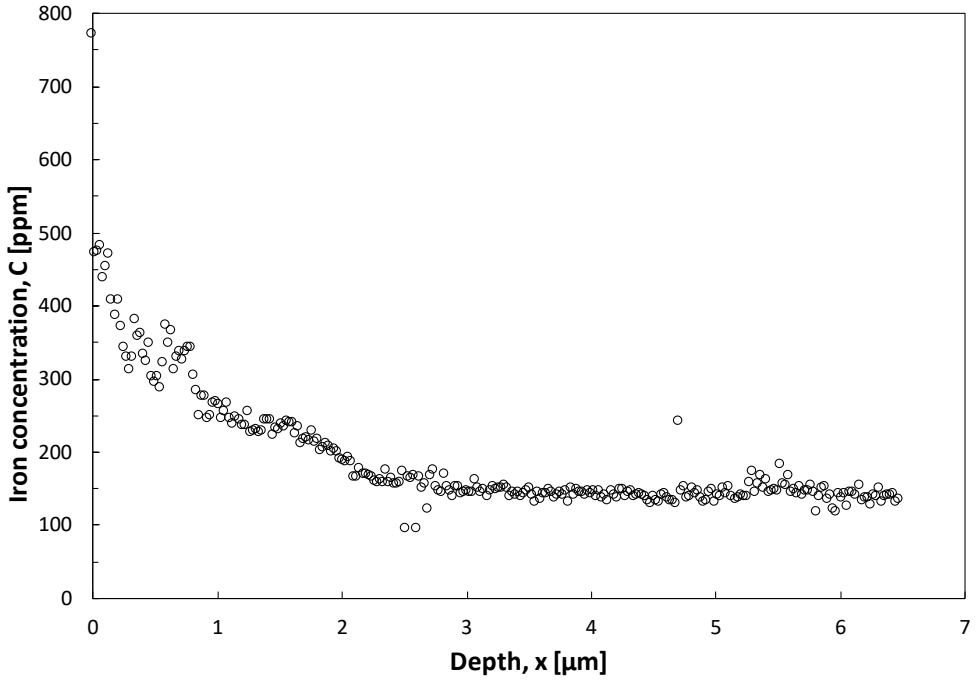

Figure 5.12: The iron distribution in sample C.1300.3.1 measured from the GD-MS analysis.

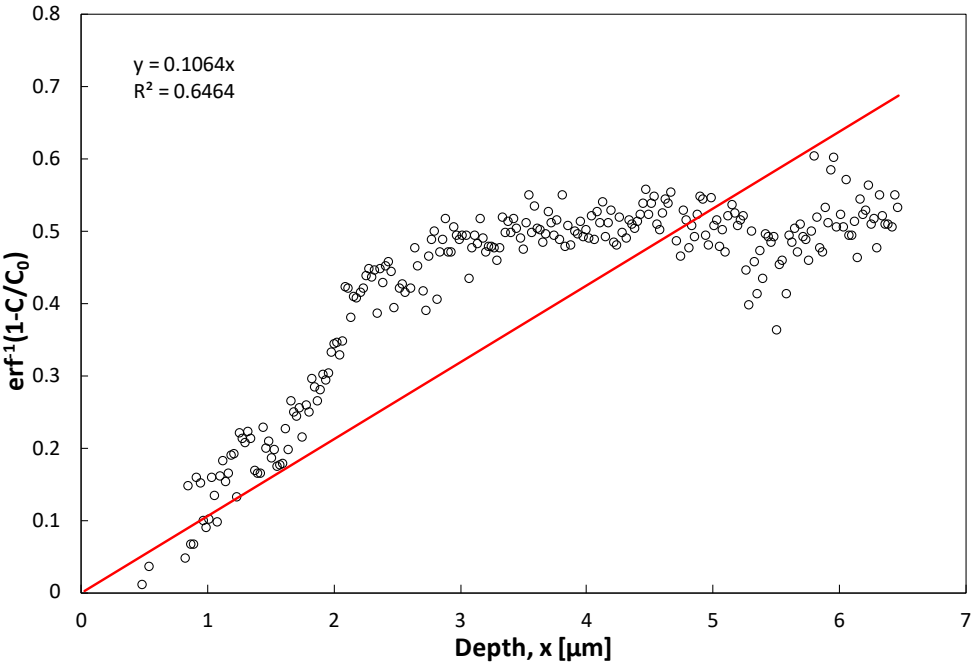

Figure 5.13: The concentration profile of C.1300.3.1 fitted to the solution of Fick's law, Equation (2.7).

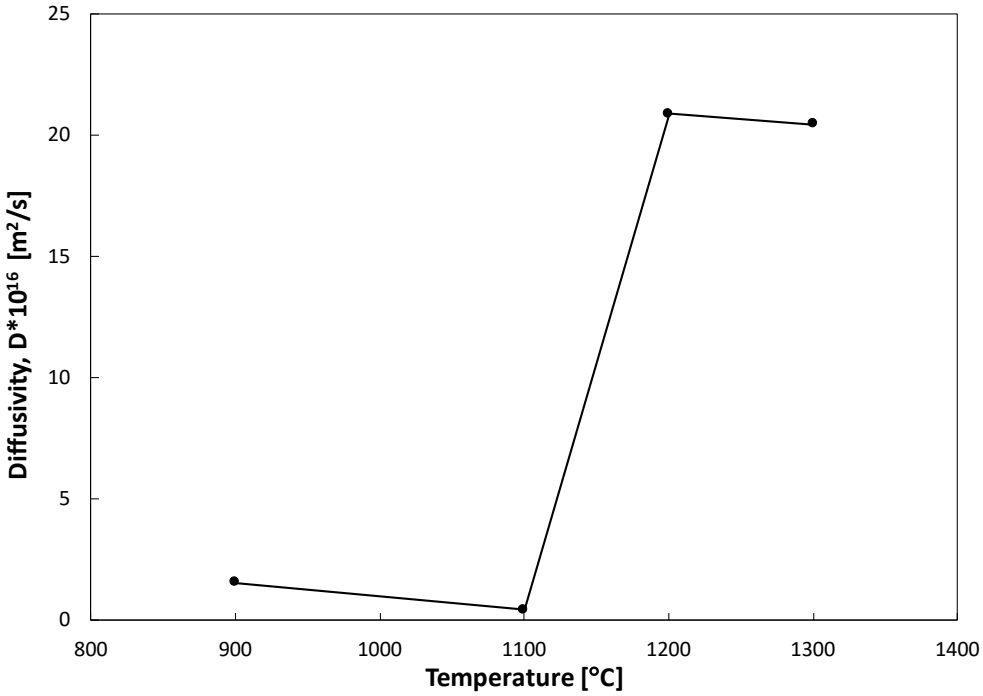

Figure 5.14: The diffusion coefficients measured for different temperatures in the silica crucible.

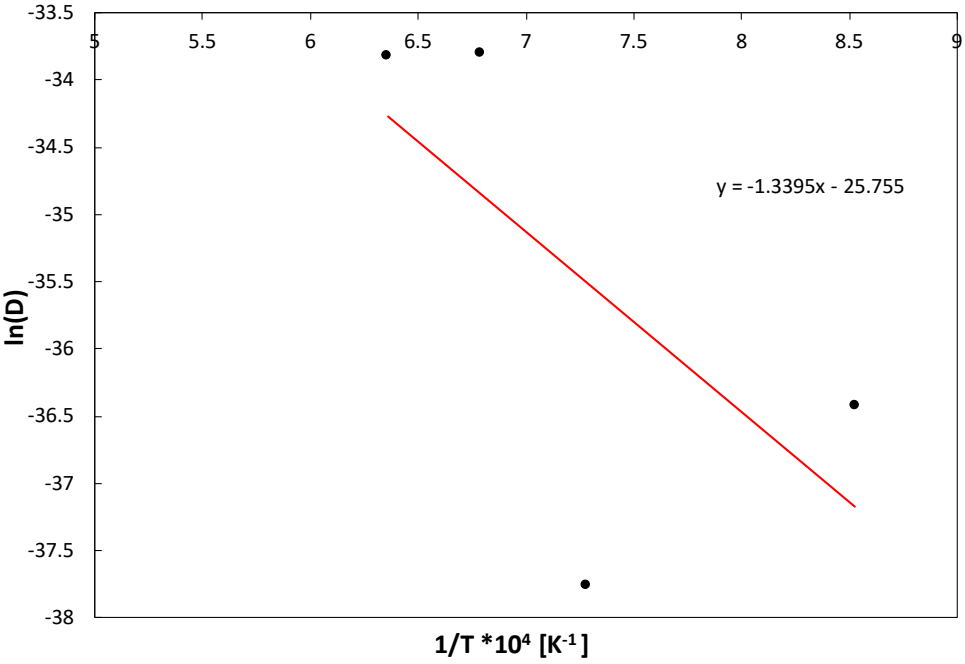

Figure 5.15: The Arrhenius plot for the silica crucible. The red line represents the linear regression.

Table 5.3: The diffusion coefficients, D [m^2/s], and boundary concentrations, C_0 [ppm], measured in the crucible samples.

Sample name	T [°C]	t [hr]	D [m^2/s]	C_0 [ppm]
C.900.24.2	900	24	1.52x10^{-16}	683
C.1100.26.1	1100	26	4.01x10^{-17}	620
C.1200.7.1	1200	7	2.09x10^{-15}	164.2
C.1300.3.1	1300	3	2.05x10^{-15}	299

The diffusion profile for iron in the slip-cast crucible was found to be

$$D = 6.53 \cdot 10^{-8} exp\left(\frac{-1.154 \text{ eV}}{kT}\right) \text{ cm}^2\text{/s}.$$

5.2.3 Quartz glass

Concentration vs depth profiles for 900, 1200 and 1300 °C obtained from the GD-MS analyses are given in Figures 5.16, 5.23 and 5.25. The concentration profiles are fitted to the one-dimensional solution to Fick's law of diffusion, Equation (2.7), in Figures 5.17, 5.24 and 5.26. The outliers in the plots were neglected in the calculations. The calculated diffusion coefficients for the different temperatures are given in Table 5.4 and Figure 5.27. The Arrhenius diffusion relation, Equation (2.10), is calculated in Figure 5.28 through linear regression. See Appendix A for calculations.

It should be noted that the GD-MS analysis of sample Q.900.24.1, shown in Figure 5.16, was analysed in two parts with a time gap in between. To check if the second curve was a better fit to the diffusion equation the first part of the measurement was excluded, shown in Figure 5.18. By comparing the correlation factors, R^2, from the linear regressions in Figures 5.17 and 5.18 it was found that including both parts of the measurement gave the best fit, with an R^2 of 0.77 compared to 0.65. After the two first GD-MS analyses of Q.900.24.1, the sample was re-polished to examine the iron distribution further into the quartz material. The results are shown in Figures 5.19 and 5.20. The measured iron concentrations were significantly higher after polishing.

The diffusion coefficient for Q.1000.24.2 was not calculated due to inadequate concentration vs depth profiles, seen from Figures 5.21 and 5.22. In Figure 5.21 the measured iron concentrations were very high indicating a lot of surface contamination. Therefore, the sample was re-polished and a second GD-MS analysis was performed. The results, shown in Figure 5.22, were quite scattered and the iron concentrations were not stabilising.

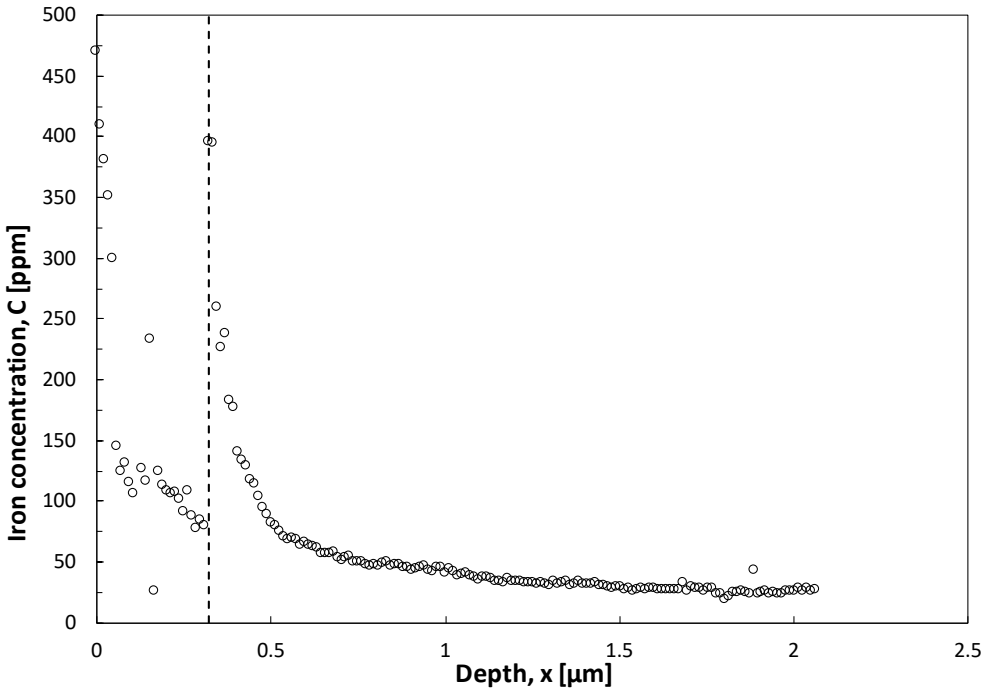

Figure 5.16: The iron distribution in sample Q.900.24.1 measured from the GD-MS analysis. The measurement was done in two parts with a time gap in between, separated by the dotted line.

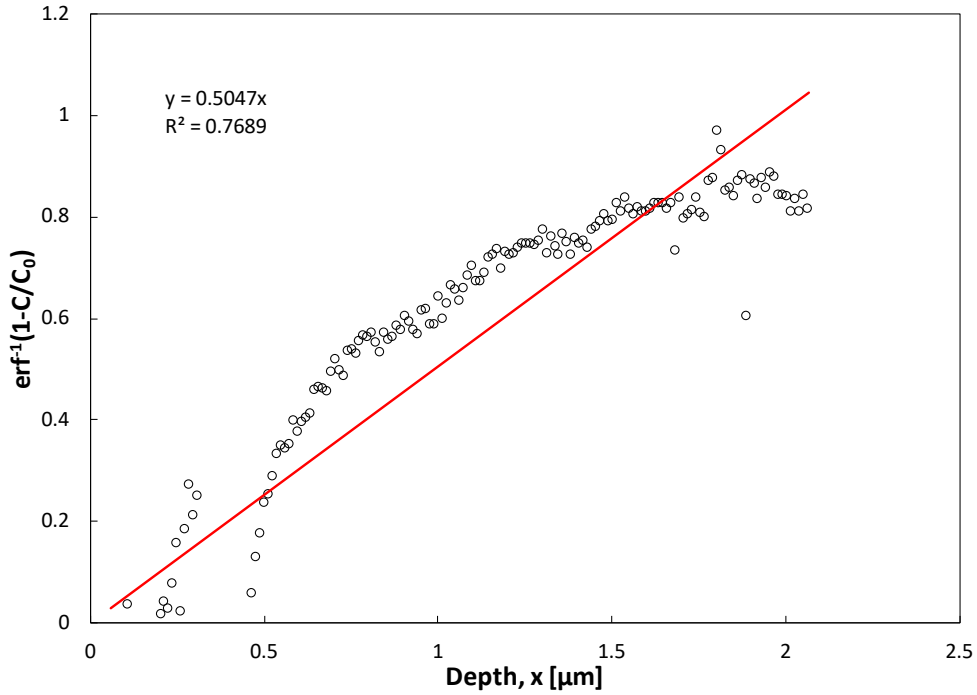

Figure 5.17: The concentration profile of Q.900.24.1 fitted to the solution of Fick's law, Equation (2.7).

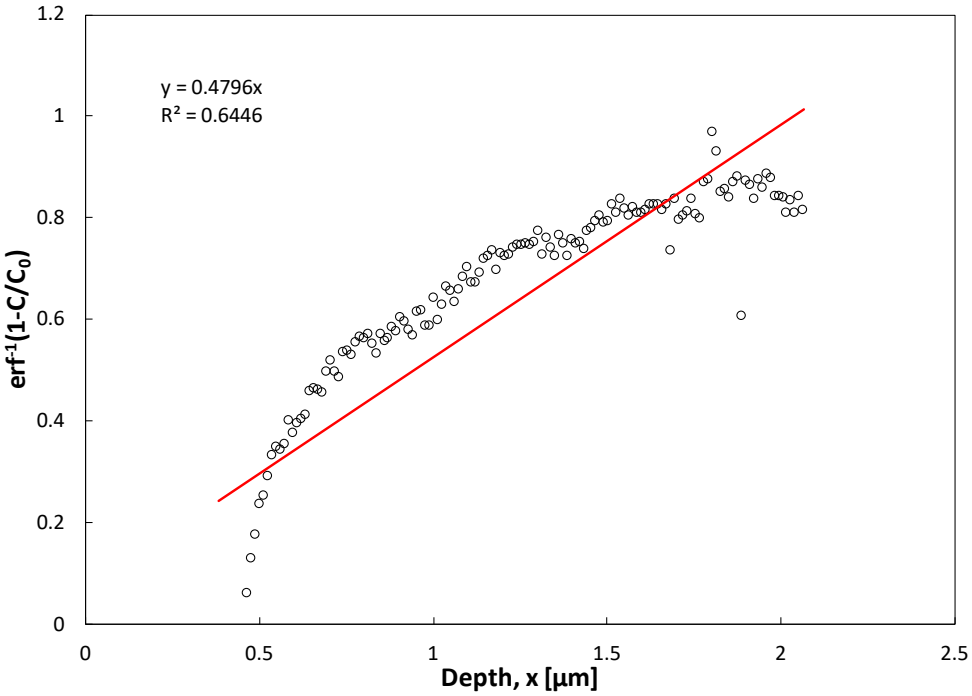

Figure 5.18: The concentration profile of Q.900.24.1 fitted to the solution of Fick's law, Equation (2.7), using only the second part of the measurement.

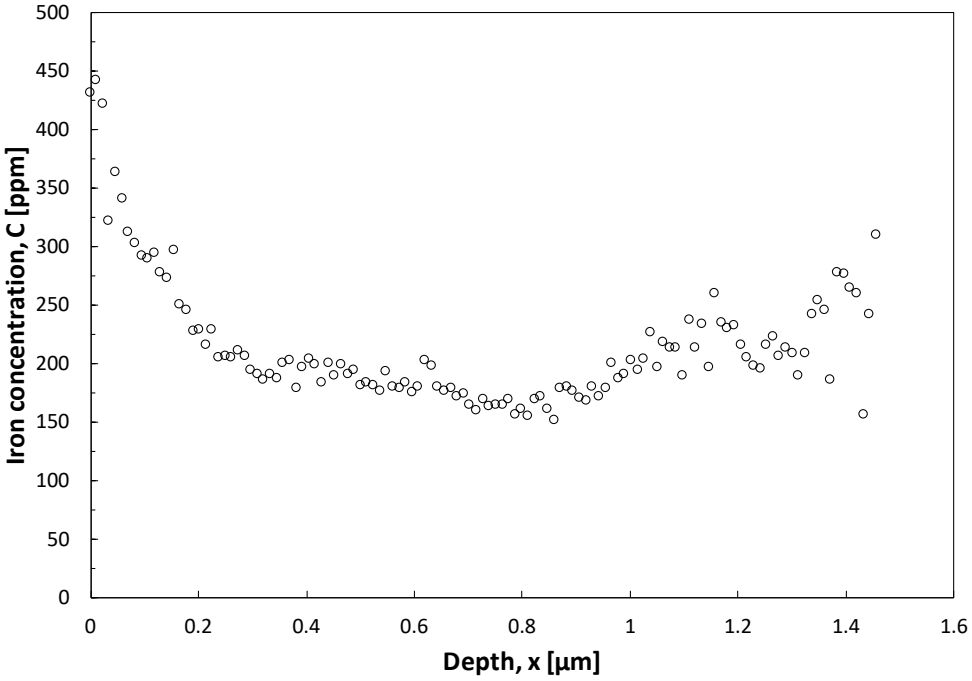

Figure 5.19: The iron distribution in Q.900.24.1, after re-polishing, measured from the GD-MS analysis.

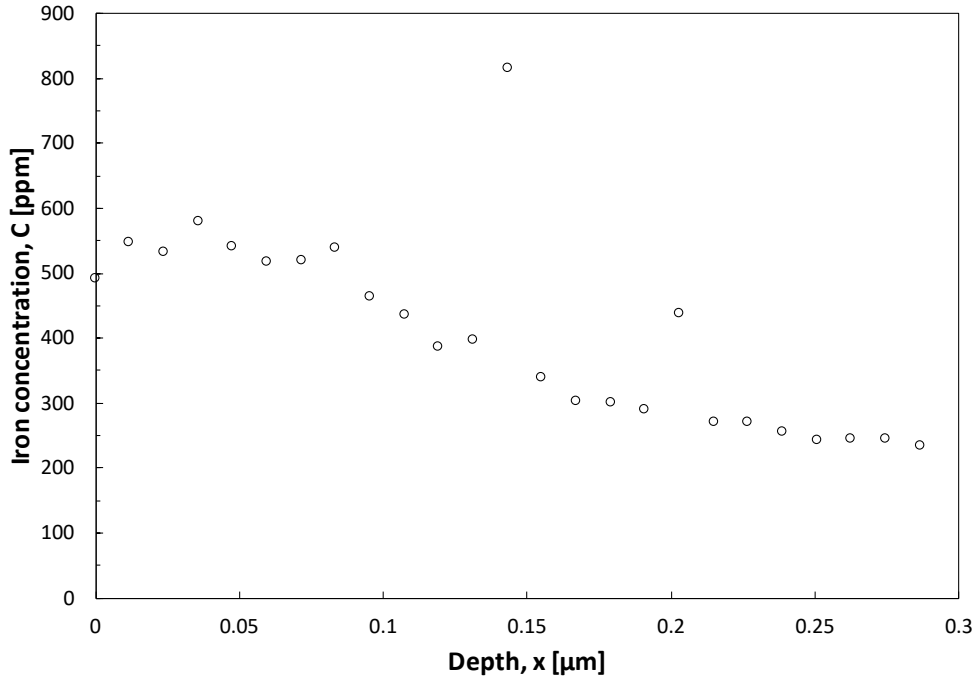

Figure 5.20: The iron distribution in Q.900.24.1, after re-polishing the second time, measured from the GD-MS analysis.

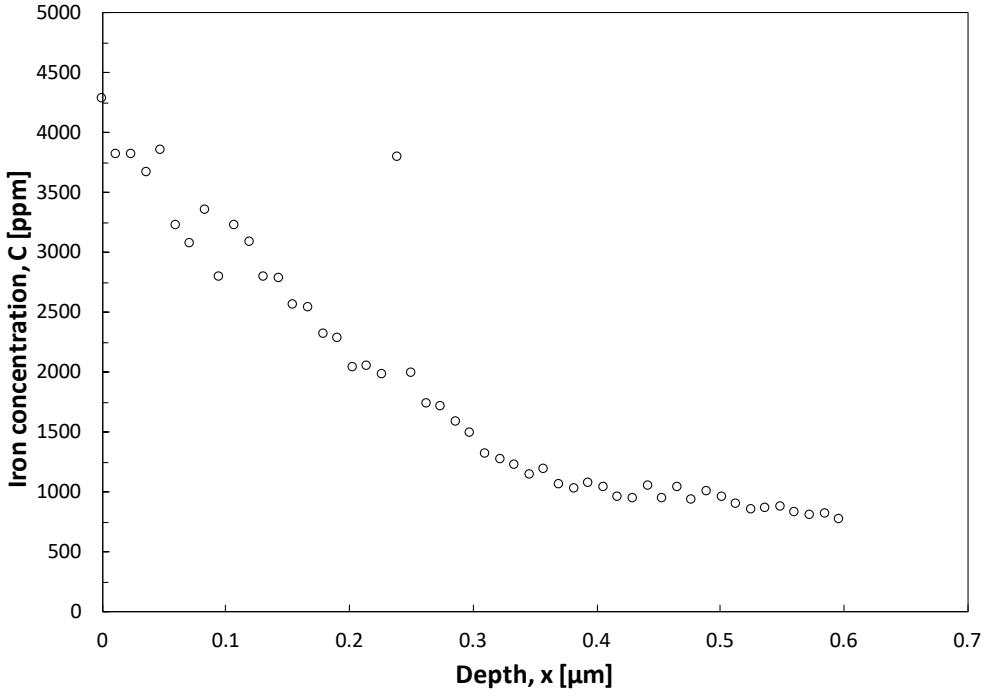

Figure 5.21: The iron distribution in sample Q.1000.24.2 measured from the GD-MS analysis.

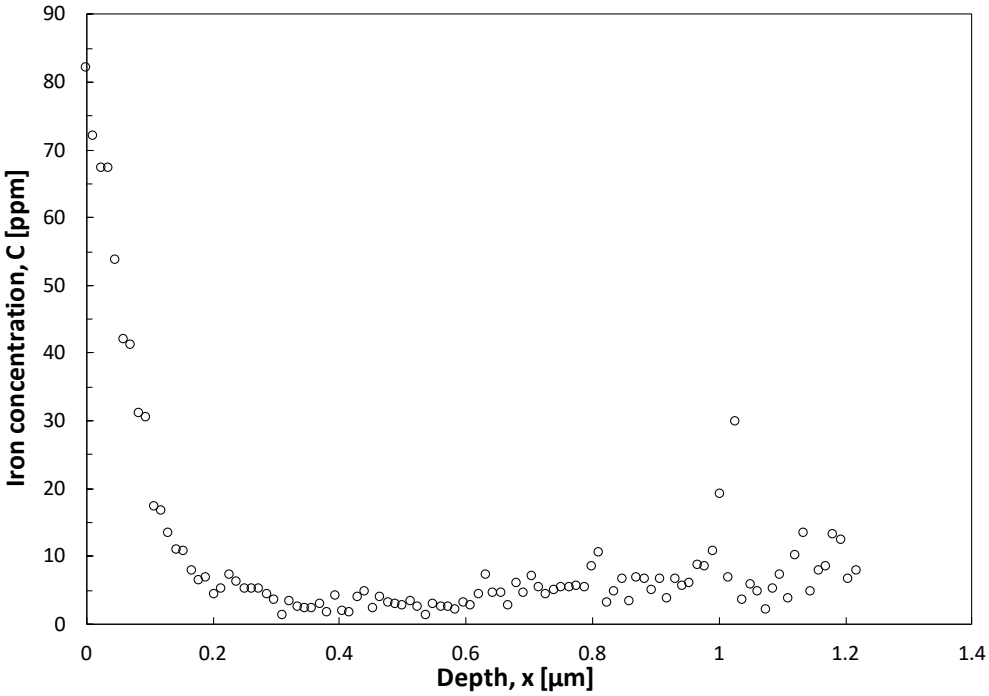

Figure 5.22: The iron distribution in sample Q.1000.24.2, after re-polishing, measured from the GD-MS analysis.

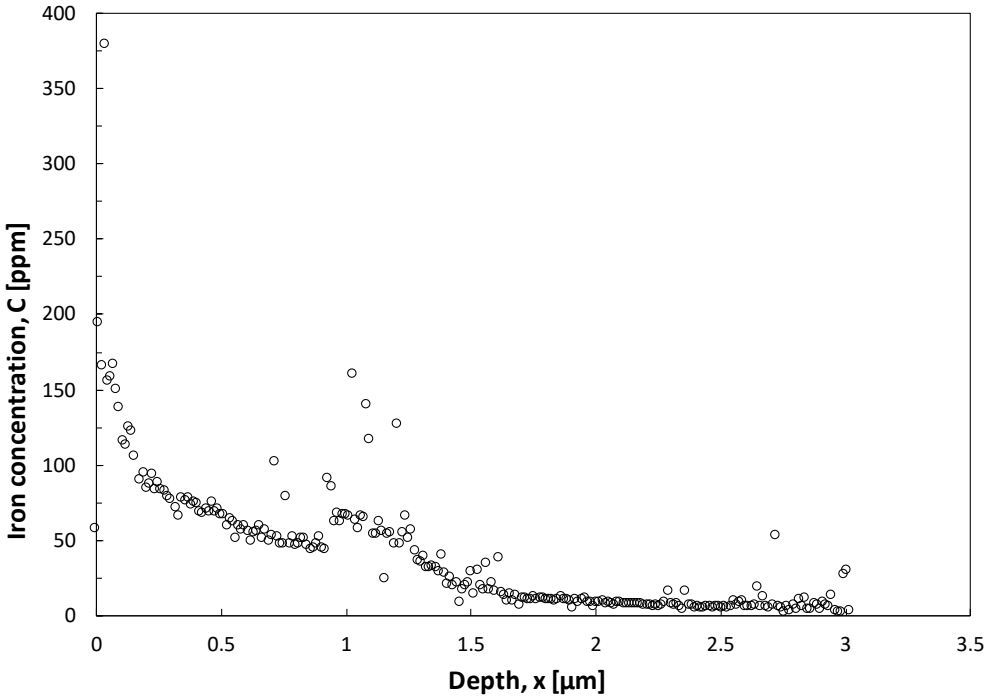

Figure 5.23: The iron distribution in sample Q.1200.7.1 measured from the GD-MS analysis.

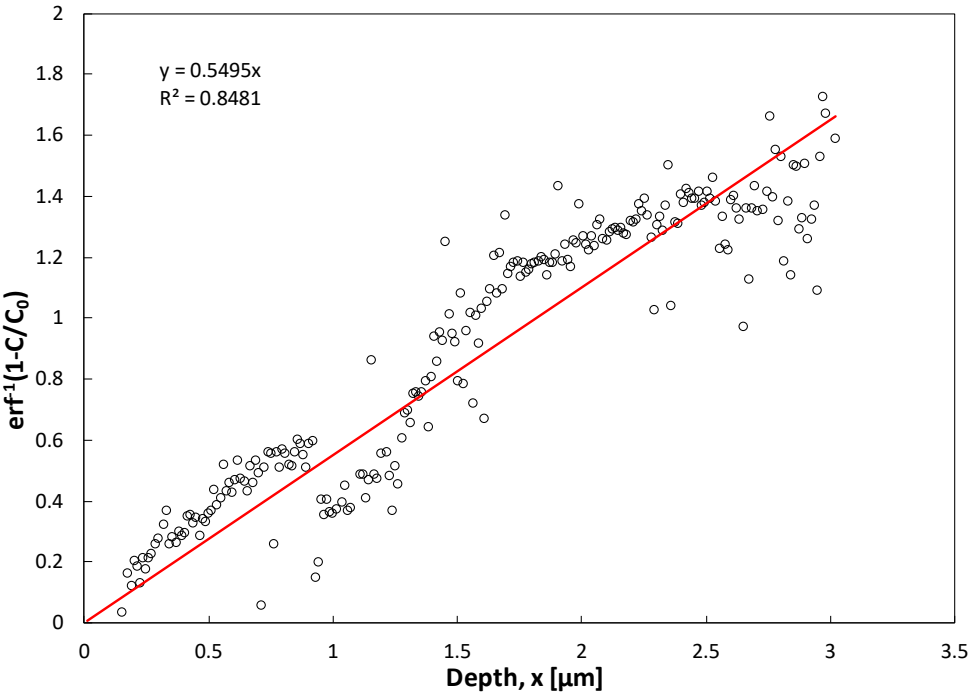

Figure 5.24: The concentration profile of Q.1200.7.1 fitted to the solution of Fick's law, Equation (2.7).

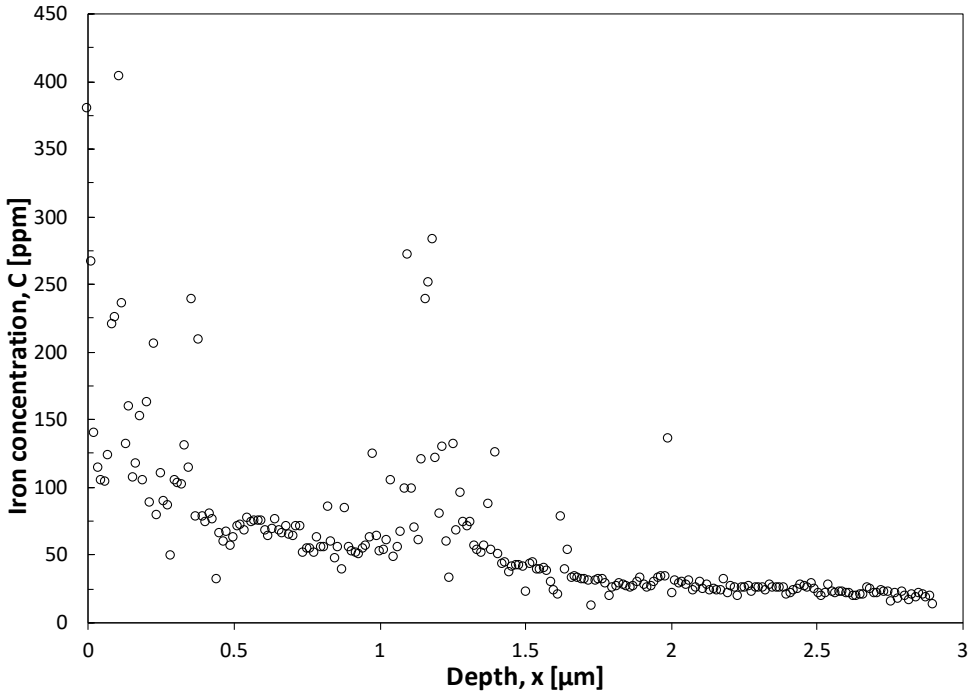

Figure 5.25: The iron distribution in sample Q.1300.3.1 measured from the GD-MS analysis.

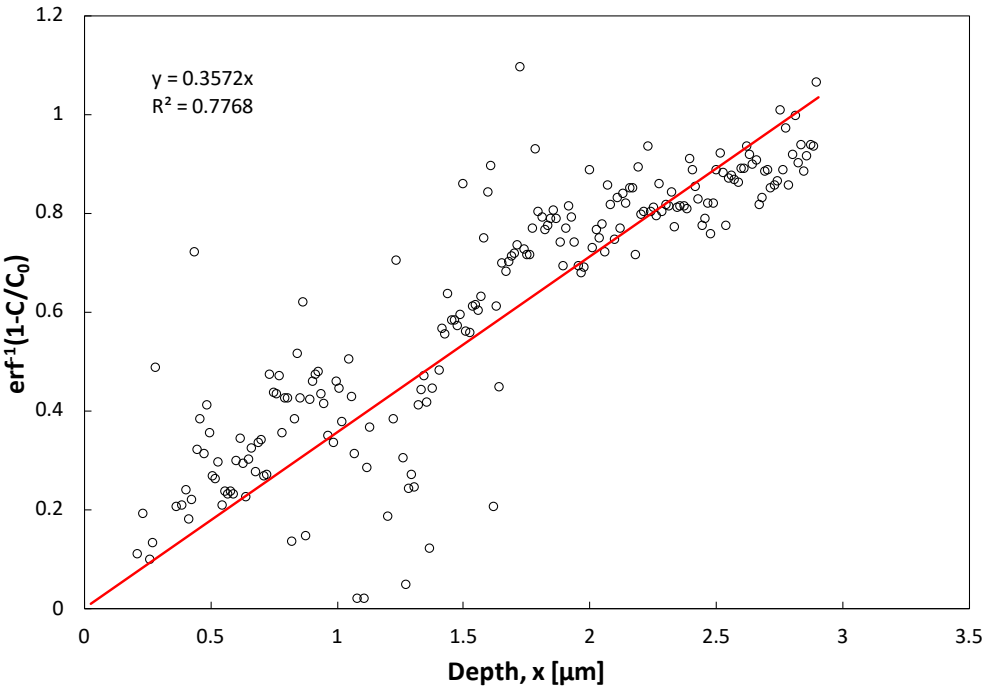

Figure 5.26: The concentration profile of Q.1300.3.1 fitted to the solution of Fick's law, Equation (2.7).

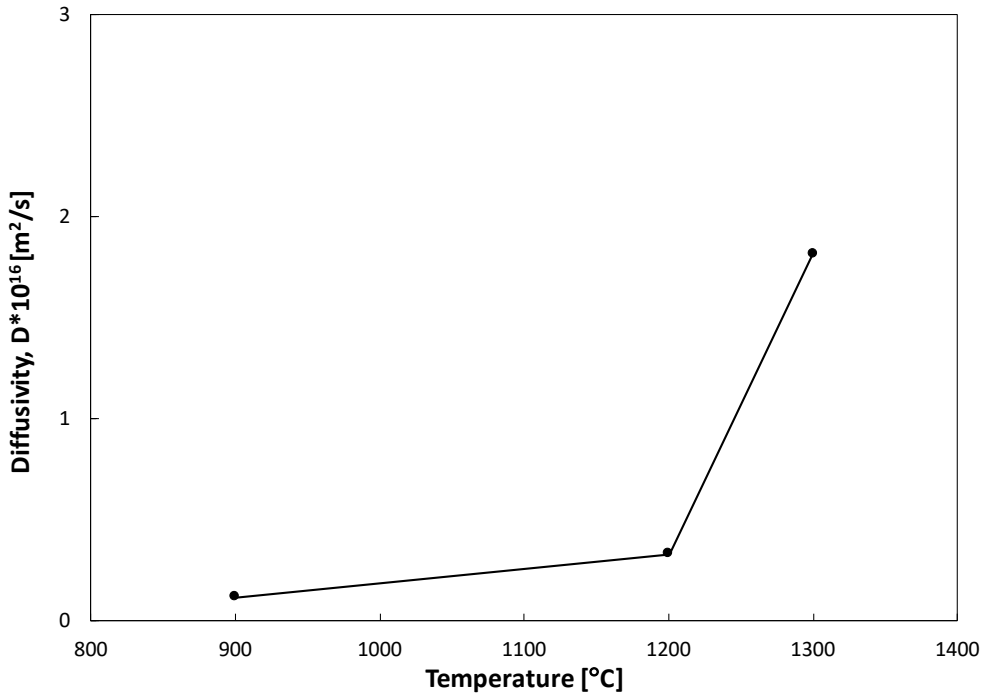

Figure 5.27: The diffusion coefficients measured for different temperatures in the quartz glass.

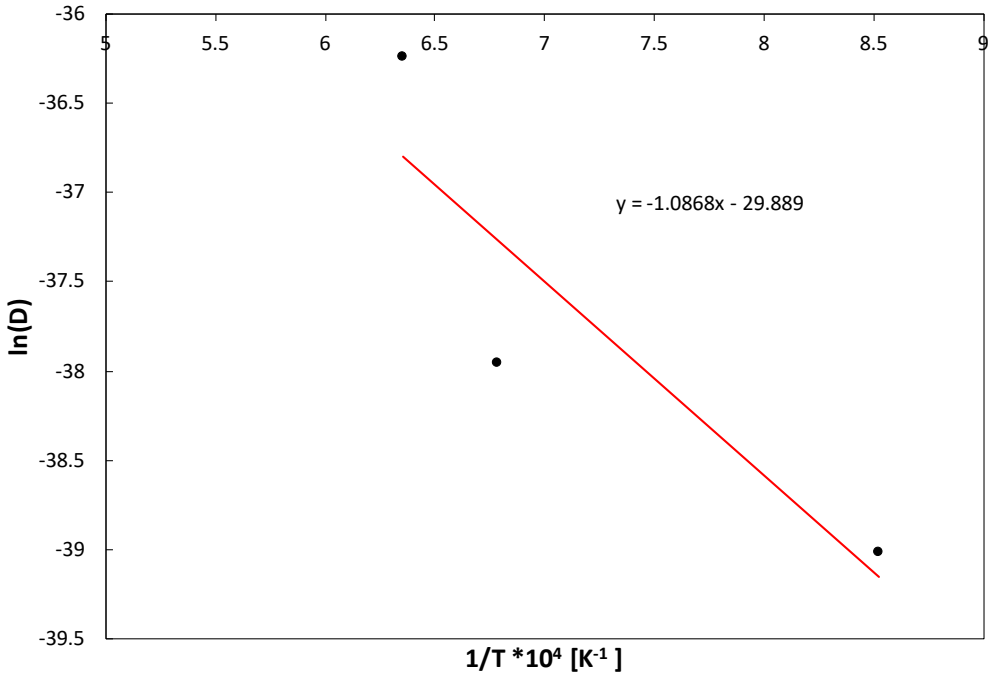

Figure 5.28: The Arrhenius plot for the quartz glass. The red line represents the linear regression.

Table 5.4: The diffusion coefficients, D [m^2/s], and boundary concentrations, C_0 [ppm], measured in the quartz glass samples.

Sample name	**T [°C]**	**t [hr]**	**D [m^2/s]**	**C_0 [ppm]**
Q.900.24.1	900	24	1.14x10^{-17}	110.9
Q.1200.7.1	1200	7	3.23x10^{-17}	109
Q.1300.3.1	1300	3	1.82x10^{-16}	100.5

The diffusion profile for the quartz glass was found to be

$$D = 1.05 \cdot 10^{-9} exp\left(\frac{-0.937 \text{ eV}}{kT}\right) \text{ cm}^2/\text{s}.$$

The Arrhenius diffusion relations calculated for the two quartz materials are given in Table 5.5. Table 5.6 presents the calculated diffusion coefficients at different temperatures using the calculated Arrhenius relations. Figure 5.29 compares the diffusion profiles of iron from this work with values from the literature. The authors are given in the legend. Apart from Schubert et al. and Skarstad who also measured the iron diffusion in a slip-cast silica crucible, the reported diffusion values for

iron are measured in quartz glass.

Table 5.5: The calculated Arrhenius relations for the silica crucible and quartz glass. The temperature-dependent preexponential, D_0 [cm^2/s], and the activation energy, E_a [eV], is given for both materials.

Material	D_0 [cm^2/s]	E_a [eV]
Silica crucible	6.53x10^{-8}	1.154
Quartz glass	1.05x10^{-9}	0.937

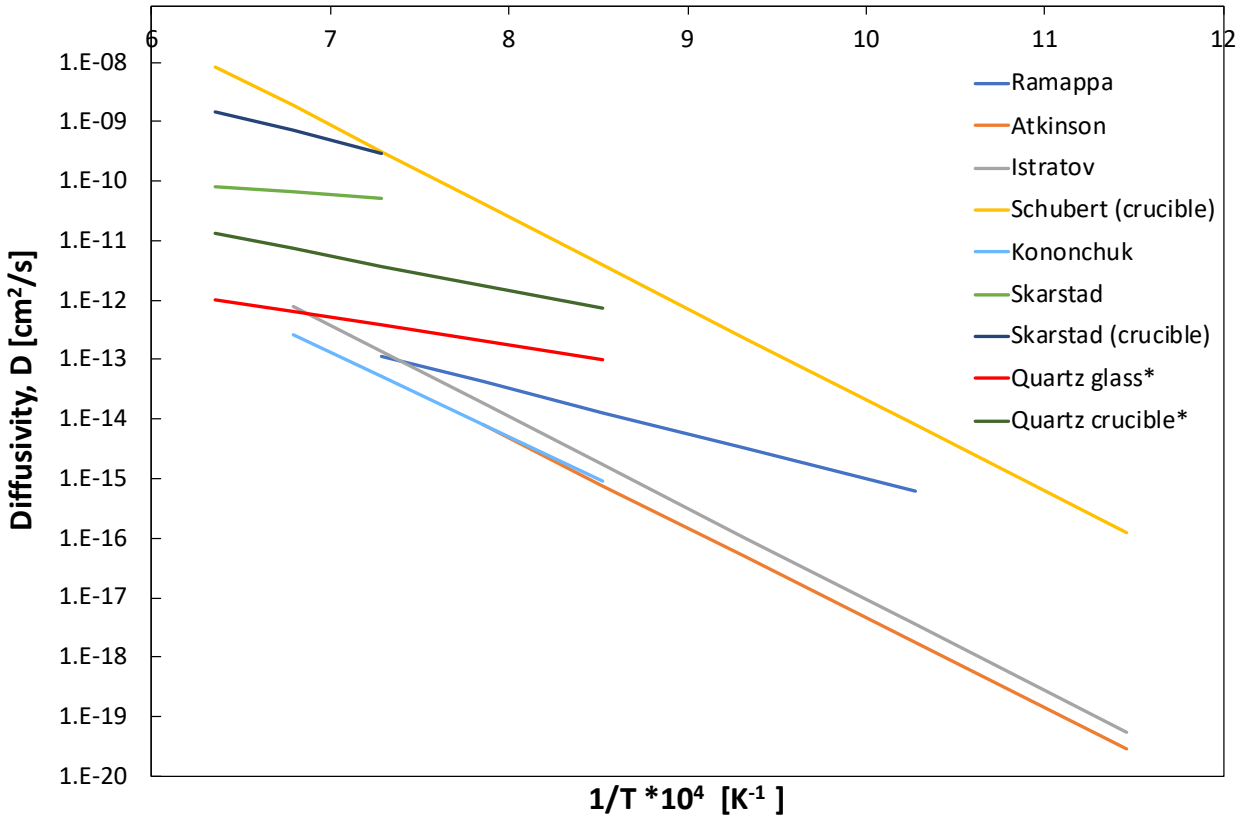

Figure 5.29: A comparison of the calculated diffusion coefficients for iron in the slip-cast crucible and quartz glass to values found in the literature. Apart from Schubert et al. and Skarstad, the diffusion profiles of iron were measured in quartz glass.*This work

Table 5.6: The calculated diffusion coefficients, D [cm^2/s], at different temperatures using the calculated Arrhenius relations from Table 5.5.

Temperature, T [°C]	**Diffusion coefficient, D [cm^2/s]**	
	Silica crucible	**Quartz glass**
900	7.17x10^{-13}	9.90x10^{-14}
1100	3.78x10^{-12}	3.82x10^{-13}
1200	7.34x10^{-12}	6.53x10^{-13}
1300	1.31x10^{-11}	1.04x10^{-12}

5.2.4 Depth analysis

The depth profiles of the GD-MS craters in samples C.1200.7.1 and Q.1300.3.1 are presented in Figures 5.30 and 5.31. The sputtering rates for the silica crucible and quartz glass were measured to be 0.57 nm/s and 0.30 nm/s, respectively, given in Table 5.7. Due to unevenness in the crater measurements, the averages of the plotted depths for each material were used in the calculation of the sputtering rates. The calculation can be found in Appendix A.

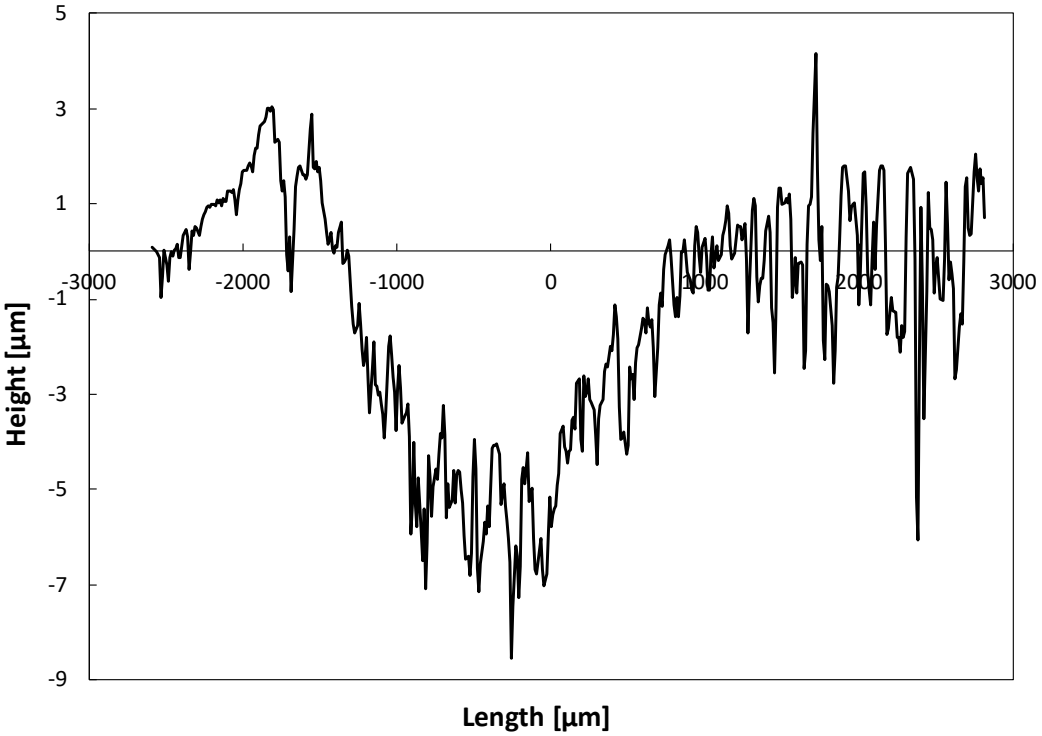

Figure 5.30: The GD-MS crater depth profile of C.1200.7.1.

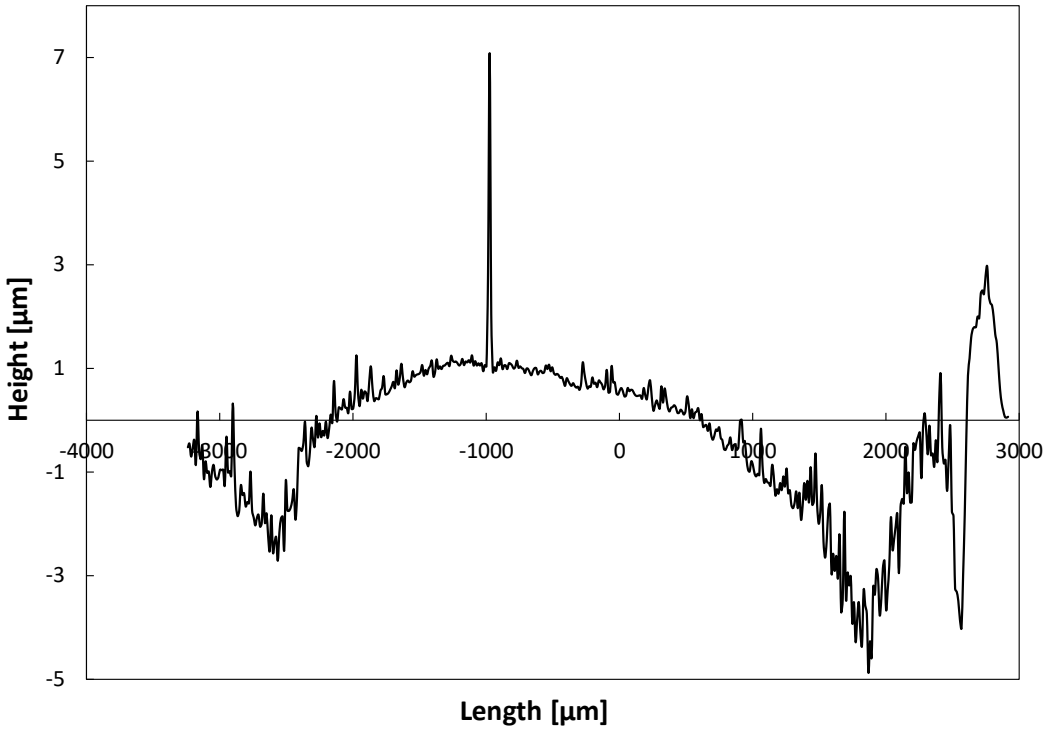

Figure 5.31: The GD-MS crater depth profile of Q.1300.3.1.

Table 5.7: The measured GD-MS sputtering rates [nm/s] for the silica crucible and quartz glass samples.

Material	Sputtering rate [nm/s]
Silica crucible	0.57
Quartz glass	0.30

5.3 Light microscopy

Figures 5.32, 5.33a and 5.33b show the light microscopy images of the surfaces of the quartz glass samples Q.1300.3.1 and Q.900.24.1, respectively. Figures 5.34a and 5.34b show the light microscopy images of the surfaces of the silica crucible sample C.1300.3.1. More cracks were observed in the surface of the quartz glass samples compared to the crucible samples. Contamination was visible on both materials. Small pores were also observed on the crucible surface. The cross-sections of the heat treated samples C.1200.7.1 and Q.1200.7.1 are shown in Figures 5.35a and 5.35b. The diffusion contact surface is shown at the top of the image.

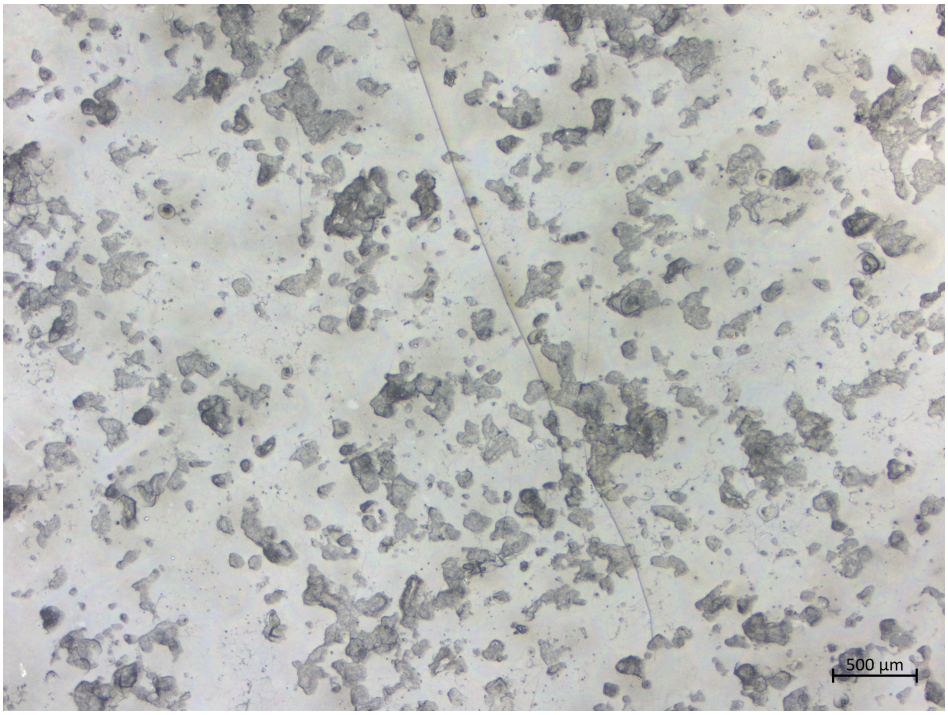

Figure 5.32: Light microscopy image of sample Q.1300.3.1 before polishing.

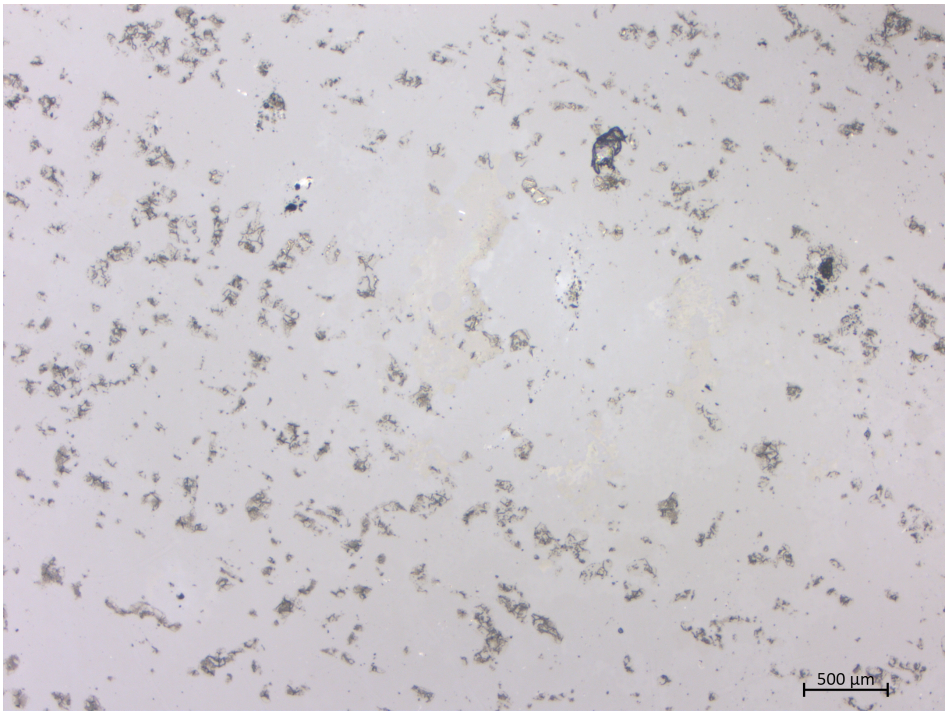

(a) Q.900.24.1 before polishing.

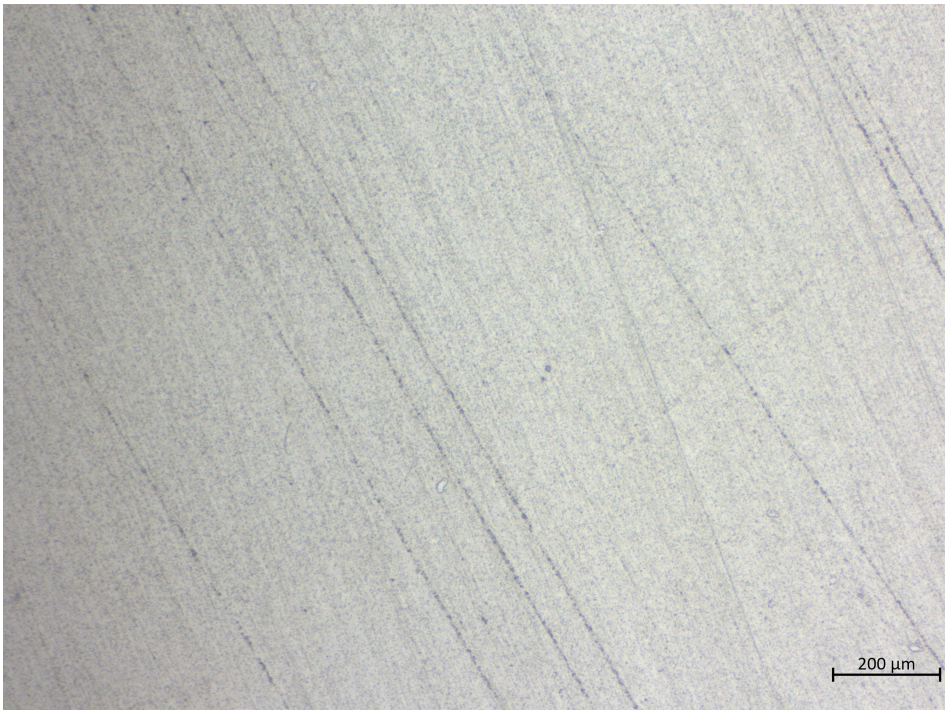

(b) Q.900.24.1 after polishing.

Figure 5.33: Light microscopy images of sample Q.900.24.1 before and after polishing.

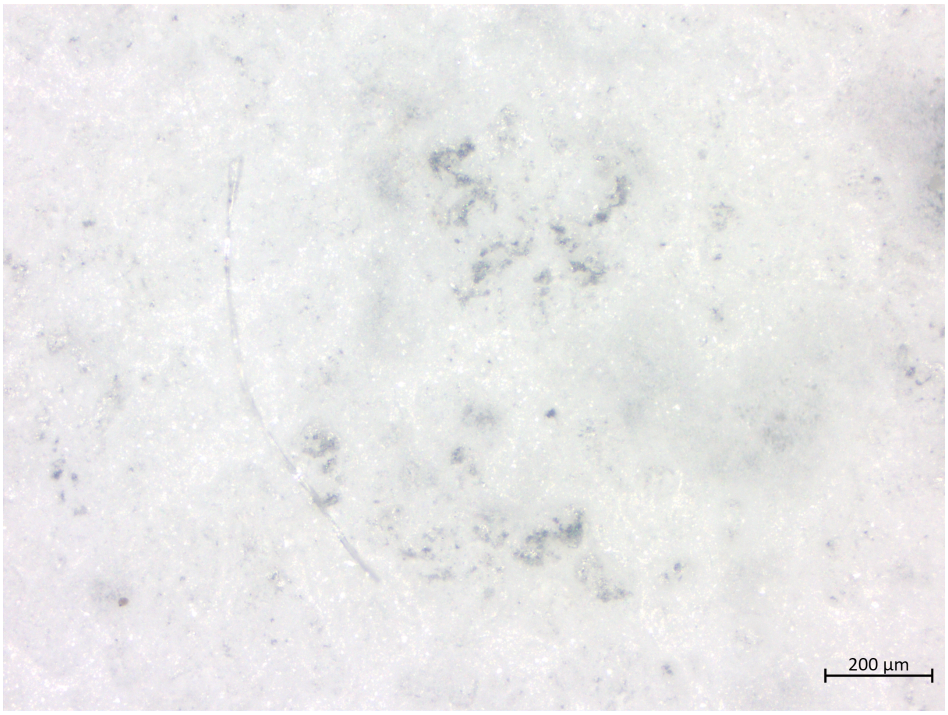

(a) C.1300.3.1 before polishing.

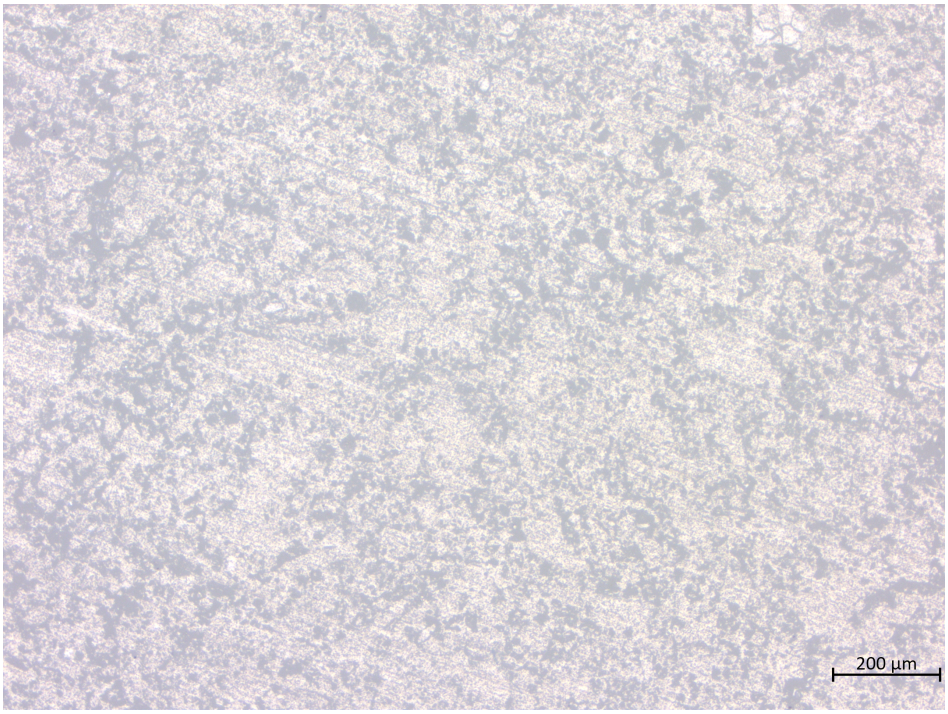

(b) C.1300.3.1 after polishing.

Figure 5.34: Light microscopy images of sample C.1300.3.1 before and after polishing.

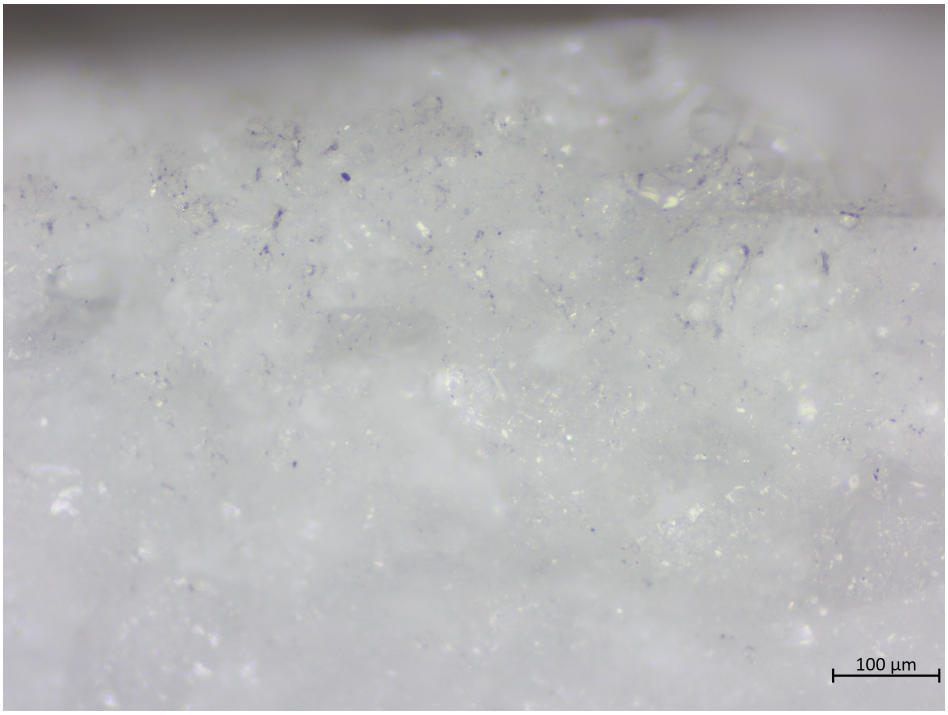

(a) The cross-section of C.1200.7.1.

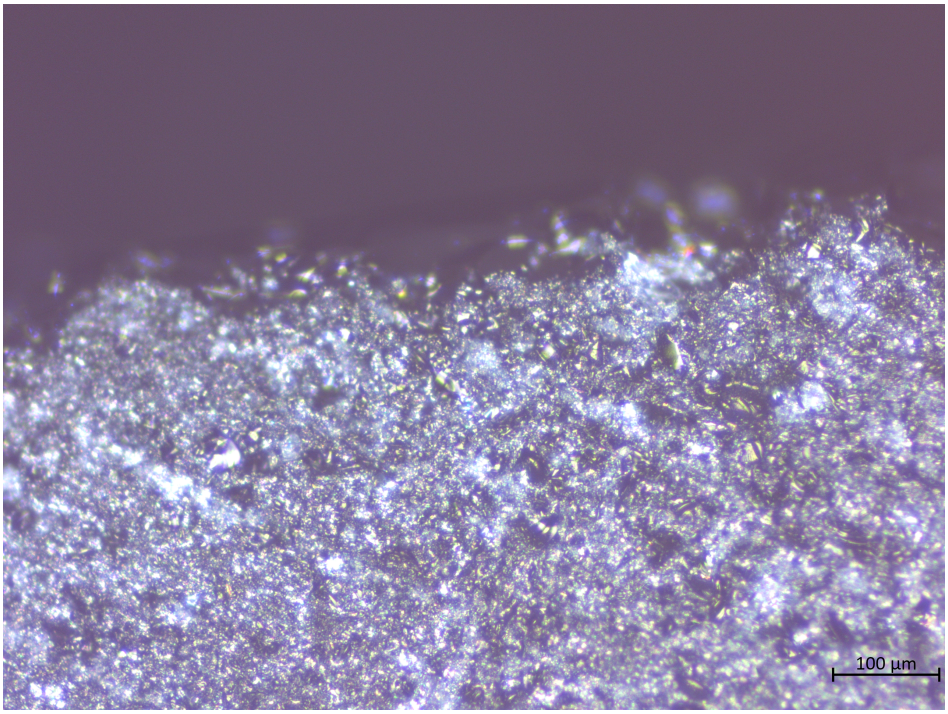

(b) The cross-section of Q.1200.7.1.

Figure 5.35: Light microscopy images of the cross-sections of C.1200.7.1 and Q.1200.7.1.

Chapter 6

Discussion

6.1 Diffusion experiments

To achieve solid-state diffusion through the diffusion couple technique, the contact between the two media has to be even throughout the entire surface area.[65] In this way, the concentration gradient will be equal on all points in the plane perpendicular to the flow direction. Ideally, the samples should have been polished to attain such even surface topographies. Specifically, the slip-cast silica crucible which was originally coated and had a more uneven surface. However, since polishing was avoided to prevent any iron contamination, it can be expected that the diffusion was not equal on all parts of the sample surface. Some areas may have had better contact than others, resulting in more diffusion of iron in certain areas of the sample. The cracks present in the quartz glass post heat treatment support this assumption. The quartz glass was only shattered on parts of the surface which could indicate that the pressure was not even on the entire surface plane and that these areas had more intimate contact. Therefore, the obtained results may not be representable for the entire sample since the GD-MS only analysed a small area of the sample surface. An interesting comparison would be to perform multiple GD-MS analyses on the same sample in different areas of the surface to examine if the iron diffusion is equal.

As mentioned, cracking in the quartz glass was observed after heat treatment. Quartz glass is a material with a very low thermal expansion coefficient. At 0-900 °C, the mean thermal expansion coefficient is only $4.8\text{x}10^{-7}$ K^{-1}.[66] This means that it can withstand rapid thermal changes. However, if a material with a different thermal expansion coefficient is attached to the quartz glass the two materials will expand and contract at different rates which can result in the glass cracking.[74] The steel plate, having a much higher thermal expansion coefficient ($12.5\text{x}10^{-6}$ K^{-1} at 20 °C [75]), was intimately placed together with the quartz glass for several hours during the diffusion experi-

ments. Since the quartz will expand and contract to a less extent compared to the steel it is likely to crack. Not to mention, the continuous maximum working temperature of the quartz glass is 1150 °C and heat treatments up to 1300 °C were performed.[66] If this affected the samples, it would be expected to see an increasing amount of cracking with increasing temperature. From visual observations, cracking was observed for all temperatures to an equal degree. However, from imaging with light microscopy a higher amount of microcracks was observed for the higher temperatures, see Figures 5.33a and 5.32.

6.2 GD-MS

The obtained concentration vs depth profiles correspond well with the expected profile from the literature given in Figure 2.10 in Chapter 2. The iron distributions measured in the slip-cast crucible shown in Figures 5.8, 5.10 and 5.12 were very even and had little scattering. However, for the samples C.900.24.2, Q.900.24.2, Q.1200.7.1 and Q.1300.3.1 some scattered areas were observed where a significant increase in the iron concentration occurred in the middle of the measurement. This inconsistency may be related to cracks present in the samples. A possibility is that iron accumulated in the cracks and as a result, the GD-MS measured higher iron levels in these areas. Reinforcing this argument is that the sudden increase of iron was observed more often in the quartz glass compared to in the silica crucible, and more cracks were observed in the quartz glass material. On the other hand, the inconsistency in the concentration profiles could also be due to instability in the plasma during the GD-MS analysis. Changes in the characteristics of the plasma, e.g the temperature or the electric field, will lead to instability in the plasma. Further, a high signal to noise ratio is prerequisite for detecting the iron concentrations.[67] The matrix element, Si, is used to quantify the concentrations of Fe and In through the ion beam ratio, shown in Equation (4.2) in Chapter 4. The GD-MS analyses the elements one at a time in consecutive order, starting with the lightest element (1.^{28}Si 2.^{56}Fe 3.^{115}In). Instability in the plasma for a longer time will reduce the ion beam signals measured of each element, but the ion beam ratio will not be affected. However, if the plasma is unstable for a short time, only during the analysis of the Si matrix element, the remaining measurements of Fe and In will be affected. This can be seen from Equation (4.2) where the iron concentration, K_{Fe}, increases when the matrix ion beam signal, I_M, is decreasing. This could explain the sudden increase observed in the concentration vs depth profiles.

6.2.1 Analysis of blank samples

The initial iron concentration in the standard grade slip-cast silica crucible was found to be 82.8 ppm. This is comparable to the reported values of 45.2-120 ppm measured in the same type of

crucible, shown in Table 2.2 in Chapter 2. Further, the initial iron level in the quartz glass was found to be 2.2 ppm which also corresponds to the typical iron level of 0.8 ppm reported by the producer, given in Table 4.1.[66] In this study, the difference in initial iron concentrations and the possible effect it has on the diffusion profiles have not been accounted for.

6.2.2 Slip-cast crucible

According to literature, the diffusion coefficient will increase with increasing temperature due to more atomic movement in the material, aiding the diffusive motion of atoms.[42] Contrary to expectations, the measured diffusion coefficients in Figure 5.14 for the silica crucible did not increase for all temperatures and showed a significant difference between 900-1100 °C and 1200-1300 °C. This inconsistency may be due to inadequate concentration profiles. Comparing the iron distributions in Figures 5.5, 5.8, 5.10 and 5.12, it seems like the samples heat treated at 1200-1300 °C were more polished before the GD-MS analysis, starting the measurements at lower iron levels than in the samples for 900-1100 °C. It would be expected to see higher iron levels in the higher temperature samples. Furthermore, it is clear from the correlation factors, R^2, in Figures 5.7, 5.9, 5.11 and 5.13 that the two concentration profiles measured at 900 °C and 1100 °C fit better to the diffusion equation than the ones measured at 1200 °C and 1300 °C. The R^2 values for 900 °C and 1100 °C were both above 0.8, while the R^2 values for 1200 °C and 1300 °C were 0.4 and 0.65, respectively. This can explain the large variation in the measured diffusion coefficients for the silica crucible. From this, it can be assumed that the measured diffusivities for 900 °C and 1100 °C are more accurate.

6.2.3 Quartz glass

In contrast to the crucible, the measured diffusion coefficients for the quartz glass increased with increasing temperature. The concentration profiles for all of the temperatures fit quite well to the diffusion equation with correlation factors, R^2, above 0.76. A surprising outcome was the measured diffusion profile for sample Q.900.24.1 in Figures 5.19 and 5.20. After the sample was analysed with GD-MS, the surface was re-polished to investigate the iron concentration further inside the sample. It would be expected to observe similar iron concentrations as the concentrations measured when the first GD-MS analysis ended. However, commencing the second analysis the detected iron concentrations were significantly increased. The sample was re-polished a second time but the iron concentrations were still very high. This finding was unexpected and suggests that either the polishing process, sample holder or the indium mask has contaminated the sample. If not, it is a contradicting diffusion behaviour that cannot be explained solely from this study.

Summarising the diffusivities in Figure 5.29 shows that for the temperature range 900-1300 °C the slip-cast silica crucible measured iron diffusivities one order of magnitude higher than in the quartz glass. The diffusion coefficients measured ranged from 10^{-13}-10^{-11} cm^2/s for the silica crucible and 10^{-14}-10^{-12} cm^2/s for the quartz glass, seen from Table 5.6. These results reflect those of Skarstad and Schubert et al. who also reported faster diffusion properties in the porous silica crucible.[30][10] Similar to this study, Skarstad measured a difference of one order of magnitude in the two quartz materials. The measured diffusivity in quartz glass also corresponds well with the literature values, especially the reported values by Ramappa et al., seen from Figure 5.29.[13] Previous studies by Skarstad and Schubert et al. argued that the porosity of the crucible could be related to the higher diffusion properties. This is a reasonable assumption since the porosity is one of the main dissimilarities between the two quartz materials. However, not enough literature on the effect of porosity on solid-state diffusion has been found to conclude this argument. In this study, a density of 1.95 g/cm^3 and 2.2 g/cm^3 was measured for the silica crucible and quartz glass, respectively. This corresponds well with the literature, see Figure 3.1 in Chapter 3. The potential link between the porous structure of the silica crucible and the higher diffusivity should be examined more closely with further studies. The silica crucibles are made from slip-casting of a silica slurry which results in the more porous structure.[18][19] The two quartz materials are essentially quite similar since the crucible consists of sintered quartz glass particles. This similarity could give rise to a hypothesis stating that the diffusion mechanisms of iron in the two materials should be similar. When comparing their diffusion in Figure 5.29, it can be seen that they follow the same trend, but at different orders of magnitudes. It should be noted that the reproducibility of the results from this study has not been tested. Concentration vs depth profiles were not obtained for all of the heat treated samples due to time limitations and the remaining heat treated samples should be analysed to validate the results.

6.2.4 Depth analysis

The calculated GD-MS sputtering rates were found to be 0.57 nm/s for the silica crucible and 0.30 nm/s for the quartz glass. These values can be related to the hardness of the materials. The quartz glass has documented hardness values of 5.5-6.5 on the Mohs scale.[66] Hardness values for the slip-cast crucible have not been found, but it can be assumed that it will have lower values due to the more porous and less dense structure. The depth profile of sample C.1200.7.1, in Figure 5.30, resembles the typical sputter crater from GD-MS given in Figure 4.15. The higher sidewalls is a result of the deposition of atoms from the sputtering process. The crater shape is, however, quite uneven. The crater in sample Q.1300.3.1, shown in Figure 5.31, is deeper at the sides compared to the centre and the crater walls are not vertical. The crater has a convex shape, compared to the more concave crater of sample C.1200.7.1, and is also quite uneven. The crater shapes can

be explained from the sputtering conditions in the GD-MS process. To achieve a decent depth resolution, the plasma conditions must be optimised to achieve homogeneous sputtering over the entire sample surface.[76] Inhomogeneous sputtering of the samples can, therefore, explain the uneven craters. The crater depths were also very small which makes it more challenging to provide good depth profiles. Due to time limitations and difficulties with the profilometer, only one depth profile from each material was obtained. The sputtering rates were used in the calculation of the diffusion coefficients. As a result, inaccurate depth profiles will give rise to uncertainty in the calculated diffusion profiles. A more optimal approach would be to measure several depth profiles of both materials and then measure the average depths and sputtering rates. Table A.1 in Appendix A presents the effect of varying the depth and diffusion time on the diffusion coefficient of sample C.1100.26.1. It was found that an increase in depth by 0.01 μm doubled the value of the diffusion coefficient. This means that uncertainty in the measured depths is likely to have a big effect on the results. In other words, the calculated values for iron diffusion in this study are probably not as precise and new depth profiles should be taken.

6.3 Light microscopy

The sample surfaces were highly contaminated after the diffusion experiments, seen from Figures 5.32, 5.33a and 5.34a. It seemed like more cracks were present in the surfaces of the quartz glass samples, compared to the silica crucible samples. The darker areas in the images are most likely cracks but are also likely to be iron contamination, in addition to other alloying elements in steel such as C, Cr and Cu. Since the sample surface has been in contact with the steel plate for a long time at higher temperatures it is expected that the surface will contain an extremely high amount of iron. This was also confirmed from the concentration profile of sample Q.1000.24.2 in Figure 5.21. The sample was not polished as much and the GD-MS measured iron levels of almost 4500 ppm. Furthermore, a visible difference in the sample surface was observed after polishing, see Figures 5.33a and 5.33b. The straight lines in the second image are grooves resulted from the polishing.

The diffusion of iron has been measured in the two quartz materials, but the diffusion mechanisms that occur have not been investigated. It is not possible to determine which iron phases are present in the sample from solely examining with light microscopy. According to literature, when the metal concentrations exceed its solubility limit, the iron will be present as precipitates forming other solid phases or compounds of different composition.[38] Knowing the chemical state of iron is an important part of understanding the diffusion mechanisms that occur in the material. An interesting examination would be to analyse the surface with secondary electron imaging (SEM) and x-ray diffraction (XRD) to identify the iron phases that are present in the sample after diffusion. This

would be an important finding to gain more knowledge on the iron behaviour in the silica crucible.

Both light microscopy images of the cross-sections of the crucible and quartz glass materials were quite blurry due to uneven topography. The cross-section of the quartz sample, in Figure 5.35b, revealed a very uneven surface with a lot of cracks. Further, the cross-section of the crucible sample, in Figure 5.35a, revealed darker spots in the area right below the surface and white spots deeper into the sample. This could be the pores present in the structure, where the darker spots contain accumulated iron. These findings could also be related to the sudden increase in iron concentration observed for some of the samples discussed earlier. If the iron accumulated in pores this would give a significant increase in the concentration profile. On the other hand, these darker areas could also be contamination from the cutting process. A conclusion based on only these images is not possible and more studies are necessary. Imaging the cross-section with SEM would have been better to observe the pores and cracks in the samples.

6.4 Technical challenges

During the second heat treatment at 900 °C the thermocouple oxidised and broke. Images are included in Appendix B, Figures B.6a and B.6b. The pressure increased from vacuum to 1.71 mbar and the top part of the processing quartz tube was black on the inside. The was most likely due to the production of SiO gas inside the processing tube. An additional closed-end alsint pipe (4 mm diameter) was added around the thermocouple for extra protection for the remaining experiments.

No sufficient results were retrieved from the second heat treatment at 1300 °C. The steel plate in between the quartz crucible and quartz glass seemed to have melted and was stuck onto both sample surfaces, see Figure 5.3. Carbon steel usually melts at higher temperatures, ranging from 1425-1540 °C, depending on the composition.[77] Typically, the melting point decreases with increasing carbon content.[78] The lowered melting point indicates that a reaction occurred in the processing tube during the diffusion experiment.[77] The mullite tube cracked after commencing the heat treatment, the pressure increased and air leaked into the tube. A leakage in the system will contaminate the atmosphere and may explain why the steel melted below its melting point. Since the leakage also was the only difference from the first experiment that was performed successfully, it is reasonable to assume that the results are related to this. At higher heating temperatures and in oxidising atmospheres, oxygen can penetrate deep into the steel and oxidise the grains resulting in a weakening of the bonds.[78] Oxidising gases can diffuse into the steel even before reaching the melting point. Especially when the metal is held at a high temperature over time, overheating is more likely to happen.[78] From Figure 5.3 it can be seen that it is mostly the excess steel around

the contact surfaces of the crucible and quartz glass that melted. This supports the assumption of oxygen penetration since this area was most exposed to the furnace atmosphere.

According to the furnace specifications, the maximum working temperature of the mullite tube under vacuum conditions is 1300 °C. The mullite tube cracked most likely due to the rapid thermal change from room temperature to 1300 °C. In a vacuum atmosphere, the heating rate can be much higher and the mullite probably could not withstand the abrupt change in temperature. Even though the tube was placed in the furnace opening to gradually heat up, the thermal change was still too rapid. A better approach could be to preheat the mullite tube to a lower temperature, e.g. 200 °C, before slowly heating it to 1300 °C. However, this would involve diffusion to occur before reaching 1300 °C giving a more inaccurate measurement which is a disadvantage. Another solution could be to use an argon atmosphere instead of vacuum which would increase the maximum working temperature of the mullite tube to 1500 °C.

Chapter 7

Conclusion

This study aimed to measure the diffusion coefficient of iron in amorphous quartz (SiO_2) crucibles by conducting heat treatments of diffusion couples consisting of standard grade silica crucible and steel, with quartz glass as a reference. As a conclusion, over the temperature range 900-1300 °C, the following Arrhenius relations were obtained for the diffusion of iron in a silica crucible and synthetic quartz glass, respectively,

$$D = 6.53 \cdot 10^{-8} exp\left(\frac{-1.154 \text{ eV}}{kT}\right) \text{ cm}^2\text{/s}$$
$$D = 1.05 \cdot 10^{-9} exp\left(\frac{-0.937 \text{ eV}}{kT}\right) \text{ cm}^2\text{/s}$$

The two quartz materials showed a similar trend in diffusivity, but different orders of magnitude. The diffusion of iron in the slip-cast silica crucible was measured to be one order of magnitude higher than in the synthetic quartz glass, with calculated diffusion coefficients in the range of 10^{-13}-10^{-11} cm^2/s compared to 10^{-14}-10^{-12} cm^2/s for the quartz glass. This means that iron diffuses much faster in the quartz crucible material, which in turn means a higher contamination potential of the silicon melt. The results from this study can be further used to model the iron distribution in the mc-Si ingot to gain more knowledge on the iron in-diffusion and contamination of mc-Si ingots for solar cells.

A method for conducting heat treatment of diffusion pairs, using a GSL-1500X-50RTP tube furnace, and obtaining concentration vs depth profiles from GD-MS has been developed. Adequate diffusion profiles were obtained using GD-MS with little scattering in the measurements. The sputtering rates of the silica crucible and quartz glass were found to be 0.57 nm/s and 0.30 nm/s, respectively. However, depth profiles of multiple samples should be measured to establish a greater degree of accuracy on this matter which would further give more precise diffusion coefficients.

Chapter 8

Further work

Based on the results presented in this thesis, further studies should validate the measured diffusion coefficients of iron in the silica crucible and quartz glass. A natural progression of this work would be to analyse the remaining heat treated samples to investigate the reproducibility of the experiments. Two GD-MS measurements for each temperature should be performed for all of the temperatures (900-1300 °C). This will improve the statistics of this study and also give better diffusion profiles. The study should be repeated using a different iron source material with a lower thermal expansion coefficient than steel. This is to prevent the cracking observed in the quartz glass samples. Less cracking could give a more precise GD-MS analysis and correspondingly concentration vs depth profile. Also, more accurate depth profiles should be done to improve the calculated sputtering rates, as it was seen that the depth had a big impact on the calculated diffusion coefficients.

Moreover, further investigation of the material structures in the two quartz materials is strongly recommended. XRD should be used to identify the iron phases present in the sample. Knowledge on the chemical state of iron in amorphous quartz is important to understand the diffusion mechanisms of iron in the silica crucible. Imaging the surface and cross-section with SEM would also be suggested to investigate the pores and cracks in the two materials. The potential link between the porous structure of the silica crucible and the higher diffusivity should be examined more closely to establish a greater degree of comprehension on this matter.

Bibliography

[1] N. Taylor and A. Jäger-Waldau. Low carbon energy observatory photovoltaics technology development report 2018 – public version. *European Commission, Luxemburg*, EUR 29916 EN, 2019.

[2] T. Markvart. *Solar Electricity*. John Wiley and Sons, LTD, 2000.

[3] ISE Fraunhofer Institute for Solar Energy Systems. Photovoltaics report. Freiburg, Germany, 14 November 2019.

[4] F. Schindler, B. Michl, J. Schon, W. Kwapil, W. Warta, and M. C. Schubert. Solar cell efficiency losses due to impurities from the crucible in multicrystalline silicon. *IEEE Journal of Photovoltaics*, 4(1):122–129, 2014.

[5] Y. M. Yang, A. Yu, B. Hsu, W. C. Hsu, A. Yang, and C. W. Lan. Development of high-performance multicrystalline silicon for photovoltaic industry. *Progress in photovoltaics: research and applications*, 23:340–351, 2015.

[6] R. Kvande, L. Arnberg, C. Martin, G. Rancoule, L. Dupuy, and A. Holt. Influence of crucible and coating quality on the properties of multicrystalline silicon for solar cells. *Journal of Crystal Growth*, 311(3):765–768, 2009.

[7] M. P. Bellmann, E. A. Meese, M. Syvertsen, A. Solheim, H. Sørheim, and L. Arnberg. Silica versus silicon nitride crucible: Influence of thermophysical properties on the solidification of multi-crystalline silicon by bridgman technique. *Journal of Crystal Growth*, 318:265–268, 2011.

[8] A. A Istratov, H. Hieslmair, and E. R. Weber. Iron and its complexes in silicon. *Applied Physics A*, 69:13–44, 1999.

[9] R. Kvande, L. Geerligs, G. Coletti, Lars A., M. Di Sabatino, E. Øvrelid, and C. Swanson. Distribution of iron in multicrystalline silicon ingots. *Journal of Applied Physics*, 104(6): 064905 – 064905, 2008.

[10] M. C. Schubert, J. Schon, F. Schindler, W. Kwapil, A. Abdollahinia, B. Michl, S. Riepe, C. Schmid, M. Schumann, S. Meyer, and W. Warta. Impact of impurities from crucible and coating on mc-silicon quality - the example of iron and cobolt. *IEEE Journal of Photovoltaics*, 3(4):1250–1258, 2013.

[11] M. D. Abbott, D. Poplavskyy, G. Scardera, D. Inns, F. Lemmi, K. R. McIntosh, and S. C. Baker-Finch. Iron contamination in silicon solar cell production environments. In *IEEE 40th Photovoltaic Specialists Conference (PVSC)*, Denver, Colorado, USA, June 2014.

[12] J. Schön, H. Habenicht, M. C. Schubert, and W. Warta. Understanding the distribution of iron in multicrystalline silicon after emitter formation: Theoretical model and experiments. *Journal of Applied Physics*, 109:063717, 2011.

[13] D. A. Ramappa and W. B. Henley. Diffusion of iron in silicon dioxide. *Journal of The Electrochemical Society*, 146(10):3773–3777, 1999.

[14] A. A. Istratov, W. Huber, and E. R. Weber. Gettering strategies in soi wafers. *Solid State Phenomena*, 95-96:547–552, 2004.

[15] A. McEvoy, L. Castañer, and T. Markvart. *Solar Cells: Materials, Manufacture and Operation*. Academic Press, 2013.

[16] G. Müller and P. Rudolph. Crystal growth from the melt. *Encyclopedia of Materials: Science and Technology (Second Edition)*, pages 1866–1872, 2001.

[17] V. Pupazan, R. Negrila, O. Bunoiu, I. Nicoara, and D. Vizman. Effects of crucible coating on the quality of multicrystalline silicon grown by a bridgman technique. *Journal of Crystal Growth*, 401:720–726, 2014.

[18] T. Markvart and L. Castaner. *Practical Handbook of Photovoltaics: Fundamentals and Applications*. Elsevier Ltd., 2003.

[19] N. P Bansal and J. P. Singh. *Innovative Processing and Synthesis of Ceramics, Glasses, and Composites VI*. The American Ceramic Society, 2002.

[20] R. Roligheten, G. Rian, and S. Julsrud. Reusable crucibles and method of manufacturing them. *International Patent WO 2007/148986 A1*, 2007.

[21] D. Camel, B. Drevet, V. Brizé, F. Disdier, E. Cierniak, and N. Eustathopoulos. The crucible/silicon interface in directional solidification of photovoltaic silicon. *Acta Materialia*, 129:415–427, 2017.

[22] B. Drevet, O. Pajani, and N. Eustathopoulos. Wetting, infiltration and sticking phenomena in si3n4 releasing coatings in the growth of photovoltaic silicon. *Solar Energy Materials and Solar Cells*, 94:425–431, 2010.

[23] D. W. Richerson and W. E. Lee. *Modern Ceramic Engineering: Properties, Processing, and Use in Design 4th Edition*. CRC Press, 2018.

[24] A. Atkinson and J. W. Gardner. The diffusivity of fe^{3+} in amorphous sio_2 and the protective properties of sio2 layers. *Corrosion Science*, 21:49–58, 1981.

[25] A. R. West. *Solid State Chemistry and its Applications*. John Wiley and Sons, 2014.

[26] V. Presser and K. G. Nickel. Silica on silicon carbide. *Critical Reviews in Solid State and Materials Sciences*, 33(1):1–99, 2008.

[27] J. F. Shackelford and R. H. Doremus. *Ceramic and glass materials: Structure, properties and processing*. Springer Science and Business Media, 2008.

[28] J. Nelson. *The Physics of Solar Cells*. Imperial College Press, 2003.

[29] R. Kvande, L. Arnberg, and C. Martin. Influence of crucible and coating quality on the properties of multicrystalline silicon for solar cells. *Journal of Crystal Growth*, 311:765–768, 2009.

[30] H. V. Skarstad. Behaviour of the slip-cast crucible as a contamination source during silicon directional solidification. *Master Thesis NTNU*, 2016.

[31] G. Stokkan, M. Di Sabatino, R. Søndenå, M. Juel, A. Autruffe, K. Adamczyk, H. V. Skarstad, K. E. Ekstrøm, M. S. Wiig, C. Chuan You, H. Haug, and M. M'Hamdi. Impurity control in high performance multicrystalline silicon. *Phys. Status Solidi*, 214(7):1700319, 2017.

[32] Dr. B. Geyer, G. Schwichtenberg, and Dr. A. Miiller. Increased wafer yield in silicon ingots by the application of high purity silicon nitride-coating and high purity crucibles. In *Proc. IEEE 31st Photovolt. Spec. Conf.*, page 1059–1061, Orlando, FL, USA, 2005.

[33] G. P. Willeke and E. R. Weber. *Advances in Photovoltaics: Volume 1*. Academic Press, 2012.

[34] G. Coletti, P. C. P. Bronsveld, G. Hahn, W. Warta, D. Macdonald, B. Ceccaroli, K. Wambach, N. Le Quang, and J. M. Fernandez. Impact of metal contamination in silicon solar cells. *Advanced Functional Materials*, 21:879–890, 2011.

[35] D. Macdonald, A. Cuevas, A. Kinomura, Y. Nakano, , and L. J. Geerligs. Transition-metal profiles in a multicrystalline silicon ingot. *Journal of Applied Physics*, 97:033523, 2005.

[36] D. M. Othman Abdel Barey. Concentrations and reactions of iron in crystalline silicon after aluminum gettering. *PhD Thesis Georg-August-Universität Göttingen*, 2011.

[37] S. Beringov, T. Vlasenko, S. Yatsuk, O. Liaskovskiy, and I. Buchovska. Mono-like ingot/wafers made of solar-grade silicon for solar cells application. pages 507–511, 06 2012. ISBN 9781118291405. doi: 10.1002/9781118359341.ch60.

[38] G. Coletti. Impurities in silicon and their impact on solar cell performance. *PhD Thesis*, 2011 ISBN: 978 9086 720 514.

[39] T. U. Nærland, L. Arnberg, and A. Holt. Origin of the low carrier lifetime edge zone in multicrystalline pv silicon. *Progress in Photovoltaics: Research and Applications*, 17:289–296, 2009.

[40] T. Buonassisi, A. A. Istratov, M. D. Pickett, M. Heuer, J. P. Kalejs, G. Hahn, M. A. Marcus, B. Lai, Z. Cai, S. M. Heald, T. F. Ciszek, R. F. Clark, D. W. Cunningham, A. M. Gabor, R. Jonczyk, S. Narayanan, E. Sauar, and E. R. Weber. Chemical natures and distributions of metal impurities in multicrystalline silicon materials. *Prog. Photovolt: Res. Appl.*, 14: 513–531, 2006.

[41] A. Autruffe, M. M'hamdi, F. Schindler, F. D. Heinz, K. E. Ekstrøm, M. C. Schubert, M. Di Sabatino, and G. Stokkan. High performance multicrystalline silicon: Grain structure and iron precipitation. *Journal of Applied Physics*, 122:135103, 2017.

[42] W. D Callister and D. G. Rethwisch. *Materials Science and Engineering*. John Wiley and Sons, 2015.

[43] T. M. Harrison and P. K. Zeitler. Fundamentals of noble gas thermochronometry. *Reviews in Mineralogy and Geochemistry*, 58:123–149, 2005.

[44] J. Crank. *The Mathematics of Diffusion*. Oxford University Press, 1975.

[45] G. Coletti. Sensitivity of state-of-the-art and high efficiency crystalline silicon solar cells to metal impurities. *Progress in Photovoltaics: Research and Applications*, 21:1163–1170, 2013.

[46] D. J. Cherniak, E. B. Watson, and D. A. Wark. Ti diffusion in quartz. *Chemical Geology*, 236:65–74, 2007.

[47] D. J. Cherniak. Diffusion in quartz, melilite, silicate perovskite, and mullite. *Reviews in Mineralogy and Geochemistry*, 72:735–756, 2010.

[48] R. N. Ghoshtagore. Diffusion of nickel in amorphous silicon dioxide and silicon nitride films. *Journal of Applied Physics*, 40(11):4374–4376, 1969.

[49] E. D. Martello. Impurity distribution and reduction behaviour of quartz in the production of high purity silicon. *Thesis for the degree of Philosophiae Doctor NTNU*, Trondheim, September 2012.

[50] L. Nuccio. Diffusion of small molecules in amorphous sio_2: effects on the properties of the material and on its point defects. *PhD Thesis University of Palermo*, Palermo, February 2009.

[51] B. Rottier, H. Rezeau, V. Casanova, K. Kouzmanov, R. Moritz, K. Schlöglova, M. Wälle, and L. Fontboté. Trace element diffusion and incorporation in quartz during heating experiments. *Contrib Mineral Petrol*, 172:23, 2017.

[52] F. Jacamon and R. B. Larsen. Trace element evolution of quartz in the charnockitic kleivan granite, sw-norway: The ge/ti ratio of quartz as an index of igneous differentiation. *Lithos*, 107:281–291, 2009.

[53] I. G. Polyakova. Chapter 4: The main silica phases and some of their properties. *Glass: Selected Properties and Crystallization*, pages 197–267, 2014.

[54] Hudson Institute of Mineralogy. Mindat. URL `http://www.mindat.org`. Last visited 17.04.2020.

[55] D. J. Cherniak. Diffusion in quartz, melilite, silicate perovskite, and mullite. *Reviews in Mineralogy and Geochemistry*, 72:735–756, 2010.

[56] D. J. Cherniak, N. D. Tailby, and E. B. Watson. Al diffusion in quartz. *American Mineralogist*, 103:839–847, 2018.

[57] O. Kononchuk, K. G. Korablev, N. Yarykin, and G. A. Rozgonyi. Diffusion of iron in the silicon dioxide layer of silicon-on-insulator structures. *Applied Physics Letters*, 73(9):1206–1208, 1998.

[58] R. W. Lee, R. C. Frank, and D. E. Swets. Diffusion of hydrogen and deuterium in fused quartz. *J. Chem. Phys.*, 36(4):1062, 1962.

[59] J. Verhoogen. Ionic diffusion and electrical conductivity in quartz. *Am. Mineral.*, 37:637–655, 1952.

[60] D. J. Cherniak, J. B. Thomas, and E. B. Watson. Neon diffusion in olivine and quartz. *Chemical Geology*, 371:68–82, 2014.

[61] W. G. Perkins and D. R. Begeal. Diffusion and permeation of he, ne, ar, kr, and d_2 through silicon oxide thin films. *J. Chem. Phys.*, 54(4):1683, 1971.

[62] F. J. Norton. Permeation of gaseous oxygen through vitreous silica. *Nature*, 191(4789):701, 1961.

[63] J. B. Brady and D. J. Cherniak. Diffusion in minerals: An overview of published experimental diffusion data. *Reviews in Mineralogy and Geochemistry*, 72, 2010.

[64] G. D. Bromiley and M. Hiscock. Grain boundary diffusion of titanium in polycrystalline quartz and its implications for titanium in quartz (titaniq) geothermobarometry. *Geochimica et Cosmochimica Acta*, 178:281–290, 2016.

[65] A. A. Kodentsov, G. F. Bastin, and F. J. J. van Loo. The diffusion couple technique in phase diagram determination. *Journal of Alloys and Compounds*, 320(2):207–217, 2001.

[66] Heraeus Quarzglas GmbH and Co KG. Quartz Glass for Optics Data and Properties. URL `https://www.heraeus.com/media/media/hca/doc_hca/products_and_solutions_8/optics/Data_and_Properties_Optics_fused_silica_EN.pdf`. Last visited 27.05.2020.

[67] M. Di Sabatino. Detection limits for glow discharge mass spectrometry (gdms) analyses of impurities in solar cell silicon. *Measurement*, 50:135–140, 2014.

[68] G. Huber, G. Passler, K. Wendt, J. V. Kratzand, and N. Tratumann. *Handbook of Radioactivity Analysis (2nd Edition), Chapter 10*. Academic Press, 2003.

[69] A. A. Ganeev, A. R. Gubal, K. N. Uskov, and S. V. Potapov. Analytical glow discharge mass spectrometry. *752 Russian Chemical Bulletin, International Edition*, 61(4):752–767, 2012.

[70] Thermo Fisher Scientific. Element GD Plus Glow Discharge Mass Spectrometer. URL `https://assets.thermofisher.com/TFS-Assets/CMD/brochures/BR-30066-GD-MS-ELEMENT-GD-PLUS-BR30066-EN.pdf`. Last visited 01.04.2020.

[71] F. L. King, Teng. J., and R. E. Steiner. Glow discharge mass spectrometry: Trace element determinations in solid samples. *Journal of Mass Spectrometry*, 30:1061–1075, 1995.

[72] V. Hoffmann, M. Kasik, P. K. Robinson, and C. Venzago. Glow discharge mass spectrometry. *Analytical and Bioanalytical Chemistry*, 381:173–188, 2005.

[73] R. Williams. *Surface Modification of Biomaterials: Methods Analysis and Applications*. Woodhead Publishing, 2011.

[74] Q. A. Acton. *Advances in Silicon Dioxide Research and Application*. ScholarlyEditions, 2003.

[75] R. N. Gunn. *Duplex Stainless Steels: Microstructure, Properties and Applications*. Woodhead Publishing, 1997.

[76] T. Prohaska, J. Irrgeher, A. Zitek, and N. Jakubowski. *Sector Field Mass Spectrometry for Elemental and Isotopic Analysis*. Royal Society of Chemistry, 2014.

[77] Engineering ToolBox. Metals and Alloys - Melting Temperatures, 2005. URL `https://www.engineeringtoolbox.com/melting-temperature-metals-d_860.html`. Last visited 18.05.2020.

[78] NPCS Board of Consultants and Engineers. *The Complete Techonology Book on Steel and Steel Products*. Asia Pacific Business Press Inc., 2008.

Appendices

A Calculations

A.1 Density

The density, ρ [g/cm^3], of the quartz glass and crucible samples were calculated from the equation,

$$\rho = \frac{m}{V} \tag{A.1}$$

where m [g] and V [cm^3] is the mass and volume of the sample, respectively.

A.2 Iron diffusion profiles

The steel surface was considered to be an infinite source of iron so a one-dimensional solution to Fick's law of diffusion could be applied. The surface concentration of iron was assumed to remain constant for the whole duration of diffusion.[13] The concentration profile was then assumed to follow the solution,

$$C = C_0(1 - erf\left(\frac{x}{2\sqrt{Dt}}\right)) \tag{A.2}$$

where C [mol/m^3] is the iron concentration at distance x [m] and time t [s]. C_0 [mol/m^3] is the boundary concentration of iron and D [m^2/s] is the diffusion coefficient.[44] Equation (A.2) can be rewritten as,

$$erf^{-1}\left(1 - \frac{C}{C_0}\right) = \frac{x}{\sqrt{4Dt}} \tag{A.3}$$

From this, the diffusion profile can be calculated by plotting the inverse of the error function, erf^{-1}(1-$\frac{C}{C_0}$), against the depth, x. This plot should yield a straight line with a slope corresponding

to $\frac{x}{\sqrt{4Dt}}$ and a zero intercept if the diffusion profile conforms to the assumed model. Linear regression is used to obtain the slope and the diffusion coefficient, D, is calculated.

C_0 is not known with certainty in this approach, however a good guess of C_0 can be made from inspecting the diffusion profile. If the intercept of the regression deviated significantly from zero, C_0 was adjusted until a zero intercept was obtained. The diffusion coefficient, D, could then be calculated from the slope.

$$ln(D) = ln(D_0) - \frac{E_a}{kT} \tag{A.4}$$

Furthermore, using the calculated D at each temperature, ln(D) was plotted against the inverse of temperature, 1/T, to calculate the temperature-dependent preexponential, D_0, from the intercept value $ln(D_0)$. The activation energy, E_a, was calculated from the slope -$\frac{E_a}{kT}$. As a result, the Arrhenius relation according to Equation (2.10) from Chapter 2 was obtained.

A.3 Sputtering rates

The average crater depths were measured to be 5.45 µm for C.1200.7.1 and 2.91 µm for Q.1300.3.1. The number of GD-MS measurements per sample were 241 and 244 for C.1200.7.1 and Q.1300.3.1, respectively, and the analysis time for each measurement was 40 seconds. This gives sputtering rates equal to,

$$\text{Sputtering rate (quartz glass)} = \frac{2.91\ \mu\text{m}}{244}\frac{1}{40\ \text{s}} = 0.30\ \text{nm/s} \tag{A.5}$$

$$\text{Sputtering rate (crucible)} = \frac{5.45\ \mu\text{m}}{241}\frac{1}{40\ \text{s}} = 0.57\ \text{nm/s} \tag{A.6}$$

A.4 Uncertainty in D

There is uncertainty in both the diffusion time, t, and the measured depths, x. Both variables are included in the equation for calculating the diffusion coefficient. To see how a certain change in these variables affect the diffusion coefficient, D, the two variables were changed and new values for D were calculated. This was done using the values calculated for sample C.1100.26.1 and the results are given in Table A.1. It was found that the depth had the biggest effect on the diffusion coefficient. An increase in the depth by 0.01 µm doubled the value of the diffusion coefficient.

Table A.1: The effect of varying the depth, x, and diffusion time, t, on the diffusion coefficient, D, for sample C.1100.26.1. The diffusion coefficient for C.1100.26.1 was measured to be 4.01x10^{-17} m^2/s, t was 26 hours and x was 0.0226 μm.

Variable		ΔD **[m^2/s]**
$\Delta\, x$	+0.01 μm	+4.33x10^{-17}
	-0.01 μm	-2.76x10^{-17}
$\Delta\, t$	+5 min	-1.28x10^{-17}
	-5 min	+1.29x10^{-17}

B Diffusion experiments

Images of the slip-cast crucible, steel and quartz glass samples after heat treatment are given in Figures B.1-B.4. Images of the cracked mullite tubes after attempting heat treatment at 1300 °C are included in Figure B.5.

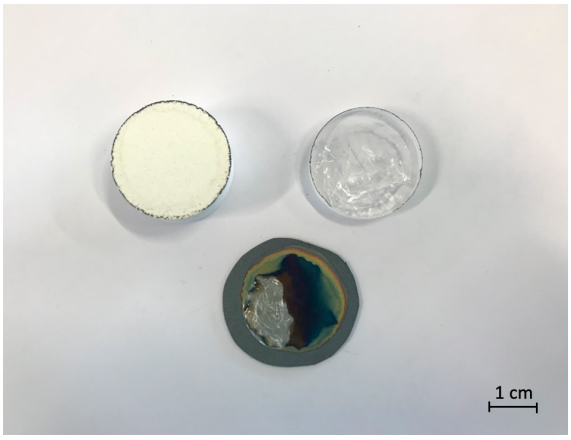

(a) Samples C.900.24.2 and Q.900.24.2.

(b) Samples C.1300.24.1 and Q.1300.24.1.

Figure B.1: Quartz glass, crucible and steel samples post heat treatment at 900 °C and 1300 °C.

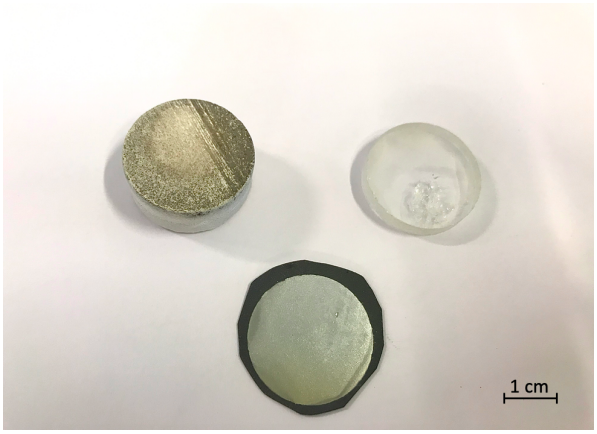

(a) Samples C.1000.24.1 and Q.1000.24.1.

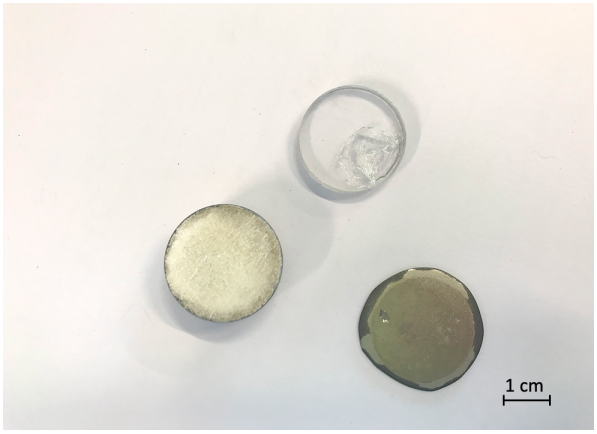

(b) Samples C.1000.24.2 and Q.1000.24.2.

Figure B.2: Quartz glass, crucible and steel samples post heat treatment at 1000 °C.

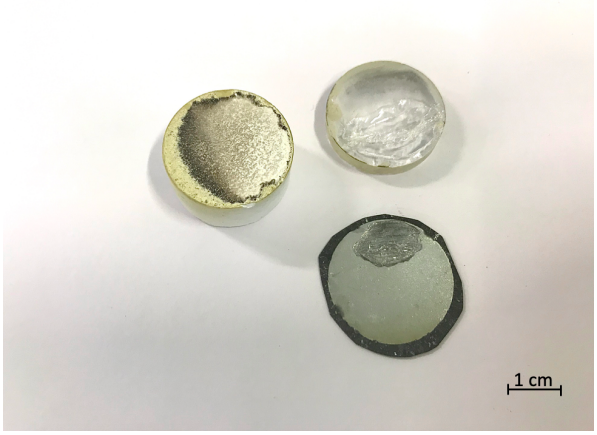

(a) Samples C.1100.26.1 and Q.1100.26.1.

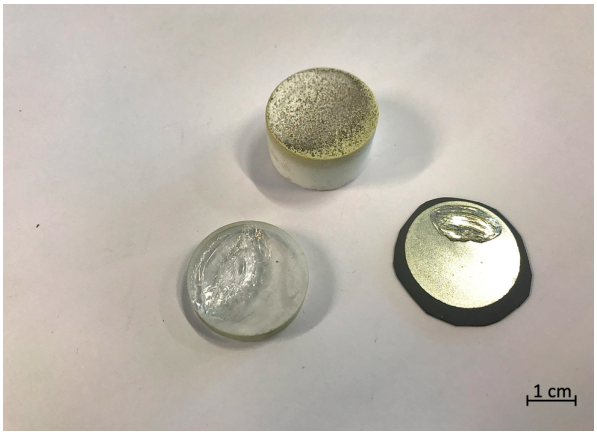

(b) Samples C.1100.24.2 and Q.1100.24.2.

Figure B.3: Quartz glass, crucible and steel samples post heat treatment at 1100 °C.

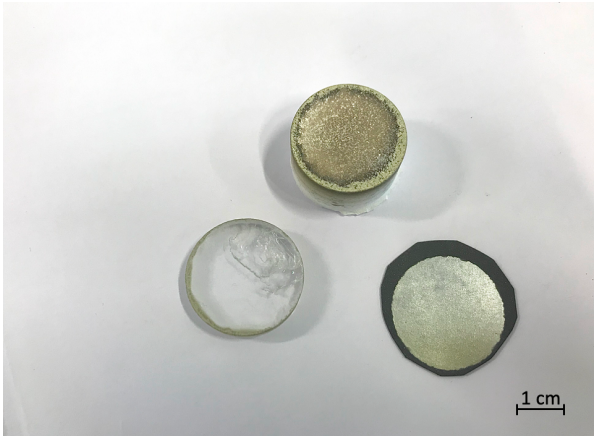

(a) Samples C.1200.24.1 and Q.1200.24.1.

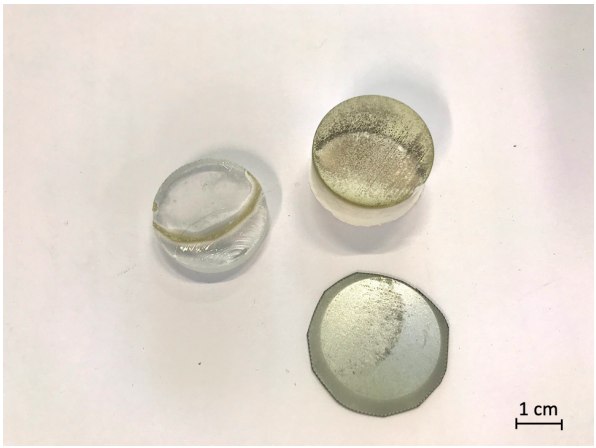

(b) Samples C.1200.24.2 and Q.1200.24.2.

Figure B.4: Quartz glass, crucible and steel samples post heat treatment at 1200 °C.

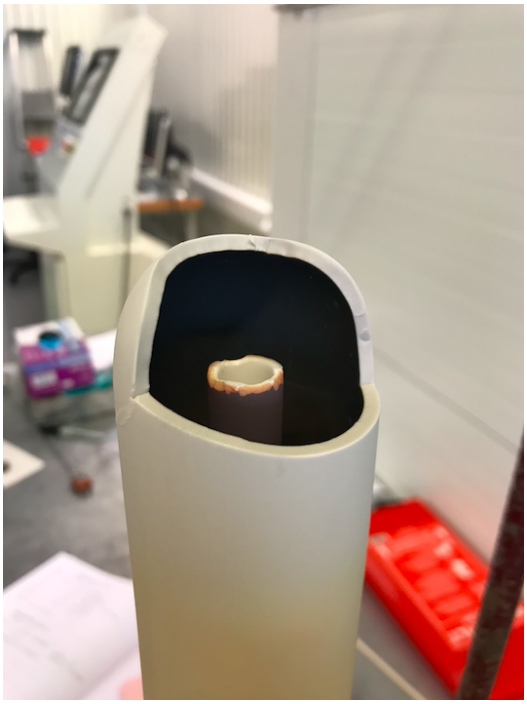

(a) Second attempt of heat treating at 1300 °C.

(b) Third attempt of heat treating at 1300 °C.

Figure B.5: The cracked mullite tubes after heat treatment at 1300 °C.

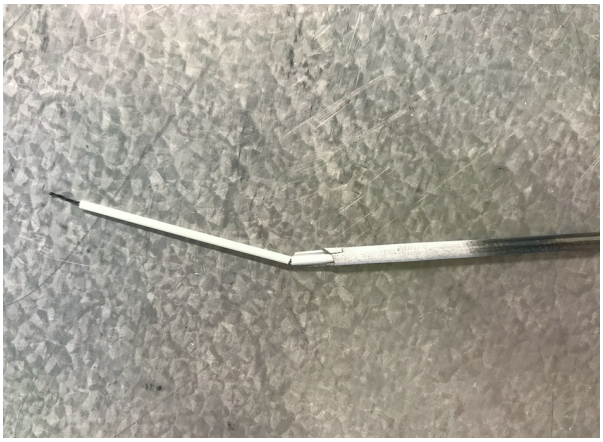

(a) The oxidised thermocouple.

(b) An additional closed-end alsint pipe was added inside the original alsint pipe to protect the thermocouple from oxidising.

Figure B.6: Adjustments made to the experimental setup after the thermocouple oxidised.

C Instrumental

Table C.1: Tube furnace specifications for GSL-1500X-50RTP.

Temp. accuracy [°C]	Max temp. [°C]	Continuous temp. [°C]
± 1	1500	1400

Table C.2: The heating speed [°C/s] given for the mullite and quartz processing tubes at different temperatures.

Temperature [°C]	Heating speed [°C/s]
For mullite tube:	
RT-800	7
800-1000	7
1000-1100	4
1100-1200	3
1200-1300	1.5
1300-1350	0.7
For quartz tube:	
RT-500	30
500-800	12
800-900	5
900-1000	3.6
1000-1100	1

Ragnhild Austreid

Diffusion studies of Fe in amorphous quartz for the PV industry

NTNU
Norwegian University of
Science and Technology